Adapted inversion strategies for electrical resistivity data to explore layered near-surface environments

Kumulative Dissertation
zur Erlangung des akademischen Grades
"doctor rerum naturalium"
(Dr. rer. nat.)
in der Wissenschaftsdisziplin "Angewandte Geophysik"

eingereicht an der
Mathematisch-Naturwissenschaftlichen Fakultät
Institut für Geowissenschaften
der Universität Potsdam

von
M.Sc. Mauricio Arboleda-Zapata
Potsdam, den 20.01.2023

Supervisors and reviewers: Prof. Dr. Jens Tronicke and Prof. Dr. Oliver Korup
Externas reviewer: Dr. Florian Wagner

Published online on the
Publication Server of the University of Potsdam:
https://doi.org/10.25932/publishup-58135
https://nbn-resolving.org/urn:nbn:de:kobv:517-opus4-581357

Summary

The electrical resistivity tomography (ERT) method is widely used to investigate geological, geotechnical, and hydrogeological problems in inland and aquatic environments (i.e., lakes, rivers, and seas). The objective of the ERT method is to obtain reliable resistivity models of the subsurface that can be interpreted in terms of the subsurface structure and petrophysical properties. The reliability of the resulting resistivity models depends not only on the quality of the acquired data, but also on the employed inversion strategy. Inversion of ERT data results in multiple solutions that explain the measured data equally well. Typical inversion approaches rely on different deterministic (local) strategies that consider different smoothing and damping strategies to stabilize the inversion. However, such strategies suffer from the trade-off of smearing possible sharp subsurface interfaces separating layers with resistivity contrasts of up to several orders of magnitude. When prior information (e.g., from outcrops, boreholes, or other geophysical surveys) suggests sharp resistivity variations, it might be advantageous to adapt the parameterization and inversion strategies to obtain more stable and geologically reliable model solutions. Adaptations to traditional local inversions, for example, by using different structural and/or geostatistical constraints, may help to retrieve sharper model solutions. In addition, layer-based model parameterization in combination with local or global inversion approaches can be used to obtain models with sharp boundaries.

In this thesis, I study three typical layered near-surface environments in which prior information is used to adapt 2D inversion strategies to favor layered model solutions. In cooperation with the coauthors of Chapters 2-4, I consider two general strategies. Our first approach uses a layer-based model parameterization and a well-established global inversion strategy to generate ensembles of model solutions and assess uncertainties related to the non-uniqueness of the inverse problem. We apply this method to invert ERT data sets collected in an inland coastal area of northern France (Chapter 2) and offshore of two Arctic regions (Chapter 3). Our second approach consists of using geostatistical regularizations with different correlation lengths. We apply this strategy to a more complex subsurface scenario on a local intermountain alluvial fan in southwestern Germany (Chapter 4). Overall, our inversion approaches allow us to obtain resistivity models that agree with the general geological understanding of the studied field sites. These strategies are rather general and can be applied to various geological environments where a layered subsurface structure is expected. The flexibility of our strategies allows adaptations to invert other kinds of geophysical data sets such as seismic refraction or electromagnetic induction methods, and could be considered for joint inversion approaches.

Zusammenfassung

Die ERT-Methode (Electrical Resistivity Tomography) wird häufig zur Untersuchung geologischer, geotechnischer und hydrogeologischer Probleme im Binnenland und in Gewässern wie beispielsweise Seen, Flüssen oder dem Meer eingesetzt. Das Ziel der ERT-Methode ist es, zuverlässige Widerstandsmodelle des Untergrunds zu erhalten, die in Bezug auf die Struktur des Untergrundes und dessen petrophysikalischer Eigenschaften interpretiert werden können. Die Zuverlässigkeit der resultierenden Widerstandsmodelle hängt nicht nur von der Qualität der erfassten Daten ab, sondern auch von der angewendeten Inversionsstrategie. Die Inversion von ERT-Daten führt zu mehreren Lösungen, die die gemessenen Daten gleich gut erklären. Typische Inversionsansätze basieren auf verschiedenen deterministischen (lokalen) Strategien, die verschiedene Glättungs- und Dämpfungsstrategien berücksichtigen, um die Inversion zu stabilisieren. Diese Strategien haben jedoch den Nachteil, möglicherweise auftretende scharfe Grenzflächen zu verwischen. Es gibt jedoch Szenarien, in denen der Untergrund durch Schichten mit scharfen Grenzflächen gekennzeichnet ist, die Schichten mit hohem Widerstandskontrast (z. B. bis zu mehreren Größenordnungen) voneinander trennen. Wenn Vorwissen (z. B. aus Aufschlüssen, Bohrungen oder anderen geophysikalischen Untersuchungen) auf scharfe Widerstandsvariationen hindeutet, kann es von Vorteil sein, die Parametrisierungs- und Inversionsstrategien anzupassen, um stabilere und geologisch zuverlässige Modelllösungen zu erhalten. Anpassungen traditioneller lokaler Inversionen, beispielweise durch die Verwendung verschiedener struktureller und/oder geostatistischer Bedingungen, können helfen, schärfere Modelllösungen zu erhalten. Zusätzlich kann eine schichtbasierte Modellparametrisierung in Kombination mit lokalen oder globalen Inversionsansätzen verwendet werden, um Modelle mit scharfen Grenzen zu erhalten.

In dieser Arbeit habe ich drei typische geschichtete oberflächennahe Umgebungen untersucht, in denen Vorabinformationen verwendet werden, um 2D-Inversionsstrategien so anzupassen, dass geschichtete Untergrundlösungen bevorzugt werden. In Zusammenarbeit mit den Co-Autoren der Kapitel 2-4 habe ich zwei allgemeine Strategien in Betracht gezogen. Unser erster Ansatz verwendet eine schichtbasierte Modellparametrisierung und eine gut etablierte globale Inversionsstrategie. Diese Strategie erzeugt Ensembles von Modelllösungen mithilfe derer die Unsicherheiten im Zusammenhang der Nicht-Eindeutigkeit des inversen Problems bewertet werden können. Wir wenden diese Methode an, um ERT-Datensätze zu invertieren, die in einem Binnenküstengebiet in Nordfrankreich (Kapitel 2) und vor der Küste zweier arktischer Regionen (Kapitel 3) gesammelt wurden. Unser zweiter Ansatz besteht darin, geostatistische Regularisierungen mit unterschiedlichen Korrelationslängen zu verwenden. Wir wenden diese Strategie auf ein

komplexeres Untergrundszenario an, das sich auf einen lokalen Schwemmfächer in einem Mittelgebirge im Südwesten Deutshclands umfasst (Kapitel 4). Insgesamt ermöglichen uns unsere Inversionsansätze, Widerstandsmodelle zu erhalten, die mit dem allgemeinen geologischen Verständnis der untersuchten Feldstandorte übereinstimmen. Diese Strategien sind allgemeingültig und können in verschiedenen geologischen Umgebungen angewandt werden, in denen eine geschichtete Struktur des Untergrunds zu erwarten ist. Zudem erlaubt es die Flexibilität unserer Strategien, dass diese an die Inversion anderer geophysikalischer Datensätze wie seismischer Refraktionsmessungen oder elektromagentischer Induktionsverfahren angepasst werden können. Außerdem könnten solche Strategien für gemeinsame Inversionsansätze in Betracht gezogen werden.

Declaration

I, Mauricio Arboleda Zapata, doctoral student at the university of Potsdam with matriculation number 799869, declare that this cumulative thesis has not previously been submitted to any other university and that it has been prepared independently and exclusively with the specified resources.

Acknowledgements

I want to thank Dr. Jens Tronicke for his patience, guidance, and support during all my doctoral studies. He always put me back on track when I was getting a bit lost. He is a wonderful person and scientist who further deepened my passion for geophysical data inversion and its applications.

I am grateful to Dr. Oliver Korup for sharing his knowledge and passion for geomorphology and data science. He gave me another point of view and a better understanding of near-surface processes.

I appreciate all the time I spent with my colleagues in the Applied Geophysics group, and I want to thank Philipp, Tim, Niklas, Erika, Julien, Marko, and Shopie for spending some time with me and showing me some aspects of the German culture.

I also want to thank my colleagues from the Geohazards group: Georg, Chris, Melanie, Lisa, Eli, Eric, Maria, and Joaquin. I enjoyed our weekly meetings and the small talks. I learned a lot from all of you.

I appreciate all the support I received from the staff of the NatRiskChange Training Group, the Institute of Geosciences, and the Welcome Center. They made it possible to facilitate all administrative processes within the well-known German bureaucracy.

This thesis is the result of multiple collaborations. Therefore, I am very grateful for all the contributions of the co-authors and anonymous reviewers of the manuscripts I present in this thesis. Additionally, I want to thank Philipp Koyan, David Naranjo, and Alice Nocquet for reviewing some sections of this thesis.

This thesis is dedicated to my parents, Marleny Zapata and Luis Arboleda, and my siblings, Alex, Mario, Sandra, and Mary, for all their support during all these years of academic preparation. This thesis is also dedicated to my girlfriend, Alice, who kept me strong and encouraged me until the end.

Contents

1 Introduction **1**

1.1 The electrical resistivity tomography method 1

1.2 Inversion 4

1.3 Investigating layered environments 7

1.4 Objectives and outline of this thesis 9

2 A comprehensive workflow to analyze ensembles of globally inverted 2D electrical resistivity models **11**

2.1 Introduction 12

2.2 Methodology 14

2.2.1 Generating an ensemble of solutions 14

2.2.2 Model selection process 16

2.2.3 Interpolation to a common mesh 17

2.2.4 Cluster analysis 17

2.2.5 Analyzing sets of models 18

2.2.6 Analyzing sets of data residuals 19

2.3 Case studies 19

2.3.1 Synthetic example 19

2.3.2 Field example 23

2.4 Discussion 28

2.5 Conclusions 32

3 Exploring the capabilities of electrical resistivity tomography to study subsea permafrost **33**

3.1 Introduction 34

3.2 Study sites 36

3.2.1 Regional setting of Bykovsky Peninsula 36

3.2.2 Regional setting of Drew Point 37

3.3 Data acquisition 37

3.4 Methodology 40

3.4.1 2D layer-based model parameterization 40

3.4.2 Inversion strategy 41

3.4.3 Ensemble interpretation 42

3.4.4 1D inversion 42

3.4.5 Sensitivity analysis 43

3.5 Results 43

3.5.1 Bykovsky . . . 44
3.5.2 Drew Point . . . 49
3.6 Discussion . . . 54
3.6.1 Insights from our parameterization and inversion strategies . . . 55
3.6.2 Parameter learning from 1D inversion . . . 57
3.6.3 System understanding with sensitivity analysis . . . 58
3.6.4 Subsea permafrost features (Bykovsky vs. Drew Point) . . . 59
3.7 Conclusions . . . 61
3.8 Appendix - Smooth inversion . . . 61

4 Tracing past extreme floods on an alluvial fan using geophysical surveying 63
4.1 Introduction . . . 64
4.2 Study area . . . 65
4.3 Geophysical surveying . . . 67
4.3.1 Electromagnetic induction (EMI) . . . 68
4.3.2 Electrical resistivity tomography (ERT) . . . 70
4.3.3 Ground-penetrating radar (GPR) . . . 72
4.4 Discussion . . . 75
4.4.1 Past hydro-geomorphic events recorded in the Grimmbach fan . . . 75
4.4.2 Independent evidence . . . 77
4.5 Conclusions . . . 79

5 General discussion and conclusions 81

Bibliography 84

1

Introduction

Direct observations from outcrops and boreholes are key to studying and understanding different near-surface environments. However, outcrops may be scarce, have unrevealing orientations, and be far from our study area (Hickin et al., 2009). In contrast, borehole soundings can be performed at selected locations and provide detailed vertical records of the subsurface geology; nevertheless, they only provide punctual information. Therefore, creating interpolations and extrapolations in vertical and horizontal directions based on available outcrops and boreholes might be inadequate (Bazin and Pfaffhuber, 2013; Nickschick et al., 2019), especially in highly heterogeneous environments such as braided sedimentary systems (e.g., Hermans and Irving, 2017; Klingler et al., 2020).

To complement the understanding of the spatial variation of the subsurface configuration, indirect observation using near-surface geophysical techniques, with investigation depths of up to 30 m (as in our later shown examples), can reveal the general stratigraphy and hydrogeological conditions. Among the most used geophysical imaging techniques to study the near-surface structure and/or composition are different electric, electromagnetic, and seismic methods (Day-Lewis et al., 2005; Reynolds, 2011; Everett, 2013). Because this thesis focuses on the electrical resistivity tomography (ERT) method applied to layered sedimentary environments, I first introduce some general background of the ERT method, followed by a revision of typical inversion approaches and their adaptations to investigate layered geological environments. Finally, I present the main objectives and an outline of this thesis.

1.1 The electrical resistivity tomography method

The ERT method has been broadly used to estimate the distribution of subsurface resistivity (or its reciprocal electrical conductivity) and has been successfully applied to different geological, geotechnical, hydrogeological, and environmental problems (e.g., Dahlin, 2001; Loke et al., 2013). The resistivity of subsurface materials depends on porewater fluids, porosity, bulk rock composition, temperature, and particle's size, shape, and orientation, which typically varies within different geological layers (e.g., Revil and Glover,

1998; Rey and Jongmans, 2007; Shevnin et al., 2007; Kang and Lee, 2015; Wu et al., 2017). Therefore, the ERT method is a suitable tool to investigate the content, composition, and state of the water (e.g., Robinson et al., 2008; Garré et al., 2012; Wagner et al., 2019); the grain size distribution (e.g., Baines et al., 2002; Hickin et al., 2009; Gonzales Amaya et al., 2019; Schoch-Baumann et al., 2022); and the general subsurface composition and structure (e.g., Gourry et al., 2003; Hirsch et al., 2008; Schrott and Sass, 2008). In resistivity surveying, the standard workflow consists of data collection, processing, inversion, and interpretation.

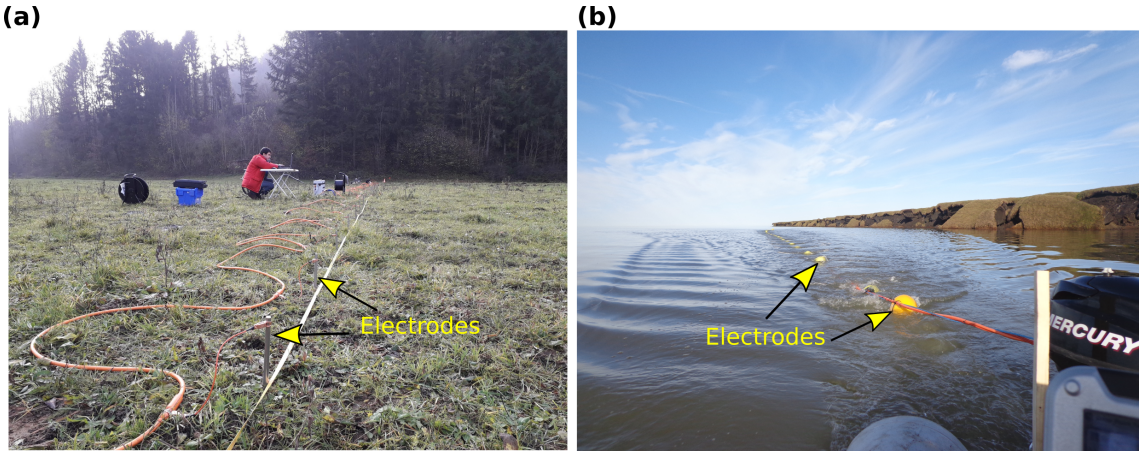

Fig. 1.1. 2D ERT data collection in (a) inland (source: Julien Guillemoteau) and (b) offshore (source: Michael Angelopoulos) field sites.

To collect 2D ERT data, an array of typically equally spaced electrodes are coupled to the ground or water along a straight profile line (Fig. 1.1a and b). An electrical current is injected into the ground using two current electrodes (A and B in Fig. 1.2) and the voltage is measured in two voltage electrodes (M and N in Fig. 1.2). Here, this set of four electrodes is referred to as a quadripole. In Fig. 1.2, the electric current flows from electrode B (source) to A (sink) which generates different voltages recorded by electrodes M and N. By repeating such measurements considering different quadripoles along a profile line, we can investigate different subsurface sections. To obtain the distribution of the apparent resistivities, we need to calculate the product between the measured impedances (i.e., injected current divided by the measured voltage) and the geometric factors (Rücker et al., 2006; Günther et al., 2006), which are in function of the relative distances between electrodes for each considered quadripole (e.g., Reynolds, 2011). The measured apparent resistivity data are typically visualized as pseudosections where the horizontal axes represent the center position of each quadripole and the vertical axes the relative penetration or levels (i.e., deeper levels often indicate larger penetration depths). Although 2D ERT data is collected along a profile line, we should be aware that every measured apparent resistivity depends on the resistivity distribution of a 3D volume. Therefore, to reduce the influence of 3D resistivity variations, 2D ERT

profiles should be perpendicular to the strike of the major structures (Loke et al., 2013).

Within the most popular acquisition configurations in 2D ERT surveying are symmetric array configurations such as Wenner and Schlumberger configurations. In these array configurations, the potential electrodes are located in the center while the current electrodes are on the outer sides (see Fig. 1.2). When the distance between the neighboring electrodes (A-M, M-N, and N-B) are equal, this corresponds to the Wenner array configuration. If the distance between M-N is smaller than between A-M and N-B is called the Schlumberger array configuration. The mix of these geometric configurations results in the Wenner-Schlumberger array configuration, which was adopted to acquire our ERT data in our later shown examples. For more details regarding these and other standard array configurations and their associated sensitivity distributions, please refer to Furman et al. (2003), Dahlin and Zhou (2004), and Stummer et al. (2004).

The acquisition strategy differs for ground-based and aquatic ERT surveys. In ground-based ERT surveys, the measurements are typically collected using stainless-steel stakes at fixed positions. Moving a subset of electrodes from the beginning to the end of the profile (roll-along) allows for extending the length of the profile while keeping similar investigation depths; i.e., when having comparable subsurface resistivity distributions. ERT data acquisition in water bodies (e.g., sea, lake, or river) is often performed using floating graphite electrodes that allow for continuous resistivity profiling; i.e., while the boat pulling the electrode streamer is in motion (e.g., Day-Lewis et al., 2006; Overduin et al., 2012; Befus et al., 2014; Hermans and Paepen, 2020). Another acquisition approach is to deploy electrodes on the water bottom, which is used to decrease the effect of current channeling under saltwater conditions (e.g., Befus et al., 2014).

After data collection, data with a low signal-to-noise ratio may be removed to avoid artifacts during data inversion (e.g., Zhou and Dahlin, 2003; Coscia et al., 2011). We can derive data quality indicators (e.g., standard deviation) from repeated and/or reciprocal measurements (e.g., Zhou and Dahlin, 2003; Nickschick et al., 2019). Repeated measurements are acquired considering the same position of the current and voltage electrodes, while reciprocal measurements reverse the position of the current and voltage electrodes. Repeated/reciprocal data are not always performed to reduce acquisition time or logistic difficulties (e.g., during continuous resistivity profiling). Still, when acquired, they provide helpful information to estimate data errors and filter bad-quality data points (i,e., values larger than an expected noise level). In addition, such error estimations can be used later as weighting factors during inversion; e.g., data points with less variation may have a more significant influence during inversion (e.g., Günther et al., 2006). However, we should be aware that such error estimations are not always accu-

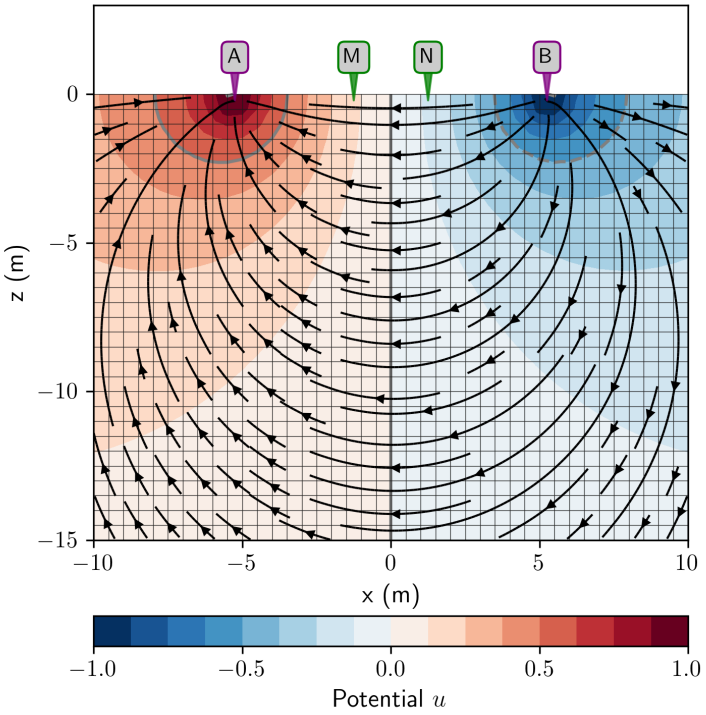

Fig. 1.2. Normalized potential distribution after applying a constant current and considering a homogeneous half-space resistivity. The labels A and B represent the current electrodes, and M and N are the voltage electrodes. The current flow is presented as simplified streamlines and the voltage as discretized colors from -1 and 1. Modified from pyGIMLi (https://www.pygimli.org/).

rate, as there may be other sources of noise that are not revealed by repeated/reciprocal measurements (Zhou and Dahlin, 2003). Another approach might consist in removing data with large geometrical factors or low recovered voltages (e.g., Ronczka et al., 2015). Once the low-quality data points have been removed, the remaining apparent resistivities are inverted. Coscia et al. (2011) used a two-step approach to remove low-quality data points. After a first inversion, they remove data points whose residuals are greater than five times the standard deviation of the distribution of the residuals, and the inversion is performed again. Furthermore, one might resample the original data set (e.g., by using a bootstrap approach) to create sub-sets of data points that are inverted and analyzed to infer possible errors introduced into the model by data noise while also providing hints about feature robustness (Schnaidt and Heinson, 2015). A brief overview of some inversion strategies is presented in the following section.

1.2 Inversion

The inversion of ERT data is an ill-posed problem; i.e., a set of model solutions (ensemble) describes the data equally well in terms of data fit (Ramirez et al., 2005; Fernández-Martínez et al., 2017; Aleardi et al., 2021b). To solve the inverse problem in geophysics, deterministic or local (e.g., Gauss-Newton and conjugate gradient) and stochastic or

global (e.g., genetic algorithms and particle swarm optimization) methods are often used (Aster et al., 2013; Sen and Stoffa, 2013). For this, the space is discretized considering unstructured and structured meshes. The main limitation of structured grids is that it needs to add a large number of mesh cells when having abrupt topography and subsurface interfaces. In contrast, unstructured meshes allow for local mesh refinement in areas of interest (e.g., subsurface interfaces) without significantly increasing the number of mesh cells. Libraries like Triangle (Shewchuk, 1996) and Tetgen (Si, 2015) allow for rapid creation of unstructured meshes and have boosted geophysical software development like the Python library pyGIMLi (Rücker et al., 2017), which is used to process and invert our later shown 2D ERT examples.

During the optimization process, the resistivities of each cell or a set of cells (e.g., layer-based model parameterization, in the following abbreviated as LBMP) are updated in every iteration until it results in data misfit values comparable with the expected noise level. Typical measures of data misfit are the L_1 norm (sum of the absolute values of the data residuals), L_2 norm (square root of the sum of the squares of the data residuals), and chi-square (sum of the squares of the ratio between data residuals and data errors). Models obtained using the L_1 norm often result in models with sharper resistivity contrasts than when using the L_2 norm (Loke et al., 2003; Auken and Christiansen, 2004; Barboza et al., 2018). Additionally, the L_1 norm is more robust in the presence of noise and data outliers (Fernández-Martínez, 2015). On the other hand, Günther et al. (2006) suggests that chi-square misfit values between 1 and 5 result in reliable models without overfitting or underfitting the data. Updating the model in a cell-wise fashion may result in a highly non-unique problem where many models might not be realistic regarding geological structures. Therefore, different regularization strategies are employed in most local inversion approaches.

Local inversion approaches with different regularization schemes (i.e., based on smoothing and damping strategies) favor minimum structure models by keeping small differences between resistivity values of neighboring cells and from a reference model (e.g., Loke and Barker, 1996; Günther et al., 2006). Applying such regularization schemes results in more stable model solutions while decreasing the non-uniqueness of the inverse problem. Furthermore, adaptations of smooth inversions of ERT data allow constraining the inverse problem by weighting the model parameters by known resistivity values (e.g., from well log measurements) or boundaries derived from geological and/or other kinds of geophysical methods (e.g., Bazin and Pfaffhuber, 2013). Adding prior information may help to obtain more realistic model solutions. For example, the water resistivity and bathymetric profiles are often measured during aquatic surveys using conductivity meter and echo sounder devices, respectively. Such information can be used to fix or

allow small variations of the resistivity and depth of the water layer during inversion (e.g., Overduin et al., 2012; Angelopoulos et al., 2019). Similarly, we could also include interfaces derived from other geophysical methods like ground-penetrating radar (e.g., Doetsch et al., 2012) and seismics (Bergmann et al., 2014; Ronczka et al., 2017).

One limitation of smooth inversion approaches (with isotropic constraints) is that these yield structures with comparable horizontal and vertical sizes. However, this is not a typical case for many near-surface geological environments where the lateral extent of different geological units can be more than an order of magnitude larger than their vertical extent as reported in alluvial systems (e.g., Gelhar, 1993). To favor model solutions with structures with different horizontal/vertical ratios, one strategy is weighting the spatial derivative to control the degree of smoothness in different directions (e.g., Coscia et al., 2011). In addition, geostatistical constraints might help to guide the inversion results for structures with different correlation lengths in the horizontal and vertical directions (Jordi et al., 2018).

When inverting ERT data, the objective function topography is typically characterized by several hills and valleys. Models falling in the same topography region have similar models in terms of the data misfit, general structure, and resistivity distribution (e.g., Ramirez et al., 2005; Fernández-Martínez et al., 2017). The objective function topography is typically smoothed by local inversion approaches, which requires a good starting model to converge to a plausible solution (Sen and Stoffa, 2013). In contrast to local inversion approaches, global inversion strategies do not rely on gradient-based strategies, and the starting model is usually randomly defined. Therefore, to better study and characterize the solution space, different global inversion approaches could be used instead.

Repeating several inversion runs to generate multiple model solutions (ensemble) using a global inversion algorithm will likely converge into different valleys of the objective function topography (i.e., equivalent model solutions). Additionally, we can use cluster analysis to obtain equivalent model solutions (clusters) from the original ensemble of model solutions (e.g., Ramirez et al., 2005; Fernández-Martínez et al., 2017). To summarize the information of each cluster, we can use different statistical descriptors; for example, the central trend can be described by using the mean or the median, and the variability by using the standard deviation or the interquartile range (e.g., Ramirez et al., 2005; Fernández-Martínez et al., 2017; Aleardi et al., 2021a,b). These statistical descriptors might be calculated in a pixel-wise fashion or by adapting more advanced approaches like structural similarity attributes commonly used in time-lapse geophysical experiments (e.g., Allroggen and Tronicke, 2016).

It is well known that global inversion algorithms are computationally expensive because they typically require evaluating the forward operator thousands of times for every inversion run (i.e., until we reach a certain misfit value or a number of iterations). Therefore, it is always wished to have a reduced number of model parameters to speed up conversion rates. It is important to consider that model reduction simplifies the topography of the cost function, reducing the variability within a set of plausible model solutions, but it compromises the model resolution (Fernández-Martínez, 2015; Grana et al., 2019). For example, Vinciguerra et al. (2022) used discrete cosine transform (DCT) to describe ERT models with a reduced number of parameters and perform inversion using a differential evolution Markov chain sampling strategy. Although results are comparable to those from traditional smooth inversion approaches, their strategy also allows for recovering model uncertainties. Similar compression strategies to DCT are the wavelet discrete transform and the Chebyshev discrete transform (Fernández-Martínez, 2015). Alternative to these compression strategies, LBMP can also significantly reduce the number of model parameters while favoring sharp subsurface resistivity distributions as often found in many geological environments (e.g., Auken and Christiansen, 2004; Akça and Basokur, 2010; De Pasquale et al., 2019).

1.3 Investigating layered environments

Near-surface geological environments typically consist of different layers, which are likely characterized by different resistivity distributions. Therefore, the ERT method can be a valuable tool for investigating such layered subsurface configurations. As illustrated above, local inversion methods typically result in smoothed model solution where any naturally occurring interface is smeared out (e.g., De Pasquale et al., 2019). However, user-specified resistivity thresholds based on additional field data or the expertise of the interpreter can be used to infer sharp interfaces that separate different subsurface units. For example, Overduin et al. (2016) and Angelopoulos et al. (2019) studied two subsea permafrost field sites and suggested that the depth to the ice-bearing permafrost table (IBPT) is defined for an approximate value of resistivity between 10 Ωm and 100 Ωm. In a similar fashion (but considering models with different resistivity distributions and user-defined thresholds), Hilbich et al. (2022) studied the contact between unfrozen and frozen sediments in high mountain areas; Beauvais et al. (2004), Giao et al. (2008), and Clair et al. (2015) distinguished regolith from unweathered bedrock; Schrott and Sass (2008) and Crawford et al. (2015) delineated failure surfaces of landslides; Baines et al. (2002), Gonzales Amaya et al. (2019), and Hirsch et al. (2008) interpreted alluvial layers with different grain size distributions, and Ronczka et al. (2015) distinguished a freshwater-saltwater interface in an aquifer system.

Different image processing techniques might be applied to avoid defining arbitrary resistivity thresholds to interpret sharp interfaces in smooth models. For example, Hsu et al. (2010) used a laplacian edge detection algorithm to study the sediment fill above the bedrock in alluvial floodplain deposits. To study a similar geological setting, Chambers et al. (2012) employed an edge detection algorithm based on the first derivative of resistivity profiles while Ward et al. (2014) considered a distribution-based fuzzy c-means clustering strategy. The main drawback of these image processing methods is that their performance highly depends on the reliability of the inverted models, which might result in shifted and/or unrealistic interfaces. In this case, other approaches like constraining the smooth inversion or adapting the parameterization strategies might be more helpful.

Structural and petrophysical information can be used to constrain smooth inversions (e.g., Günther et al., 2006; Wagner and Uhlemann, 2021). For example, Nickschick et al. (2019) studied a sedimentary basin using a smoothness-constrained approach and, following Coscia et al. (2011), weighted the vertical gradients such that they are ten times less penalized than the horizontal gradients. Thus, they obtained more realistic layered structures as suggested by available borehole data. In addition, Jordi et al. (2018) used geostatistical regularizations to obtain more layered model solutions consistent with stratified and inclined calcareous rocks. Because correlation lengths of the resistivity model parameters are not often known, these authors suggested testing different reasonable correlation lengths and evaluating their impact in the final inverted model. Doetsch et al. (2012) included GPR reflection interfaces to invert ERT data decoupling the regularization across the interfaces to obtain sharp interfaces and, thus, characterize the layering in an alluvial aquifer. Thibaut et al. (2021) combined a smooth constraint solution and a minimum gradient support approach to derive sharp interfaces from ERT data. After applying this approach to a data set collected in a gold deposit, they distinguished sedimentary rocks from crystalline rocks and identified the mineralized areas. The reader is referred to Caterina et al. (2014) for a detailed comparison of different smoothness-constrained inversions.

Although smoothness-constrained inversions can provide layered resistivity models, they still smear plausible sharp interfaces. Alternatively, sharp interfaces can be obtained by using LBMP. For example, Olayinka and Yaramanci (2000) compared smooth and block inversion results. For the block inversion, these authors investigated the influence of using a two layers model as starting model to resolve sharp subsurface models associated with a waste dump deposit overlying bedrock. Additionally, Auken and Christiansen (2004) proposed a layered laterally constrained 2D inversion algorithm and illustrated its applicability to resolve alluvial sedimentary layers with different grain size distribu-

tions and the depth to bedrock. Considering borehole data, these authors demonstrated how such an approach outperforms traditional smooth inversion considering L_1 and L_2 norms. Juhojuntti and Kamm (2015) based on the parameterization strategy of Auken and Christiansen (2004) developed a method to jointly invert ERT and seismic refraction data. These authors showed that such a strategy helps separate the water table and bedrock interfaces. Alternatively, instead of using 2D inversion algorithms, Auken et al. (2005) proposed a 1D laterally constrained approach to invert resistivity data collected using continuous resistivity profiling. To demonstrate the applicability of this algorithm, these authors investigated a sedimentary environment where they separated sandy from clayey layers. This parameterization approach was later adopted by Angelopoulos et al. (2020b) to investigate the thawed and frozen sediments in an Arctic lagoon. A simple and interesting approach is proposed by Hoffmann and Dietrich (2004), who used a set of 1D resistivity model solutions to generate different starting models for local 2D ERT inversions. These authors suggested that the 1D model solutions could be used to support the interpretation of possible layered structures that were smeared during the 2D local inversion.

It is important to note that in terms of an objective function, the minimum-structure smooth inversion usually results in smaller data misfit than layer-based inversion due to more freedom to introduce heterogeneity, especially in the shallowest levels (Juhojuntti and Kamm, 2015). However, using LBMP has shown to be a powerful strategy to obtain realistic model solutions while decreasing the number of parameters which is attractive for different global optimization algorithms. For example, Akça and Basokur (2010) used a genetic algorithm and a LBMP consisting of interfaces defined by piecewise cubic Hermite interpolation to delineate the landfill area of a waste disposal site. De Pasquale et al. (2019) used an empirical-Bayes-within-Gibbs inversion algorithm using a model with one interface defined by connected nodes to image the regolith-bedrock interface.

1.4 Objectives and outline of this thesis

This thesis aims to illustrate the potential of different adapted inversion strategies for 2D electrical resistivity data to investigate and elucidate the general subsurface structure in layered near-surface environments. Additionally, this thesis aims to quantify the uncertainties associated with the non-uniqueness of the ERT inversion problem.

In Chapter 2, I propose a workflow to derive uncertainties of globally inverted ERT data associated with layered models. Using a three-layer synthetic model and a field example in an onshore coastal aquifer, I demonstrate that the non-uniqueness of the 2D ERT inversion problem can be addressed by (1) incorporating prior and geological

background information into the inversion procedure, (2) simplifying the parameterization strategy (e.g., LBMP), and (3) generating and analyzing an ensemble with multiple model solutions. To analyze the ensemble from step (3), I first use cluster analysis to group or cluster similar model solutions where the central trend models (e.g., median models) represent equivalent model solutions, and the variabilities (e.g., interquartile range model) represent the associated uncertainties.

In Chapter 3, I use the workflow developed in Chapter 2 to investigate layered subsea permafrost environments. In this Chapter, I investigate the capabilities of the ERT method to identify the interface defined by the thawed and frozen sediments in two Arctic regions with different environmental conditions (e.g., water depth and water resistivity). For this, I evaluate the impact of constraining the water layer depth and resistivity, which show, after sensitivity analysis, to be the parameters with the most significant influence during inversion.

In Chapter 4, I study the influence of applying different geostatistical regularizations to invert ERT data collected in a more complex subsurface scenario (i.e., in terms of the horizontal and vertical resistivity variations) on a local intermountain alluvial fan in southwestern Germany. Furthermore, I compare the ERT inversion results with electromagnetic induction and ground-penetrating radar models.

Finally, in Chapter 5, I discuss the main findings of this thesis and highlight possible research paths in the direction of global inversion and parameterization strategies to investigate layered subsurface environments.

2

A comprehensive workflow to analyze ensembles of globally inverted 2D electrical resistivity models

---

This chapter is published as:
Arboleda-Zapata, M., Guillemoteau, J., and Tronicke, J., 2022. A comprehensive workflow to analyze ensembles of globally inverted 2D electrical resistivity models, *Journal of Applied Geophysics*, 196, 104 512, https://doi.org/10.1016/j.jappgeo.2021.104512.

Abstract

Electrical resistivity tomography (ERT) aims at imaging the subsurface resistivity distribution and provides valuable information for different geological, engineering, and hydrological applications. To obtain a subsurface resistivity model from measured apparent resistivities, stochastic or deterministic inversion procedures may be employed. Typically, the inversion of ERT data results in non-unique solutions; i.e., an ensemble of different models explains the measured data equally well. In this study, we perform inference analysis of model ensembles generated using a well-established global inversion approach to assess uncertainties related to the non-uniqueness of the inverse problem. Our interpretation strategy starts by establishing model selection criteria based on different statistical descriptors calculated from the data residuals. Then, we perform cluster analysis considering the inverted resistivity models and the corresponding data residuals. Finally, we evaluate model uncertainties and residual distributions for each cluster. To illustrate the potential of our approach, we use a particle swarm optimization (PSO) algorithm to obtain an ensemble of 2D layer-based resistivity models from a synthetic data example and a field data set collected in Loon-Plage, France. Our strategy performs well for both synthetic and field data and allows us to extract different plausible model scenarios with their associated uncertainties and data residual distributions. Although we demonstrate our workflow using 2D ERT data and a PSO-based inversion approach, the proposed strategy is general and can be adapted to analyze model ensembles generated from other kinds of geophysical data and using different global inversion approaches.

2.1 Introduction

Electrical resistivity tomography (ERT) is a popular geophysical method typically used in different hydrological, geotechnical, environmental, geological, and engineering applications (Loke et al., 2013). In resistivity surveying, the standard workflow consists of data acquisition, processing, inversion, and interpretation. During 2D ERT data acquisition, two electrodes inject an electrical current into the ground while another pair of electrodes measure the voltage. Such quadripole configurations are performed at different positions and spacings along a profile to obtain a 2D pseudo-section of the apparent resistivities calculated from the measured voltages. The next step is data evaluation and processing, which typically consists of checking data quality and editing/filtering erroneous readings (e.g., related to electrode coupling problems). Subsequently, the filtered data are inverted to reconstruct a 2D resistivity model of the subsurface. Finally, inverted resistivity models are interpreted (e.g., in terms of geological structures) typically considering the sensitivity matrix (e.g., Oldenburg and Li, 1999; Furman et al., 2003) to exclude unresolved model areas from the interpretation.

According to Günther et al. (2006) and Loke et al. (2013), if the data set is incomplete, inconsistent, or noisy, the inverse problem is ill-posed and characterized by a non-unique solution; i.e., an ensemble of model solutions describes the data equally well (e.g., Fernández-Martínez et al., 2017; De Pasquale et al., 2019). Different approaches have been suggested to generate an ensemble of models that are consistent with a given geophysical data set. On the one hand, there are strategies that use local inversion routines considering different initial conditions (e.g., Vasco et al., 1996) and/or regularization parameters (e.g., Constable et al., 2015). On the other hand, there are strategies whose objective is to obtain solutions independent of starting models or regularization parameters using global optimization approaches. For example, such global inversion strategies are based on genetic algorithms (e.g., Stoffa and Sen, 1991; Akça and Basokur, 2010), particle swarm optimization (e.g., Shaw and Srivastava, 2007; Fernández-Martínez et al., 2010; Tronicke et al., 2012), simulated annealing (e.g., Rothman, 1985; Sen and Stoffa, 1991), and Monte Carlo methods (e.g., Tarantola, 2005; Cordua et al., 2012).

To analyze and interpret the generated ensemble of solutions, different approaches have been proposed in the literature. For example, Sen and Stoffa (1996) and de Groot-Hedlin and Vernon (1998) analyzed the correlation matrix to estimate the trade-off between individual model parameters. Sambridge (1999) used a neighborhood algorithm to resample the parameter space and, then, calculated the resolution matrix and the trade-off in the model parameter space. Tompkins et al. (2011) proposed a strategy

called cut-off maps which consists of a pixel-wise calculation of specific quantiles of the model ensemble. Tronicke et al. (2012), Fernández-Martínez et al. (2012), and Zhu and Gibson (2018) used statistical measures such as the ensemble mean or median to characterize the central tendency of the ensemble whose uncertainties are assessed through dispersion measures such as the standard deviation or the interquartile range. Furthermore, Hermans et al. (2015), Fernández-Martínez et al. (2017), and De Pasquale et al. (2019) applied probability maps to study the uncertainties for a particular range of model parameters such as resistivities associated, for example, with a specific geologic unit, and Scheidt et al. (2018) studied the variability of a set of models using orthogonal component analysis.

Whether to use the entire ensemble of solutions for posterior analysis or not, is a question that has been addressed in previous studies. Lomax and Snieder (1995) in a synthetic experiment of seismic dispersion curves apply a threshold criteria accepting the inverted models which are less than 0.85 times the applied noise level of the synthetic data to ensure suitable model solutions. Douma et al. (1996) and Douma and Haney (2013) used empirical orthogonal functions to reject the models that add the most variability to the ensemble. Alternatively, Vasco et al. (1996) and Sambridge (1999) consider all model solutions but introduce different weighting criteria to derive posterior statistics. Such an approach helps to consider information that may be contained in not converged models and, thus, might also be useful to guide resampling strategies (e.g., Sambridge, 1999). Barboza et al. (2018, 2019) proposed a quality measure for a set of solutions considering both the global error and the quantile 90 % of the residuals (i.e., the differences between the measured and calculated data). Vasco et al. (1996), Ramirez et al. (2005), and Fernández-Martínez et al. (2017) used cluster analysis strategies to group models that are similar to each other and, then, performed posterior statistical analysis for each cluster.

In this study, we adapt some of these ideas and propose a logical and unified workflow to interpret ensembles of 2D ERT inversion results. Our ensemble inference strategy starts with formulating a model rejection criterion that considers different statistical measures calculated from the residuals. Then, we evaluate the variability of the resulting reduced ensemble, including the identification of potential model groupings using cluster analysis. Finally, we assess model uncertainties including the structure of residuals for each identified group of models. To illustrate our workflow, we use a global inversion strategy for generating an ensemble of possible model solutions for two 2D ERT data sets. The first data set corresponds to a synthetic example created considering a three-layer input model, while the second one represents a field data set collected in a coastal environment in Loon-Plage, France.

2.2 Methodology

We summarize our workflow for ensemble interpretation in Fig. 2.1. In the first step, we create an ensemble of resistivity models representing possible solutions for the considered 2D ERT inverse problem. Then, we filter this ensemble considering a statistical analysis of the corresponding residual distributions. Previous to any further posterior analysis, we interpolate all models to a common mesh to allow for pixel-wise calculations and analyses. Next, we perform cluster analysis to group the models and their corresponding residual data. Finally, we use the models from each cluster to assess uncertainties using probability maps and statistical descriptors of the central tendency and dispersion. Similarly, we use the data residuals from each cluster to evaluate the residual distribution in a pixel-wise fashion using global statistical descriptors. In the following subsections, we explain each of these steps in more detail.

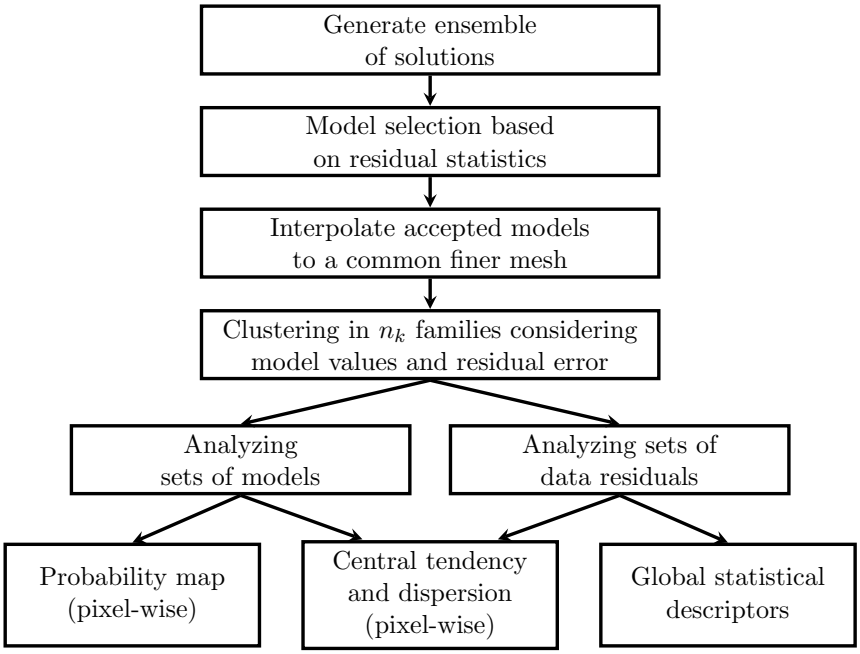

Fig. 2.1. Flow diagram illustrating the proposed interpretation strategy of model ensembles containing potential solutions of a 2D ERT inversion problem. The individual steps of this workflow are explained in more detail in Sections 2.2.1 to 2.2.6.

2.2.1 Generating an ensemble of solutions

To generate an ensemble consisting of n_m solutions (the first step in Fig. 2.1), we invert our 2D ERT data sets using a particle swarm optimization (PSO) algorithm considering a layer-based model parameterization as described in more detail by Tronicke et al. (2012) and Rumpf and Tronicke (2014, 2015). Our model parameterization relies on sums of arc-tangent functions (Roy et al., 2005), which represent the interfaces between individual layers. For a single interface, this can be written as

$$z(x) = z_0 + \sum_{j=0}^{n_{nod}} \Delta z_j \left(0.5 + \frac{1}{\pi} tan^{-1}\left(x - \frac{x_j}{b_j}\right)\right), \tag{2.1}$$

where z is the depth, n_{nod} is the number of arc-tangent nodes, z_0 is the average depth of the interface, x_j is the horizontal location of an arc-tangent node, and Δz_j is the vertical throw attained asymptotically over a horizontal distance of b_j. One advantage of this strategy is its flexibility because Eq. (2.1) allows the representation of various interface geometries including, for example, step-like or smooth variations with depth. When inverting 2D ERT data using this model parameterization, the number of model parameters n_{par} required to describe a resistivity model $\boldsymbol{m}$ consisting of n_{int} interfaces is given by

$$n_{par} = (n_{int} + 3\sum_{i=1}^{n_{int}} n_{nod_i}) + (n_{int} + 1), \tag{2.2}$$

where the first term indicates the number of parameters needed to describe the interface structure and the second term the number of homogeneous layers (i.e., layers with specific resistivity ρ). It should be noted that such a layer-based parameterization may introduce some bias, and some features may not be resolved (e.g., Rosas-Carbajal et al., 2014). However, if a priori information (e.g., regarding the geological settings) indicates a layered subsurface, such an approach may help to provide more realistic model solutions (e.g., Smith et al., 1999; Auken and Christiansen, 2004; Boiero and Socco, 2014; Juhojuntti and Kamm, 2015; De Pasquale et al., 2019) and to reduce the number of model parameters making it attractive for global inversion approaches such as the PSO-based strategy used in this study.

During PSO-based inversion, a swarm of particles explores the model-parameter space and the goodness of a model (i.e., parameter combination) is evaluated by a predefined objective function. Here, we use the root mean square logarithmic error RMSLE defined as

$$\text{RMSLE} = \sqrt{\frac{1}{n_d}\sum_{i=0}^{n_d} \boldsymbol{e}_i^2}, \tag{2.3}$$

where n_d is the number of data points, and $\boldsymbol{e}$ is the vector of residuals calculated by

$$\boldsymbol{e} = log(\boldsymbol{d}^{cal}) - log(\boldsymbol{d}^{obs}). \tag{2.4}$$

Here, $\boldsymbol{d}^{obs}$ represents the observed and $\boldsymbol{d}^{cal}$ the calculated data vector (note that $\boldsymbol{e}$ can be rewritten as $log(\boldsymbol{d}^{cal}/\boldsymbol{d}^{obs})$ which results in a dimensionless quantity). To obtain $\boldsymbol{d}^{cal}$, we use the forward operator as implemented in the software package BERT

(Günther et al., 2006; Rücker et al., 2006) considering an adaptive unstructured mesh (i.e., a new mesh is generated for each particle and for each iteration during the PSO-based inversion) that is created using the python library pyGIMLi (Rücker et al., 2017). During optimization, the PSO algorithm assesses two points of attraction; i.e., the best solution of each individual particle and the best solution of all particles. Together with some random perturbations, these control the movement of the particle swarm in the model parameter space. If the optimization meets a predefined stopping criterion, such as a threshold of the objective function or a maximum number of iterations, we save the final best model. By repeating the inversion using different seeds of the random number generator, we generate an ensemble of independent model solutions $\boldsymbol{M} = [\boldsymbol{m}_1, \boldsymbol{m}_2, ..., \boldsymbol{m}_{n_m}]$ and the corresponding residuals $\boldsymbol{\delta} = [\boldsymbol{e}_1, \boldsymbol{e}_2, ..., \boldsymbol{e}_{n_m}]$. Further details regarding this PSO-based global inversion strategy are given by Fernández-Martínez et al. (2010) and Tronicke et al. (2012). To evaluate if we obtained a representative ensemble of models, we inspect that there are no significant variations in the posterior correlation matrix after adding more model solutions to our ensemble as outlined by Sen and Stoffa (2013).

2.2.2 Model selection process

Although we employ a global inversion method, some optimization runs might not converge; i.e., get trapped in a local minimum and resulting in an inverted model with poorly fitted data. Considering these models in the posterior analysis could be misleading for the interpretation (e.g., Lomax and Snieder, 1995; Douma et al., 1996). Thus, we use a model selection criterion based on globally evaluating $\boldsymbol{\delta}$ (the second step in Fig. 2.1) considering the root mean square logarithmic error RMSLE($\boldsymbol{\delta}$), the interquartile range IQR($\boldsymbol{\delta}$), and the quantile 90 % $q_{90}(\boldsymbol{\delta})$. In the end, we accept models satisfying RMSLE($\boldsymbol{\delta}$) $\leq t_1$, IQR($\boldsymbol{\delta}$) $\leq t_2$, and $q_{90}(\boldsymbol{\delta}) \leq t_3$, where t_1, t_2, and t_3 are thresholds defined empirically or by considering error estimates from repetition or reciprocity measurements (e.g., Zhou and Dahlin, 2003). However, in our data sets such information is not available and, thus, we use histograms and scatter plots of RMSLE($\boldsymbol{\delta}$), IQR($\boldsymbol{\delta}$), and $q_{90}(\boldsymbol{\delta})$ as tools to estimate plausible thresholds values to remove those models and residuals from $\boldsymbol{M}$ and $\boldsymbol{\delta}$, respectively. A further complementary visualization strategy (not implemented in this study) could be to plot the cumulative distribution function which might be helpful to filter by a quantile criteria (e.g., accepting 80 % of the models in $\boldsymbol{M}$). These simple but informative visualization strategies may need some user validation, for example, by inspecting the models around the defined threshold. Once we are confident with the chosen threshold, we define a reduced set of accepted models $\boldsymbol{M}_{acc}$ and residuals $\boldsymbol{\delta}_{acc}$.

2.2.3 Interpolation to a common mesh

Our layer-based model parameterization strategy results in a different finite-element mesh for each model in $\boldsymbol{M}_{acc}$ (as needed by the used forward solver). To perform posterior statistical analyses, these models are interpolated (the third step in Fig. 2.1) using the nearest-neighbor technique on a densely discretized mesh; i.e., to ensure no critical loss of model resolution. Having all models with the same discretization allows us to perform pixel-wise calculations and analyses to derive, for example, the central trend and dispersion models.

2.2.4 Cluster analysis

We perform cluster analysis to identify and separate possible groups of models reflecting different subsurface scenarios. The most straightforward way to cluster the resulting model ensemble is to define the cluster input matrix as $\boldsymbol{K} = \boldsymbol{M}_{acc}$ (e.g., Fernández-Martínez et al., 2017). Alternatively, one could also set $\boldsymbol{K} = \boldsymbol{\delta}_{acc}$ in order to group models that show similar misfit distributions and patterns within the pseudo-section. Although these two strategies may provide reasonable results independently, in this study, we propose that defining $\boldsymbol{K}$ considering information from both $\boldsymbol{M}_{acc}$ and $\boldsymbol{\delta}_{acc}$ might potentially improve the clustering output (the fourth step in Fig. 2.1).

When clustering using $\boldsymbol{M}_{acc}$ and $\boldsymbol{\delta}_{acc}$ together, we have to consider resampling and rescaling (because $\boldsymbol{M}_{acc}$ and $\boldsymbol{\delta}_{acc}$ have different sizes and physical meanings) to ensure a well balanced influence from $\boldsymbol{M}_{acc}$ and $\boldsymbol{\delta}_{acc}$ on the result of cluster analysis. Typically, each model vector in $\boldsymbol{M}_{acc}$ is significantly larger than the number of corresponding data residuals. Therefore, if we consider $\boldsymbol{M}_{acc}$ and $\boldsymbol{\delta}_{acc}$ with their original sizes, the cluster output might be biased towards $\boldsymbol{M}_{acc}$. To avoid such a bias, we first resample the models in $\boldsymbol{M}_{acc}$ in to a set of vertical resistivity profiles to obtain comparable sizes of $\boldsymbol{M}_{acc}$ and $\boldsymbol{\delta}_{acc}$. Note that for a grid-based parameterization strategy, random resampling may be more appropriated than resampling along vertical profiles, also other resampling strategies might be considered, but they are out of the scope of this study. Furthermore, because $\boldsymbol{M}_{acc}$ values are given in Ωm and $\boldsymbol{\delta}_{acc}$ dimensionless, we standardize $\boldsymbol{M}_{acc}$ and $\boldsymbol{\delta}_{acc}$ such that they show a mean of zero and standard deviation of one. With this, our input matrix $\boldsymbol{K}$ is defined as the concatenation

$$\boldsymbol{K} = \boldsymbol{M}_{acc}^{r,s} \frown \boldsymbol{\delta}_{acc}^{s}, \tag{2.5}$$

where the superscripts r and s indicate resampled and scaled variables, respectively.

To perform a cluster analysis of $\boldsymbol{K}$, we use the well-known *k*-means algorithm (Mac-

Queen, 1967). In the *k*-means algorithm, we must pre-define the number of clusters n_k. To get a first idea of n_k, we use the variance ratio criterion (VRC) of Caliński and Harabasz (1974), which considers the relationship between the within-group average squared distances and the between-group average squared distances. Additionally, we inspect other reasonable values for n_k, for example, considering $n_k \pm 2$ after n_k is established using the VRC. This flexibility choosing n_k is helpful, for instance, to include a priori information or empirical knowledge in the interpretation. As the result of cluster analysis, we obtain n_k clustered families Fi (where $i = 1, 2, ..., n_k$) of models and corresponding sets of residuals denoted by $\boldsymbol{M}_{Fi}$ and $\boldsymbol{\delta}_{Fi}$, respectively.

2.2.5 Analyzing sets of models

Different statistical measures can summarize the information from a set of models (see the last two steps in Fig. 2.1). For example, we derive a representative (i.e., central tendency) model from a set of models $\boldsymbol{M}$ (e.g., $\boldsymbol{M}_{acc}$, $\boldsymbol{M}_{F1}$, or $\boldsymbol{M}_{F2}$) by calculating the median model $\mu_{1/2}(\boldsymbol{M})$ and estimate the variability within the set by the interquartile range IQR($\boldsymbol{M}$) as used, for example, by Tronicke et al. (2012) and Fernández-Martínez et al. (2012). We want to highlight that when using robust statistics (e.g., median), we are less affected by outliers than when using non-robust statistics (e.g., mean) and, thus, less sensitive to the thresholds defined in the model selection process (Section 2.2.2). Additionally, uncertainties for a specific resistivity range are assessed using probability maps as suggested, for example, by Hermans et al. (2015), Fernández-Martínez et al. (2017), and De Pasquale et al. (2019). Here, we estimate the probability P of a certain range of resistivities $P(\boldsymbol{M}, [\rho_{min}, \rho_{max}])$ by counting the cells in $\boldsymbol{M}$ falling in the specified resistivity range and dividing it by the number of models in $\boldsymbol{M}$. This interpretation tool is useful if there is a well-defined geophysical target; i.e., a layer in the subsurface characterized by well-constrained resistivity values. These statistical analyses are performed in a pixel-wise fashion considering that all models have the same discretization (Section 2.2.3).

A critical point when working with resistivity models and values, respectively, is to define whether the statistical calculations (e.g., $\mu_{1/2}(\boldsymbol{M})$ and IQR($\boldsymbol{M}$)) are performed on a linear or logarithmic scale. We perform a preliminary statistical analysis using both scales (also for our later shown examples) to decide which scale is more appropriate. We find that calculations using a linear scale typically favor smooth solutions. In contrast, we notice that when using a logarithmic scale, we favor more blocky solutions. Because in our examples we aim to image subsurface interfaces using a layer-based parameterization, we decide to use the logarithmic scale to perform all calculations needed by our statistical analyses.

2.2.6 Analyzing sets of data residuals

A careful analysis of the data residuals (see Eq. (2.4)) can provide further insights into the solutions of the formulated inverse problem; for example, to identify any systematic effects, outliers, or biases that may distort our inversion results (e.g., Zhou and Dahlin, 2003; Juhojuntti and Kamm, 2015; Constable et al., 2015). In this study, we derive the central tendency and dispersion from a set of data residuals $\boldsymbol{\delta}$ (e.g., $\boldsymbol{\delta}_{acc}$, $\boldsymbol{\delta}_{F1}$, or $\boldsymbol{\delta}_{F2}$) by a pixel-wise calculation of the median of the residuals $\mu_{1/2}(\boldsymbol{\delta})$ and the interquartile range of the residuals IQR($\boldsymbol{\delta}$), respectively. Additionally, in the same way as discussed in Section 2.2.2, we globally evaluate the statistical descriptors RMSLE($\boldsymbol{\delta}$), IQR($\boldsymbol{\delta}$), and $q_{90}(\boldsymbol{\delta})$ because they are useful to make comparisons between the clustered residuals (see the last two steps in Fig. 2.1). Finally, we also want to highlight that the clustered families may be further filtered using our model selection strategy (Section 2.2.2).

2.3 Case studies

We use two 2D ERT data sets to illustrate our workflow (Fig. 2.1). The first one is a synthetic example where we know the underlying input resistivity model and the noise level of the data. The second one is a field example where our geological background knowledge suggests a layered subsurface consisting of sedimentary layers with different pore fillings.

2.3.1 Synthetic example

Our synthetic input model consists of three layers (Fig. 2.2a). The uppermost layer represents a channel fill-like structure with $\rho = 300$ Ωm, the middle layer is a conductive layer with $\rho = 10$ Ωm, and the lowermost layer is characterized by $\rho = 200$ Ωm. To obtain the resistivity response of this model, we employ the BERT forward solver (Günther et al., 2006; Rücker et al., 2006) using a Wenner array configuration and 48 electrodes equally spaced in 1 m intervals along the surface. The simulated data set is contaminated by adding 0.01 of Gaussian noise (in terms of our objective function Eq. (2.3)) to simulate small-scale variabilities and noise as often observed in field data sets. In total, we obtain a pseudo-section with 360 apparent resistivity measurements as shown in Fig. 2.2b.

We invert our synthetic data using the layer-based global inversion strategy as described in Section 2.2.1. We use three interfaces (four layers) with four nodes for each interface resulting in a total of 43 model parameters (see Eq. (2.2)). To perform the global inversion, we use the PSO-based inversion strategy with a swarm size of 88 particles and save the best model after 400 iterations. These PSO parameters, as well as the

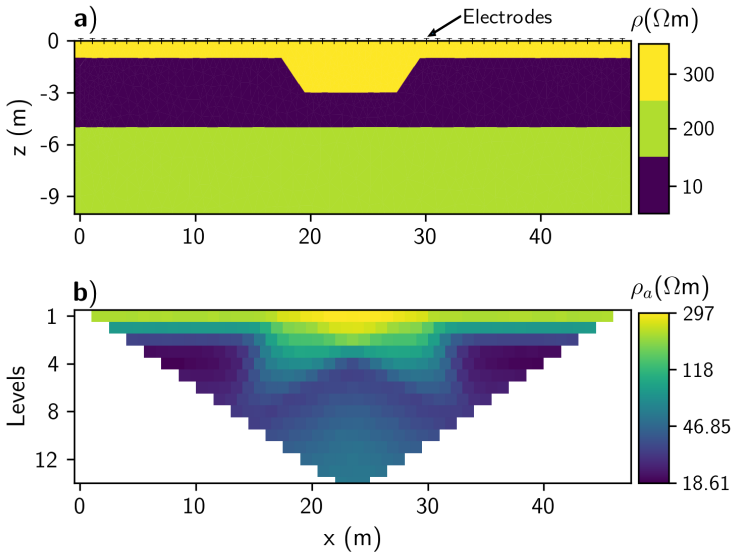

Fig. 2.2. (a) Synthetic input resistivity model indicating electrode positions along the surface and (b) synthetic apparent resistivity ρ_a data visualized as a Wenner pseudo-section.

model parameterization, are selected after some initial parameter testing. We repeated the inversion until we got a representative ensemble consisting of 1103 models.

To evaluate and filter the generated ensemble (Section 2.2.2), we explore possible threshold values using histograms and scatter plots of RMSLE($\boldsymbol{\delta}$), IQR($\boldsymbol{\delta}$), and $q_{90}(\boldsymbol{\delta})$ as shown in Fig. 2.3. From the histograms in Fig. 2.3a-c we notice a bimodal distribution in all variables. In order to reject models where the optimization may not have converged, we define upper thresholds (see the dashed vertical lines in Fig. 2.3a-c) to exclude models with rather high RMSLE($\boldsymbol{\delta}$), IQR($\boldsymbol{\delta}$), and $q_{90}(\boldsymbol{\delta})$ values, respectively. Then, we refine these threshold values using the scatter plots shown in Fig. 2.3d-f to select the models belonging to the main cloud of points. In Fig. 2.3d-f, we consider the smallest value of the statistical descriptor to define our model selection criteria. In the end, we accept models satisfying RMSLE($\boldsymbol{\delta}$) $\leq$ 0.019, IQR($\boldsymbol{\delta}$) $\leq$ 0.022, and $q_{90}(\boldsymbol{\delta}) \leq$ 0.028 resulting in 503 accepted models and residual vectors representing the ensembles $\boldsymbol{M}_{acc}$ and $\boldsymbol{\delta}_{acc}$, respectively. Furthermore, because the remaining 503 models in $\boldsymbol{M}_{acc}$ have different discretizations containing 4600$\pm$750 cells, we interpolate them to a finer common mesh with 16502 cells (see Section 2.2.3).

Having all models with the same discretization, we calculate $\mu_{1/2}(\boldsymbol{M}_{acc})$, IQR($\boldsymbol{M}_{acc}$), and $P(\boldsymbol{M}_{acc}, \rho \in$ [3, 15] Ωm$)$ to get a first impression regarding the characteristics of $\boldsymbol{M}_{acc}$ (Fig. 2.4a-c). Although the median model (Fig. 2.4a) represents a reasonable solution compared to the input model (Fig. 2.2a), we notice (when analyzing individual models) that some models show significant deviations from this median model; especially for depths $z <$ 5 m. Thus, to further analyze $\boldsymbol{M}_{acc}$ and to identify potential groups

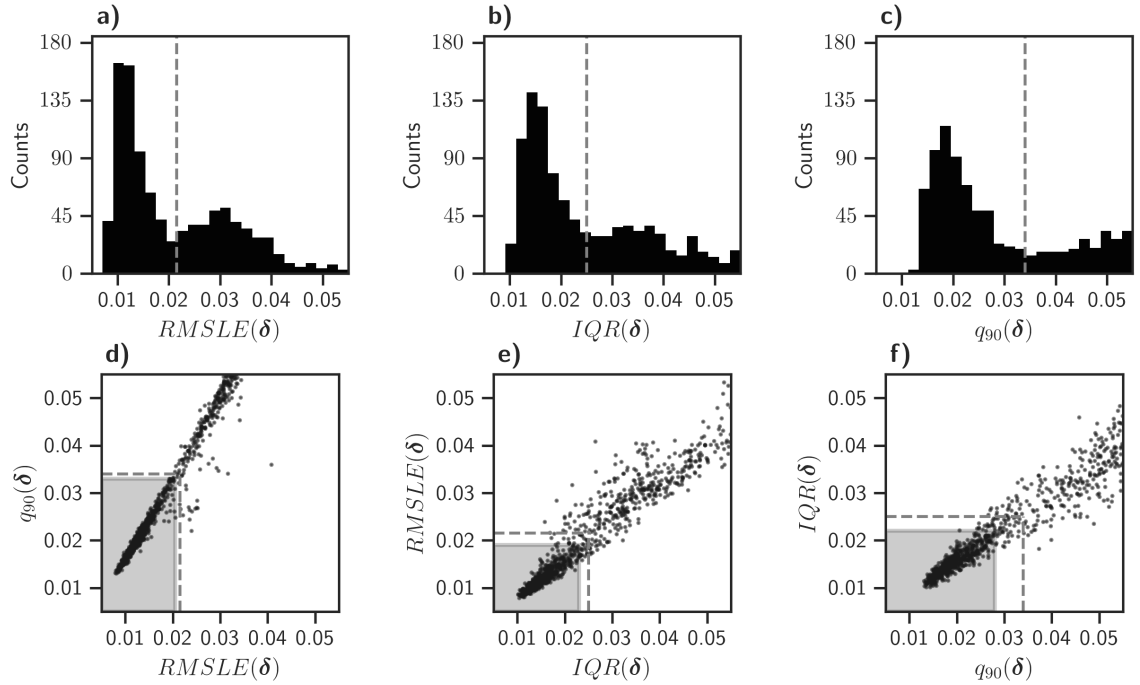

Fig. 2.3. Determination of the acceptance thresholds using RMSLE($\boldsymbol{\delta}$), IQR($\boldsymbol{\delta}$), and $q_{90}(\boldsymbol{\delta})$ to filter the initial model ensemble of our synthetic example. (a-c) Histograms indicating by the grey dashed lines the first estimation of the acceptance thresholds. (d-f) Scatter plots indicating by the grey rectangles the refined and final threshold values (note that the grey dashed lines highlight the thresholds defined by analysing the histograms). For visualization purposes, we limit all axis to fits up to 0.055.

of similar models, we perform cluster analysis taking into account $\boldsymbol{M}_{acc}$ and $\boldsymbol{\delta}_{acc}$ (see Section 2.2.4). Because each model in $\boldsymbol{M}_{acc}$ significantly differs in size to the corresponding residuals in $\boldsymbol{\delta}_{acc}$ (16502 versus 360 values, respectively), we resample each model in $\boldsymbol{M}_{acc}$ by extracting 18 vertical resistivity profiles (up to a depth of $z = 10$ m) located between $x = 8$ m and $x = 40$ m with a lateral spacing of 1.88 m resulting in 771 values for each model. Moreover, we standardize the resampled model values and residuals and define $\boldsymbol{K}$ according to Eq. (2.5). Using the VRC and visual inspection, we found that $n_k = 3$ (i.e., three model families F1, F2, and F3) is sufficient to describe the variability within our reduced model ensemble. With this, 199 models are assigned to F1, 139 to F2, and 165 to F3.

The central tendency, dispersion, and probability models for the clustered model families Fi are shown in Fig. 2.4d-l. All median models $\mu_{1/2}(\boldsymbol{M}_{Fi})$ (Fig. 2.4d, g, and j) indicate a three-layer solution. However, when comparing these models in more detail, we notice some differences in the structures of the lower boundary of the conductive layer and in the resistivity of the lowermost layer. Also the IQR($\boldsymbol{M}_{Fi}$) models (Fig. 2.4e, h, and k) indicate a three-layer case and highlight the variabilities around the layer interfaces. Because the conductive layer is the one controlling the resulting model structure (also our hypothetical target), we further investigate the uncertainties associated with this layer

using the probability map $P(\boldsymbol{M}_{Fi}, \rho \in [3, 15]\ \Omega\text{m})$ (Fig. 2.4f, i, and l). These maps show high probabilities on both sides of and below the central channel-like structure, and the probability decreases as we approach the bottom of the conductive layer.

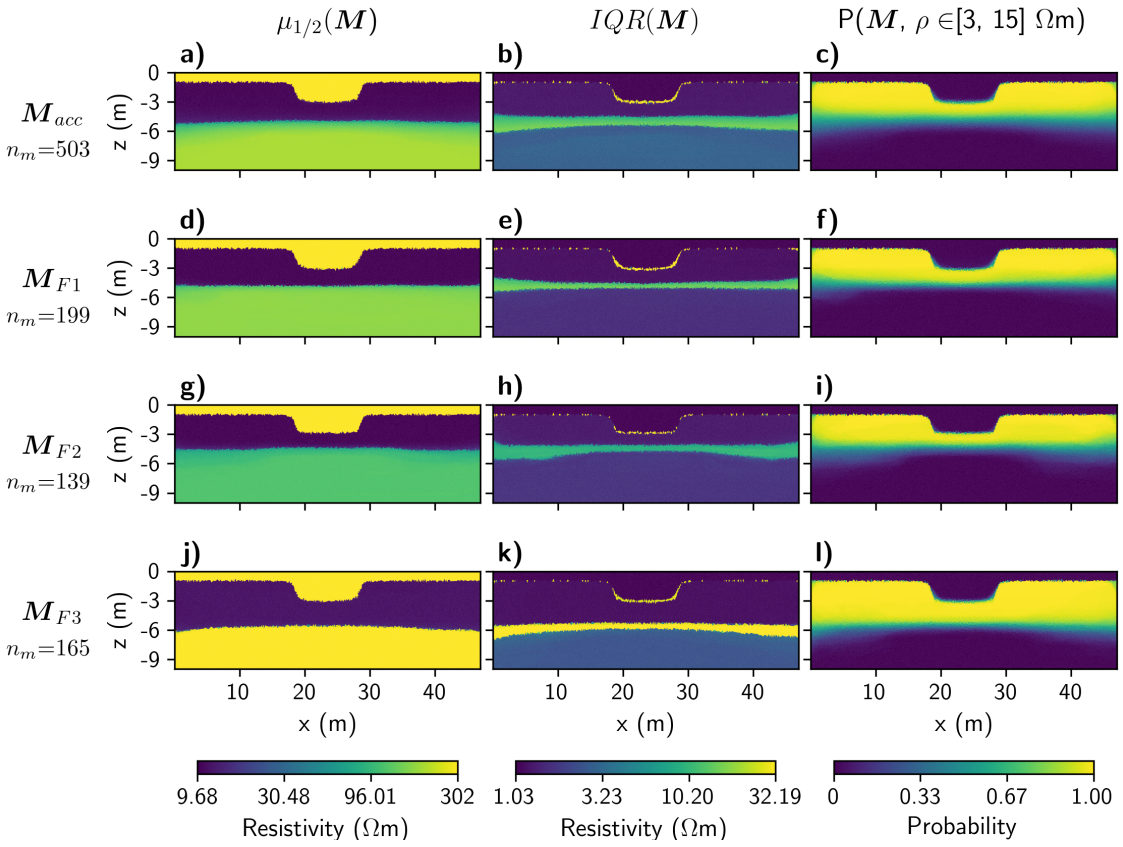

Fig. 2.4. Representation of the pixel-wise calculation of the $\mu_{1/2}(\boldsymbol{M})$, IQR($\boldsymbol{M}$), and $P(\rho \in [3, 15]\ \Omega\text{m})$ for our synthetic example. (a-c) statistics for the accepted models $\boldsymbol{M}_{acc}$ and (d-l) for the clustered families $\boldsymbol{M}_{F1}$, $\boldsymbol{M}_{F2}$, and $\boldsymbol{M}_{F3}$. n_m represents the size of each ensemble of models.

Furthermore, we analyze the corresponding sets of data residuals in a pixel-wise and global fashion (as outlined in Section 2.2.6). The pixel-wise representations of the central tendency and dispersion for all residuals $\boldsymbol{\delta}_{acc}$ and for each family of residuals $\boldsymbol{\delta}_{Fi}$ are shown in Fig. 2.5. The $\mu_{1/2}(\boldsymbol{\delta}_{Fi})$ pseudo-sections present similar patterns as $\mu_{1/2}(\boldsymbol{\delta}_{acc})$. This indicates that the models in these families fitted individual data points in a similar fashion, where the highest residuals are observed along diagonal lines around 18 m and 30 m in the first levels of the pseudo-sections. On the other hand, all IQR($\boldsymbol{\delta}_{Fi}$) pseudo-sections show similar variability patterns, while the IQR($\boldsymbol{\delta}_{acc}$) shows slightly higher values, especially in the central part. In Fig. 2.6, we additionally illustrate the global evaluation of the RMSLE, IQR, and q_{90} for $\boldsymbol{\delta}_{acc}$ and for all $\boldsymbol{\delta}_{Fi}$ by histograms. We see that the histograms of $\boldsymbol{\delta}_{F1}$ and $\boldsymbol{\delta}_{F3}$ show a similar shape compared to the histogram of $\boldsymbol{\delta}_{acc}$ in all three statistical measures. However, for $\boldsymbol{\delta}_{F2}$, the histograms of these measures are different and slightly shifted toward higher values (compared to all other histograms). Overall, this residual analysis indicates that the three families fit the data to equivalent

levels; i.e., if this was an actual field example, we could not distinguish the best family without any further information. However, if we consider the information of the known input model (Fig. 2.2a), we can conclude that F1 (Fig. 2.4d) represents the best family of models to solve our inverse problem. Although in this example we knew the noise level of our data, we decide to work with models that fit the data at lower and higher values than the added noise level. This avoids focusing on models suspected to under-fitting or over-fitting the data and, thus, ensures more detailed insights of the inverse problem (e.g., Vasco et al., 1993).

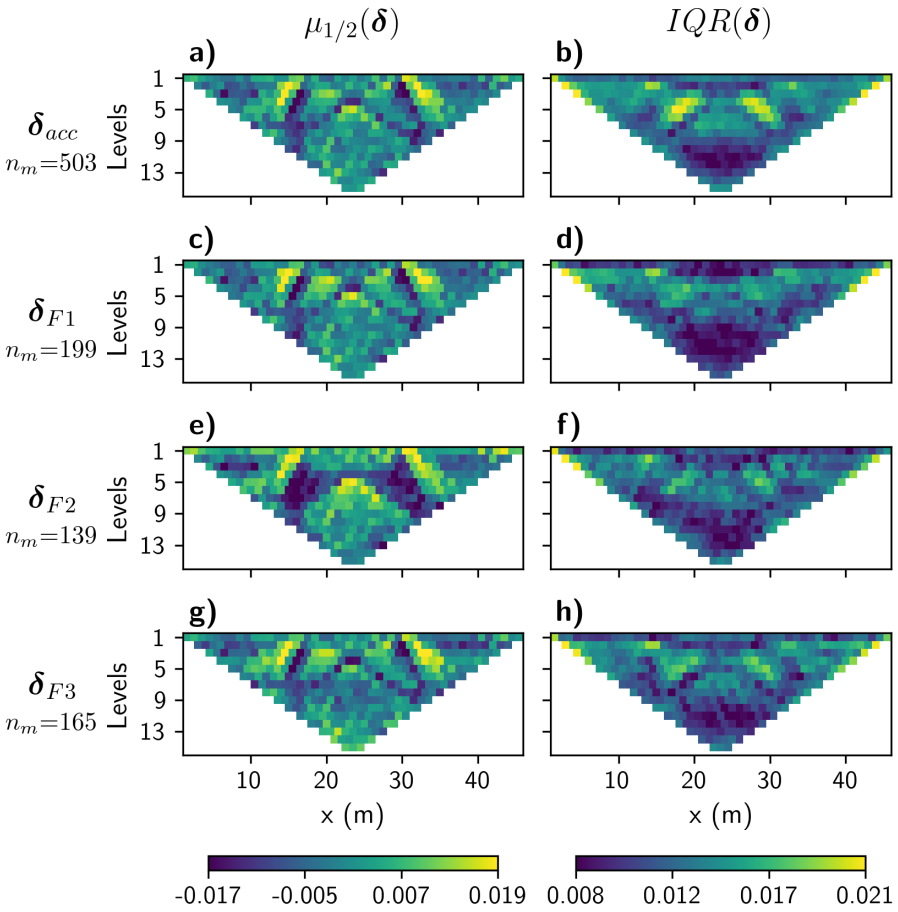

Fig. 2.5. Pseudo-section representation of the pixel-wise calculation of $\mu_{1/2}(\boldsymbol{\delta})$ and IQR$(\boldsymbol{\delta})$ for our synthetic example. (a-b) statistics for the accepted data residuals $\boldsymbol{\delta}_{acc}$ and (c-h) for the clustered families $\boldsymbol{\delta}_{F1}$, $\boldsymbol{\delta}_{F2}$, $\boldsymbol{\delta}_{F3}$. n_m represents the size of each ensemble of residual vectors.

2.3.2 Field example

In September 2019, we performed a 2D ERT survey in a coastal environment west of the town Loon-Plage, Northern France. This experiment was performed during an archaeological site evaluation by the French national institute for preventive archaeological research (INRAP), in the framework of the Port of Dunkirk extension project. To acquire our ERT data, we used 96 electrodes with a regular spacing of 2 m and collected

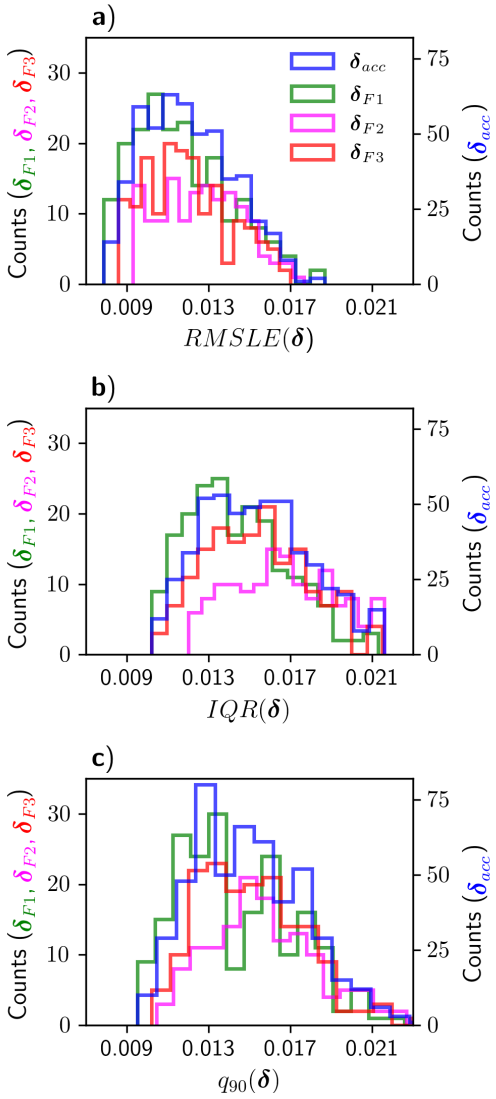

Fig. 2.6. (a-c) Histograms of the global statistical descriptors RMSLE($\boldsymbol{\delta}$), IQR($\boldsymbol{\delta}$), and $q_{90}(\boldsymbol{\delta})$ for the synthetic example. Notice that the corresponding counts of $\boldsymbol{\delta}_{F1}$, $\boldsymbol{\delta}_{F2}$, and $\boldsymbol{\delta}_{F3}$ are represented by the left axis, and of $\boldsymbol{\delta}_{acc}$ by the right axis. The legend in (a) also applies for (b) and (c).

our data using the Wenner array configuration. A single roll-along was performed by moving half of the electrodes. In the end, we recorded 2501 apparent resistivities along a 284 m long profile. After a first data quality evaluation, we removed the first level (186 data points) from the pseudo-section to reduce the influence of near-surface soil heterogeneities because the goal of this survey was to characterize deeper geological structures as needed to develop a hydrogeological understanding of this field site. In Fig. 2.7, we present the measured raw data.

Following our workflow, we invert our field data set using our layer-based model parameterization which is consistent with preliminary geological information of the study area. For example, Houthuys et al. (1993) describe the local geology as a transitional en-

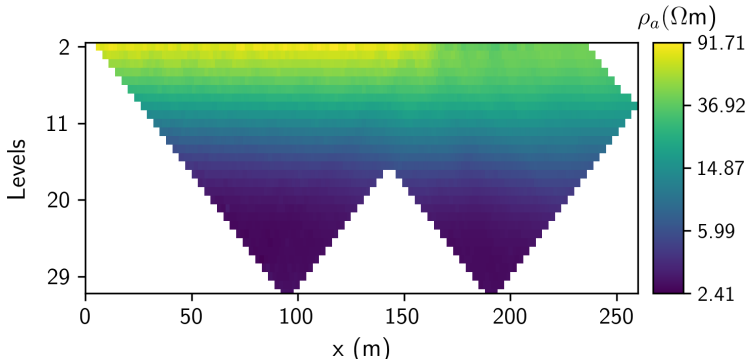

Fig. 2.7. Raw field data recorded at our field site in Loon-Plage, France using the Wenner array configuration.

vironment, where the first 15 m to 25 m of the subsurface is characterized by horizontally stratified sandy Holocene sediments with clayey and peaty intercalations. Considering this a priori information, we invert our data set using four interfaces and three nodes for each interface, resulting in 45 model parameters (see Eq. (2.2)). In the PSO, we use 50 particles and a stopping criterion of a maximum of 400 iterations. In the end, we generate an ensemble of 802 models using this inversion strategy.

Similarly to our synthetic study, we use the histograms and scatter plots shown in Fig. 2.8 to obtain the thresholds values t_1, t_2, and t_3 to remove models from the ensemble representing non-converged inversions runs (Section 2.2.2). As indicated in the plots of Fig. 2.8, we accept models satisfying RMSLE($\boldsymbol{\delta}$) $\leq$ 0.027, IQR($\boldsymbol{\delta}$) $\leq$ 0.03, and $q_{90}(\boldsymbol{\delta}) \leq$ 0.038 resulting in a reduced ensemble consisting of 744 models and residuals ($\boldsymbol{M}_{acc}$ and $\boldsymbol{\delta}_{acc}$, respectively). Furthermore, because the remaining 744 models in $\boldsymbol{M}_{acc}$ have different discretizations containing 4700$\pm$700 cells, we interpolate them to a finer common mesh with 75679 cells (see Section 2.2.3).

Having all models with the same discretization, we calculate $\mu_{1/2}(\boldsymbol{M}_{acc})$, IQR($\boldsymbol{M}_{acc}$), and $P(\boldsymbol{M}_{acc}, \rho \in [1, 3]\ \Omega m)$ as shown in Fig. 2.9a-c. From $\mu_{1/2}(\boldsymbol{M}_{acc})$ model (Fig. 2.9a), we learn that four layers (i.e., three interfaces) are sufficient to characterize the subsurface; i.e., two uppermost layers of approximately five meters thickness with a lateral contact at $x \approx$ 160 m, a layer at depths between $z \approx$ 5 m and $z \approx$ 10 m, and a lowermost layer below $z \approx$ 10 m. Furthermore, from the IQR($\boldsymbol{M}_{acc}$) model (Fig. 2.9b), we notice that the dominant variability is found at $z \approx$ 10 m, but there is also some variability associated to the overlying layer at depths between $z \approx$ 5 m and $z \approx$ 10 m. Additionally, when analyzing individual models (not shown here), we notice several models showing a layer at depths below 20 m with slightly increased resistivities compared to the overlying layer. To study this structure in more detail, we calculate $P(\boldsymbol{M}_{acc}, \rho \in$ [1, 3] $\Omega m)$ as shown in Fig. 2.9c where this resistivity range is defined after inspecting in more detail typical resistivities values (e.g., using histograms) of the deeper layers ($z <$ 10 m) for

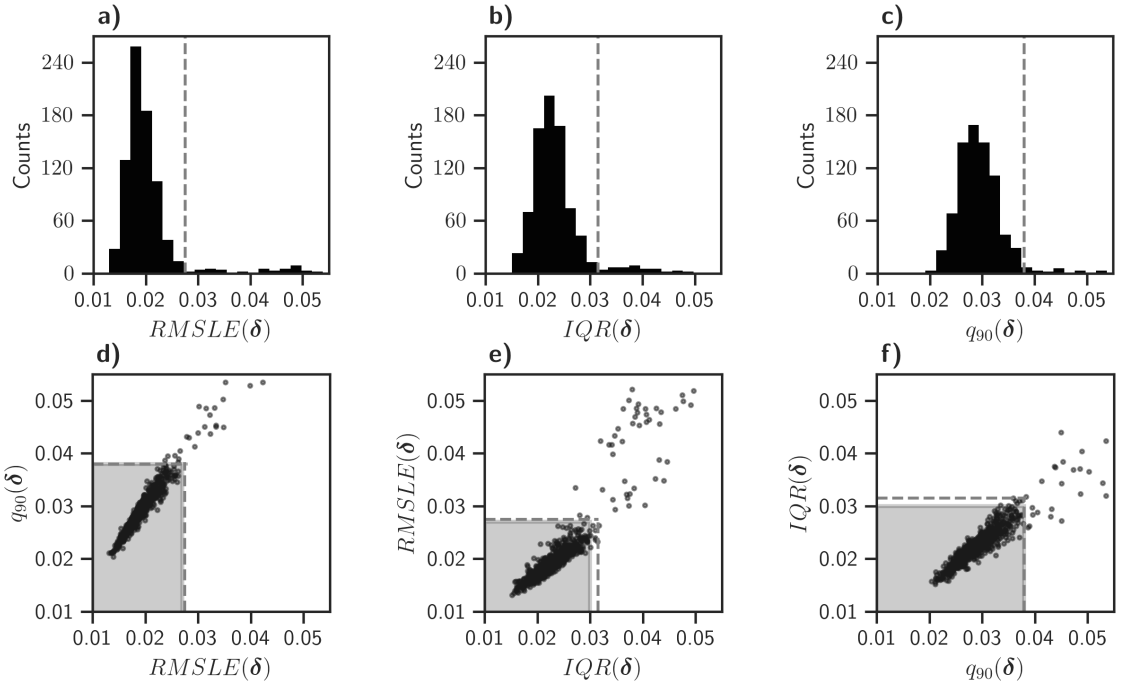

Fig. 2.8. Determination of the acceptance thresholds using RMSLE($\boldsymbol{\delta}$), IQR($\boldsymbol{\delta}$), and $q_{90}(\boldsymbol{\delta})$ to filter the initial model ensemble of our field example. (a-c) Histograms indicating by the grey dashed lines the first estimation of the acceptance thresholds. (d-f) Scatter plots indicating by the grey rectangles the refined and final threshold values (note that the grey dashed lines highlight the thresholds defined by analysing the histograms). For visualization purposes, we limit all axis to fits up to 0.055.

each ensemble. Note that choosing different resistivity ranges may be motivated by a well-defined geophysical target, which in our case is a saltwater-saturated layer characterized by the lowest resistivity values in our inverted models. Alternatively, we could have used other resistivity ranges, for example, $P(\boldsymbol{M}_{Fi}, \rho > 40\ \Omega\text{m})$ to study the near-surface structures in more detail if these model features are of interpretational interest. From the probability map, we notice, at depths between $z \approx 10$ m and $z \approx 23$ m, a probability of ~ 1. However, this probability slightly decreases below $z \approx 23$ m. The analysis of individual models and Fig. 2.9c indicates the existence of different groups of models describing different geological scenarios difficult to be identified by analyzing Fig. 2.9a-c. To further explore this, we perform cluster analysis as outlined in Section 2.2.4.

Before clustering, the models $\boldsymbol{M}_{acc}$ are resampled along 50 vertical resistivity profiles up to a depth of $z = 30$ m, laterally distributed between $x = 20$ m and $x = 260$ m with an equal spacing of 4.9 m. In total, we extract 3556 values for each model, which is comparable to the number of data and residuals points, respectively. Then, we standardize the resampled models and residual values to define $\boldsymbol{K}$ according to Eq. (2.5). In cluster analysis, by using the VRC and visual inspections, we find that three families (F1, F2, and F3) are sufficient to explain the data and to obtain a reasonable solution. Finally, we thus obtain a solution with 258 models in F1, 119 in F2, and 367 in F3.

The statistics of the clustered model families F_i are shown in Fig. 2.9d-l. The median models $\mu_{1/2}(\boldsymbol{M}_{Fi})$ (Fig. 2.9d, g, and j) suggest three different subsurface scenarios. For example, the median model $\mu_{1/2}(\boldsymbol{M}_{F1})$ (Fig. 2.9d) represents a resistive layer above $z \approx 10$ m including a ~ 5 m thick more conductive top layer for $x > 160$ m. In contrast, $\mu_{1/2}(\boldsymbol{M}_{F2})$ (Fig. 2.9g) and $\mu_{1/2}(\boldsymbol{M}_{F3})$ (Fig. 2.9j) represent a similar near-surface-structure, where above $z \approx 10$ m there is a more conductive layer embedding a more resistive top layer for $x < 160$ m. However, $\boldsymbol{M}_{F2}$ also shows a resistivity contrast at $z \approx 23$ m. Additionally, we infer the uncertainties associated with the layer interfaces in $\mu_{1/2}(\boldsymbol{M}_{Fi})$ calculating the IQR$(\boldsymbol{M}_{Fi})$ models (Fig. 2.9e, h, and k). From the IQR models, we learn that the main uncertainties are associated with the layer at $z \approx 10$ m, where, for example, we notice higher variations for $\boldsymbol{M}_{F1}$ than for $\boldsymbol{M}_{F2}$ and $\boldsymbol{M}_{F3}$. Furthermore, $\boldsymbol{M}_{F2}$ contains the highest increased variability for the layer at $z \approx 23$ m. Finally, we use $P(\boldsymbol{M}_{Fi}, \rho \in [1, 3]\ \Omega\text{m})$ to better explore the models at depths below $z \approx 10$ m (Fig. 2.9f, i, and l). Here, we observe that $\boldsymbol{M}_{F2}$ is most different compared with $\boldsymbol{M}_{F1}$ and $\boldsymbol{M}_{F3}$. This is in agreement with Fig. 2.9g, where we notice that the resistivity increases at depths below $z \approx 23$ m. In the hypothetical case that we are asked to identify the resistivity range that maximize the probability of the conductive layer, we would have to modify iteratively the resistivity range applied to $\boldsymbol{M}_{F2}$ (e.g., trying $P(\boldsymbol{M}_{F2}, \rho \in [3, 8]\ \Omega\text{m})$, $P(\boldsymbol{M}_{F2}, \rho \in [5, 10]\ \Omega\text{m})$, ...). Overall, we notice significant differences between the three families, which is illustrating the benefit of performing such a cluster analysis step.

To complement our ensemble analysis, we calculate and examine the corresponding sets of data residuals (for all residuals $\boldsymbol{\delta}_{acc}$ and each family of residuals $\boldsymbol{\delta}_{Fi}$) as outlined in Section 2.2.6. In the pixel-wise analysis of the residuals (Fig. 2.10), we observe that the $\mu_{1/2}(\boldsymbol{\delta}_{F1})$ and $\mu_{1/2}(\boldsymbol{\delta}_{F3})$ pseudo-sections show similar overall patterns compared to the $\mu_{1/2}(\boldsymbol{\delta}_{acc})$ pseudo-section. However, $\mu_{1/2}(\boldsymbol{\delta}_{F2})$ is different and the corresponding pseudo-section (Fig. 2.10e) shows reduced residual values for levels > 15 compared to Fig. 2.10a, c, and g. Although the $\mu_{1/2}(\boldsymbol{\delta})$ pseudo-sections are indicating high relative error values (0.04-0.05) for the first and deeper levels, these values are still in an acceptable range for an ERT survey. Additionally, we find that the IQR$(\boldsymbol{\delta})$ pseudo-sections (Fig. 2.10b, d, f, and h) present the same main patterns for all sets of residuals ($\boldsymbol{\delta}_{acc}$, $\boldsymbol{\delta}_{F1}$, $\boldsymbol{\delta}_{F2}$, $\boldsymbol{\delta}_{F3}$) where the highest variabilities are located in the uppermost and lowermost levels. Furthermore, we notice a diagonal pattern originating in the uppermost level at $x \approx 160$ m. These diagonals are related to the location of the lateral resistivity contrast discussed above. Complementary to the pixel-wise analysis, we globally assess the RMSLE, IQR, and q_{90} for $\boldsymbol{\delta}_{\boldsymbol{acc}}$ and $\boldsymbol{\delta}_{Fi}$ (Fig. 2.11). From these histograms, we learn that $\boldsymbol{\delta}_{F1}$ and $\boldsymbol{\delta}_{F3}$ are characterized by the highest values for all variables, while

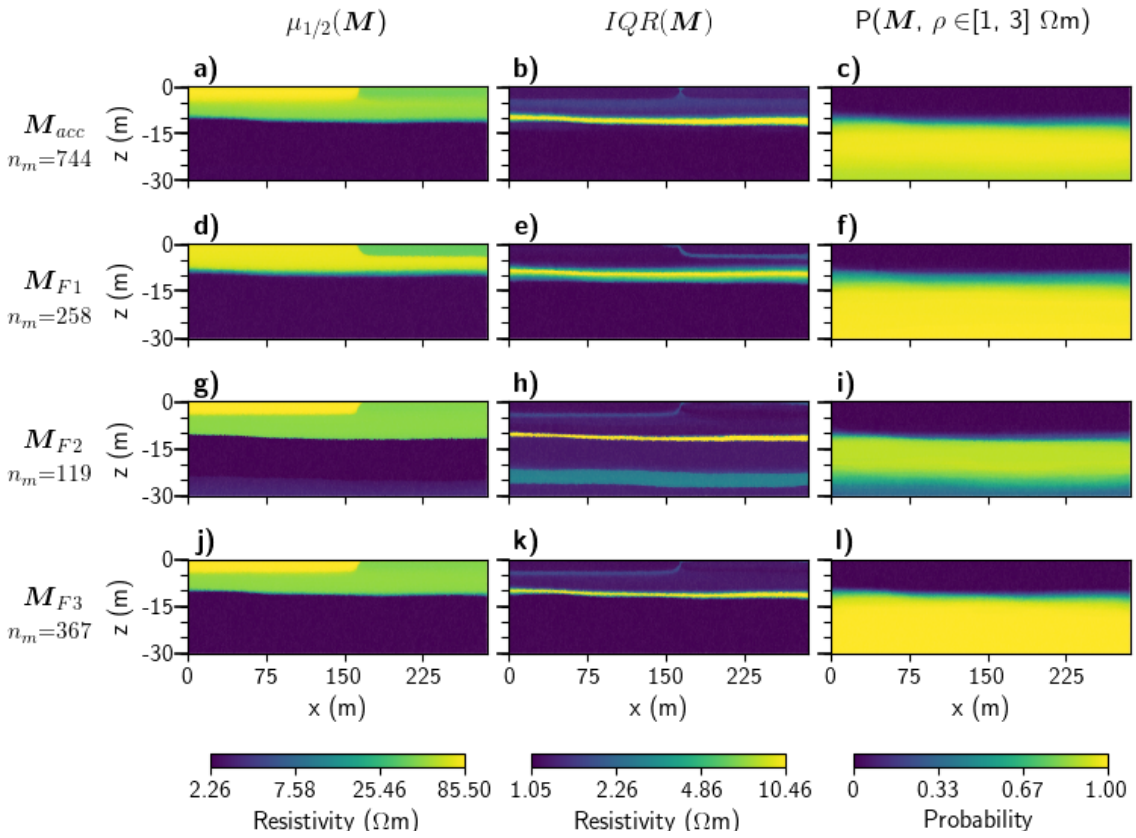

Fig. 2.9. Representation of the pixel-wise calculation of the $\mu_{1/2}(\boldsymbol{M})$, IQR($\boldsymbol{M}$), and $P(\rho \in$ [3, 15] Ωm) for our field example. (a-c) statistics for the accepted models $\boldsymbol{M}_{acc}$ and (d-l) for the clustered families $\boldsymbol{M}_{F1}$, $\boldsymbol{M}_{F2}$, and $\boldsymbol{M}_{F3}$. n_m represents the size of each ensemble of models.

the histograms of $\boldsymbol{\delta}_{F2}$ are shifted towards lower values compared to $\boldsymbol{\delta}_{F1}$ and $\boldsymbol{\delta}_{F3}$. From the pixel-wise and global analysis of the residuals, we notice a better performance of F2, where it is important to highlight that F2 is the one indicating a layer boundary at a depth of $\sim$ 23 m (see Fig. 2.9g). This indicates that the data points collected at the lowest levels are still sensitive to the small resistivity contrasts of the models collected in F2.

2.4 Discussion

Inversion of ERT data is a non-linear and non-unique problem. However, using global optimization algorithms such as PSO, we can obtain an ensemble of equivalent solutions. This study compiles a workflow (Fig. 2.1) that allows us to extract the main structures needed by the data and to assess the variability within the ensembles including the underlying residual distributions. To demonstrate our approach we used two 2D ERT data sets, which have been inverted using PSO and a layer-based model parameterization.

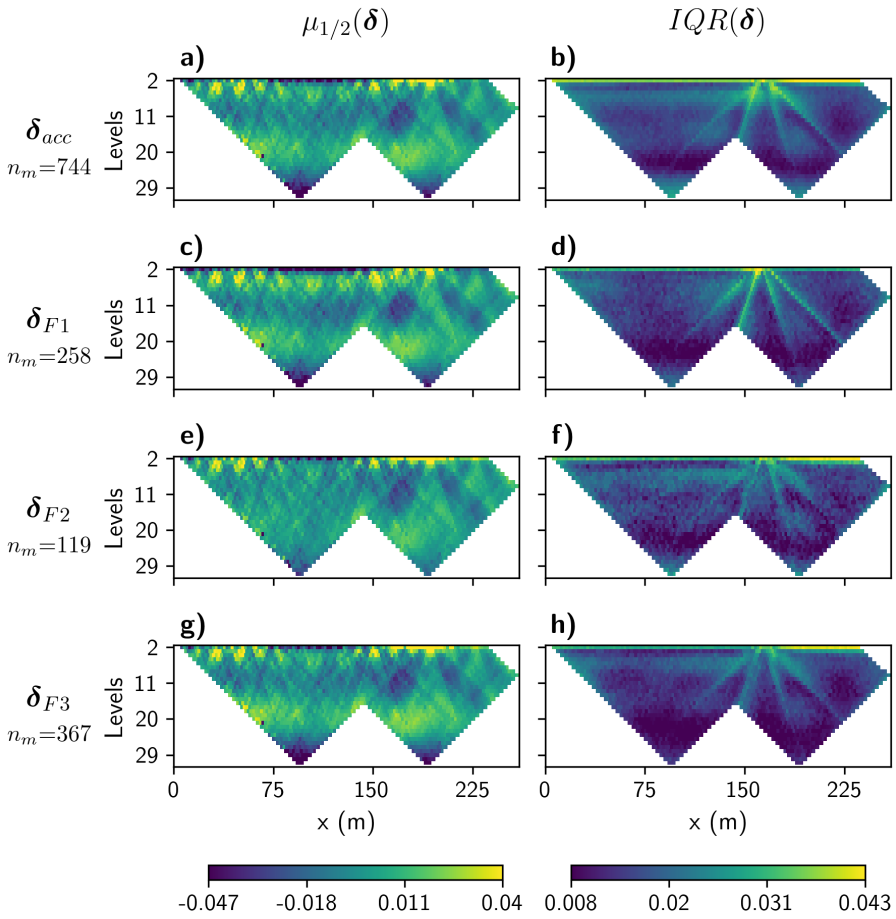

Fig. 2.10. Pseudo-section representation of the pixel-wise calculation of $\mu_{1/2}(\boldsymbol{\delta})$ and IQR($\boldsymbol{\delta}$) for our field example. (a-b) statistics for the accepted data residuals $\boldsymbol{\delta}_{acc}$ and (c-h) for the clustered families $\boldsymbol{\delta}_{F1}$, $\boldsymbol{\delta}_{F2}$, $\boldsymbol{\delta}_{F3}$. n_m represents the size of each ensemble of residual vectors.

Although we iteratively use a global-search approach to invert a 2D ERT data set, some optimization runs might not converge (e.g., Lomax and Snieder, 1995; Douma et al., 1996). Furthermore, defining a reliable stopping criterion is not straightforward, especially when there is no clear knowledge of the data noise level. When an approximation of the noise level is obtained by repeated measurements (e.g., Zhou and Dahlin, 2003), it is recommended to obtain models whose misfits values fall within a range contemplating smaller and larger misfit values and, thus, avoid the influence of data perturbation or modification of the inversion strategy (e.g., Vasco et al., 1993). We must consider that such an approach may result in considering models that are underfitting or over-fitting the data. This is why in the second step of our workflow (Fig. 2.1), we propose a model selection criteria that not only considers the models exceeding a certain threshold in the objective function (RMSLE($\boldsymbol{\delta}$) in this study) but also considers other statistical descriptors such as $q_{90}(\boldsymbol{\delta})$ as in Barboza et al. (2019) and IQR($\boldsymbol{\delta}$). In our examples, thresholds were initially defined in such a way that models located in the high-value tails of the RMSLE($\boldsymbol{\delta}$), IQR($\boldsymbol{\delta}$), and $q_{90}(\boldsymbol{\delta})$ histograms are discarded. However, just using simple thresholding may result in inaccuracies associated, for example,

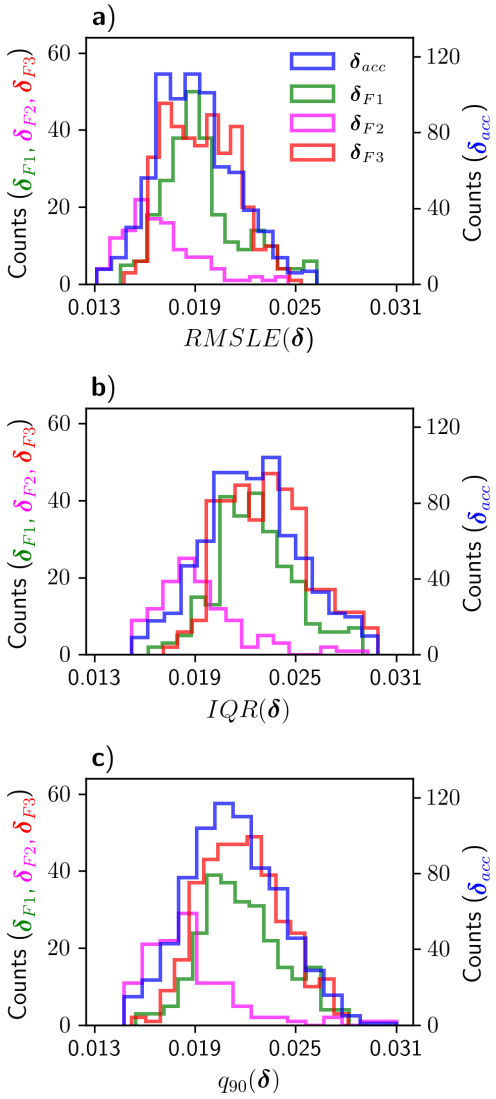

Fig. 2.11. (a-c) Histograms of the global statistical descriptors RMSLE($\boldsymbol{\delta}$), IQR($\boldsymbol{\delta}$), and $q_{90}(\boldsymbol{\delta})$ for the field example. Notice that the corresponding counts of $\boldsymbol{\delta}_{F1}$, $\boldsymbol{\delta}_{F2}$, and $\boldsymbol{\delta}_{F3}$ are represented by the left axis, and of $\boldsymbol{\delta}_{acc}$ by the right axis. The legend in (a) also applies for (b) and (c).

with the bin size of the histograms. We found that scatter plots help to further refine the threshold levels (see Fig. 2.3 and Fig. 2.8). Overall, the proposed way of filtering and formulating the model selection criteria allows for a detailed and robust selection of models from a generated ensemble.

To study model ensembles, some examples in the literature have successfully shown that central trends, dispersion measures, and probability maps are effective ways to summarize the information contained in an ensemble including the communication of uncertainties (e.g., Tronicke et al., 2012; Fernández-Martínez et al., 2012; De Pasquale et al., 2019). Such global ensemble statistics are useful if similar models compose the ensemble. This can be inspected, for example, by visually comparing the calculated median

model with individual models from the ensemble. If the ensemble is rather heterogeneous, the median model might not be representative for most models and, thus, cluster analysis can be considered as a useful tool to analyze the ensemble in more detail. In this study, we extend previous ideas by using a cluster strategy that not only considers the model values (e.g., Vasco et al., 1993, 1996; Ramirez et al., 2005; Fernández-Martínez et al., 2017) but also the corresponding data residuals. This strategy results in clusters of similar models and ensures that they fit the data in a similar fashion (as shown by the two examples in this study). Further extensions of our strategy could be, for example, to apply a weighted k-means algorithm, where the sensitivity matrix, the configuration factors, and/or measurement errors are used to weight the model and residual values, respectively. Although in this study we focus on the classical k-means algorithm, other algorithms such as spectral or agglomerative clustering might be considered to perform the classification.

Apart from analyzing sets of models, studying the corresponding sets of data residuals adds further valuable information to better understand the clustered ensemble. Typically, global evaluations of the residuals are used to get an overall view of each ensemble's performance. In this study, we additionally use a pixel-wise representation of the residuals. This visualization strategy might be used, for example, to explore the areas where the fit performs better or worse, find outliers, or determine numerical errors. We also highlight that when using a layer-based model parameterization the spatial error distribution may create some characteristic patches which can be explained by the limitation of a layer-based approach to fit small-scale heterogenities. Using both global and pixel-wise evaluations of the residuals provides a more robust criterion to accept/reject a specific set of models and to evaluate or modify the used inversion strategy (e.g., to adapt the parameterization strategy or the objective function).

Understanding uncertainties associated with the non-uniqueness of the inverse problem is crucial to create, for example, probabilistic structural and petrophysical translations. Nevertheless, this kind of analysis requires an ensemble composed of up to hundreds of independent solutions. Generating such ensembles through global optimization algorithms is computationally demanding. However, with recent computer developments, the calculation time has been considerably reduced. Furthermore, different methods help to mine the parameter solution space and to increase the number of model solutions (e.g., Sambridge, 1999; Tompkins et al., 2011; Fernández-Martínez et al., 2017).

2.5 Conclusions

This paper presents a workflow to assess ensembles of 2D ERT inversion results generated using global optimization strategies such as genetic algorithms, different simulate annealing varieties, PSO (as implemented in this study), and others. We found, in a first step, that using the global evaluation of RMSLE($\boldsymbol{\delta}$), IQR($\boldsymbol{\delta}$), and $q_{90}(\boldsymbol{\delta})$ is a robust criterion to remove models that might not have completely converged and, thus, improve the posterior statistical characterization of the ensemble. Furthermore, the cluster analysis using the *k*-means algorithm considering both model and residual values shows to be an efficient and robust approach to better explore and understand our ensembles and, thus, allows us to identify different equivalent families of models with their corresponding data residuals. To summarize the information in such sets of clustered models, the central trend for each family can be treated as different plausible subsurface scenarios whose uncertainties can be derived by dispersion measurement statistics and probability maps. Additionally, analyzing the corresponding residual distributions for each family provides valuable information to further understand and assess the validity of the clustering output. In conclusion, our workflow eases and refines the interpretation of model ensembles resulting from the global inversion of 2D ERT data and might be easily adapted to other kinds of geophysical data and inverse problems, respectively.

3

Exploring the capabilities of electrical resistivity tomography to study subsea permafrost

---

This chapter is accepted for publication and is under production:
Arboleda-Zapata, M., Angelopoulos, M., Overduin, P., Grosse, G., Jones, B., and Tronicke, J., (in press*). Exploring the capabilities of electrical resistivity tomography to study subsea permafrost, *The Cryosphere*, https://doi.org/10.5194/tc-2022-60.
*This accepted version may contain slight formatting changes after proofreading.

Abstract

Sea level rise and coastal erosion have inundated large areas of Arctic permafrost. Submergence by warm and saline waters increases the rate of inundated permafrost thaw compared to sub-aerial thawing on land. Studying the contact between the unfrozen and frozen sediments below the seabed, also known as the ice-bearing permafrost (IBPT), provides valuable information to understand the evolution of sub-aquatic permafrost, which is key to improving and understanding coastal erosion prediction models and potential greenhouse gas emissions. In this study, we use data from 2D electrical resistivity tomography (ERT) collected in the nearshore coastal zone of two Arctic regions that differ in their environmental conditions (e.g., seawater depth and resistivity) to image and study the subsea permafrost. The inversion of 2D ERT data sets is commonly performed using deterministic approaches that favor smoothed solutions, which are typically interpreted using a user-specified resistivity threshold to identify the IBPT position. In contrast, to target the IBPT position directly during inversion, we use a layer-based model parameterization and a global optimization approach to invert our ERT data. This approach results in ensembles of layered 2D model solutions, which we use to identify the IBPT and estimate the resistivity of the unfrozen and frozen sediments, including estimates of uncertainties. Additionally, we globally invert 1D synthetic resistivity data and perform sensitivity analyses to study, in a simpler way, the correlations and influences of our model parameters. The set of methods provided in this study may help to further exploit ERT data collected in such permafrost environments as well as for the design of future field experiments.

3.1 Introduction

In arctic coastal regions, contemporary subsea permafrost thawing starts following the inundation caused by sea level rise and coastal erosion. Seawater is typically warmer than mean annual air temperatures, and the presence of saltwater (mostly through diffusive processes) lowers the freezing point of the seabed (Harrison and Osterkamp, 1978; Are, 2003). Additionally, groundwater flow of freshwater from inland areas might play an important role in thawing permafrost (Frederick and Buffett, 2015; Pedrazas et al., 2020), comparable to warm discharge from large rivers (Shakhova et al., 2017). Subsea permafrost is estimated to contain a large quantity of organic carbon (Sayedi et al., 2020), which can decompose microbially to generate carbon dioxide and/or methane after the permafrost thaws. Furthermore, gas hydrates are present in subsea permafrost and may act as an additional source of methane if they dissociate (Ruppel and Kessler, 2017). Understanding the development of permafrost degradation rates helps to fine-tune predictive models of greenhouse gas emissions that may represent a positive feedback for climate warming (Schuur et al., 2015). Furthermore, the correlation between permafrost degradation and coastal erosion proposed by Are (2003) and Overduin et al. (2012, 2016) might be used to refine coastal dynamics models.

Subsea permafrost is a perennially cryotic (< 0 °C) layer or body of sediments underneath a marine water column (Angelopoulos et al., 2020a). These sediments can be frozen or unfrozen. A layer of unfrozen ground in a permafrost area is known as talik, and in particular, the perennially cryotic unfrozen sediments forming part of the permafrost are known as cryopegs (Permafrost Subcommittee, 1988). Cryopegs can be isolated pockets or layers and are commonly found along Arctic coasts in saline marine sediments that are exposed following a marine regression, for example, due to isostatic uplift (O'Neill et al., 2020). Offshore, cryotic unfrozen sediment in between the water column and frozen ground is still generally referred to as a talik (Osterkamp, 2001). The subsea permafrost that contains ice is known as ice-bearing permafrost, and when the soil particles are cemented together by ice, it is termed ice-bonded permafrost (Permafrost Subcommittee, 1988). Because traditional geophysical methods such as electrical resistivity tomography (ERT) and seismic techniques can only distinguish between sediments with no or low ice content from those with high ice content (note that direct sampling is required for a quantitative estimation of ice-content), we refer to them as unfrozen and frozen sediments in this study, and the interface that separates them is the ice-bearing permafrost (IBPT). Imaging and determining the position of the IBPT (e.g., using geophysical or borehole data) is important for a better process understanding of subsea permafrost evolution and to infer degradation rates. For example, dividing the depth to the IBPT by the time since inundation results in the mean annual degradation rate (e.g., Are, 2003; Overduin et al., 2012, 2016).

Among the most used geophysical imaging techniques to study the subsea permafrost are different electromagnetic and seismic methods as well as ERT (Scott et al., 1990; Kneisel

et al., 2008; Hubbard et al., 2013). Electromagnetic induction (EMI) methods are promising techniques to map both the top and bottom boundaries of the permafrost and might be used for a wide range of water depths (e.g., Sherman et al., 2017). EMI methods can properly work under low-resistive seawater layers, while the use of ground-penetrating radar (GPR) is limited to freshwater bottom-fast ice environments characterized by high electrical resistivity values as found in delta areas (e.g., Stevens et al., 2008). Seismic methods have been employed widely in deep-water environments (e.g., Rekant et al., 2015; Brothers et al., 2016) and, more recently, researchers have used recordings of ambient seismic noise in shallow waters to map the IBPT (e.g., Overduin et al., 2015a). The ERT method is a suitable tool to investigate the resistivity distribution of the unfrozen sediments (e.g., talik and cryopeg) and for studying and delineating the IBPT position (e.g., Sellmann et al., 1989; Overduin et al., 2012, 2016; Angelopoulos et al., 2019, 2020b; Angelopoulos, 2022; Pedrazas et al., 2020).

In marine ERT surveying, floating electrodes are typically used to inject a current and measure potential differences that are used to calculate apparent electrical resistivity data. In the summer season of the Arctic, the measured values are often influenced by the resistivity and thickness of the water layer and by the unfrozen and frozen sediments. The ERT method can detect the IBPT but does not necessarily distinguish non-cryotic from cryotic taliks above the IBPT. The resistivity of seawater depends mainly on the amount of dissolved salts and temperature. The dissolved salts are mostly affected by water inflows from rivers and the cycles of sea ice melting, freezing, and brine release. The resistivity of the seawater is commonly in the range of 0.1 Ωm to 40 Ωm (e.g., Sellmann et al., 1989; Lantuit et al., 2011). On the other hand, the resistivity of the underlying sediments is influenced by porosity, pore size, grain size, water and ice content, porewater salinity, and temperature (Kneisel et al., 2008; Wu et al., 2017). For example, the resistivity of unfrozen sediments typically ranges from 1 Ωm to 25 Ωm (e.g., Sellmann et al., 1989; Overduin et al., 2012; Angelopoulos et al., 2019), while the resistivities of frozen sediments might vary from 10 Ωm up to more than 1,000 Ωm (e.g., Overduin et al., 2012, 2016; Pedrazas et al., 2020; Rangel et al., 2021). The higher the ice content, the more resistive is the medium (Pearson et al., 1986; Fortier et al., 1994; Kang and Lee, 2015). In cases where the resistivity of the frozen sediments is several orders of magnitude higher than the resistivity of the overlying unfrozen sediments, the electrical current injected through the electrodes is expected to be channeled through the less resistive layers (e.g., Spitzer, 1998) resulting in a limited penetration of the current system into the frozen sediment layers.

When analyzing ERT data collected in subsea permafrost environments, defining an appropriate inversion and model parameterization strategy is critical for deriving reliable resistivity models and interpreting these models in terms of the IBPT position. For example, when a priori information suggests that the nature of the contact between the unfrozen and frozen sediments is gradual, a grid-based model parameterization and a local inversion algorithm favoring vertical and/or horizontal smoothness in the final models might be an appropriate choice (e.g., Loke and Barker, 1996; Günther et al., 2006). Here, the experience of the interpreter

might help to guess a specific resistivity threshold value to define the IBPT position (e.g., Overduin et al., 2016; Sherman et al., 2017; Angelopoulos et al., 2021). Additionally, one may also consider different gradient-based image processing approaches to extract interfaces from the inverted resistivity model (e.g., Hsu et al., 2010; Chambers et al., 2012). Finally, when we have ample evidence of a sharp contact between the unfrozen and frozen sediments (e.g., Overduin et al., 2015b; Angelopoulos et al., 2020a), a layer-based model parameterization combined with a local and/or global inversion algorithms might be more suitable (e.g., Auken and Christiansen, 2004; Akça and Basokur, 2010; De Pasquale et al., 2019; Arboleda-Zapata et al., 2022b).

In this study, we adapt the inversion and ensemble interpretation strategies as proposed by Arboleda-Zapata et al. (2022b) to study submarine permafrost environments of the Arctic in terms of the resistivity distribution of the unfrozen and frozen sediments and the position of the IBPT, including estimates of uncertainties. We analyze and compare ERT data collected at two field sites in the Arctic characterized by different environmental conditions regarding seawater depth and resistivity, coastal erosion rate, and the sediments porewater chemistry. Additionally, we generate and interpret ensembles of globally inverted 1D electrical data to get a deeper understanding of the inverse problem for typical resistivity distributions in these kinds of environments. Finally, we also implement local and global sensitivity analyses to recognize the most influential parameters during 2D and 1D inversions.

3.2 Study sites

Our field data were collected at two field sites; one offshore of the southern part of the Bykovsky Peninsula in the Siberian Laptev Sea (Fig. 3.1a), and the other one offshore of Drew Point in the Alaskan Beaufort Sea (Fig. 3.1d). To relate these data sets to the site-specific environmental settings, we summarize the main characteristics of each study area in a regional framework.

3.2.1 Regional setting of Bykovsky Peninsula

The Bykovsky Peninsula is located in northeastern Siberia in the vicinity of the Lena River Delta. The peninsula is mainly characterized by the presence of ice-rich sediments (volumetric ice content exceeding 80 %, also known as the Yedoma Ice Complex) that accumulated during the Late Pleistocene (Schirrmeister et al., 2002; Grosse et al., 2007). The Yedoma deposits extend to 15 m below sea level (Grigoriev, 2008). The sediments at or below sea level are composed of silt, sand, and gravel with variable grain size distributions (Grosse et al., 2007). During the early to middle Holocene, a general landscape transformation started resulting in a thermokarst-dominated relief characterized by thermo-erosional valleys and thermokarst lakes (Schirrmeister et al., 2002; Grosse et al., 2007). The mean coastal erosion rates at different locations of the peninsula typically range between 0.4 m yr^{-1} to 1.5 m yr^{-1} with maximum

values of up to 10 m yr^{-1} mainly caused by storms and thermomechanical erosion of ice-rich sediments (Lantuit et al., 2011). The seawater around the peninsula is strongly influenced by freshwater and sediments originating from the Lena River (Lantuit et al., 2011). Additionally, the resistivity of the seawater is influenced by seasonal sea ice freezing and melting as shown by Lantuit et al. (2011) who report resistivity values for the eastern shore of the Bykovsky Peninsula of less than 1 Ωm in winter and above 10 Ωm in summer. Similar water resistivity values are also reported by Overduin et al. (2016) for the seawater near Muostakh Island. The depth of the seawater for the southern part of the Bykovsky peninsula deepens 2 m within a distance of 100 m from the shoreline and increases to 5 m at about 2,000 m from the coast (Lantuit et al., 2011; Fuchs et al., 2022).

3.2.2 Regional setting of Drew Point

Drew Point is located on the coast of the Alaskan Beaufort Sea. The local geology is characterized by glaciomarine, fine-grained, ice-rich sediments deposited in the late Pleistocene (Black, 1964; Ping et al., 2011). The inland geomorphology is characterized by 3-5 m high coastal bluffs, thermokarst channels and lakes, and ice-wedge polygons on tundra plains with maximum elevations of $\sim$ 10 m (Barnhart et al., 2014; Jones et al., 2018). The average coastal erosion rate between 1979 and 2002 was around 9 m yr^{-1} (Jones et al., 2009) and increased for the period 2002 to 2016 up to approximately 20 m yr^{-1} (Jones et al., 2018). Lück (2020) reports brackish water resistivities observed during fieldwork in July 2018 of 0.4-0.5 Ωm, with weak stratification visible in the water column profiles. The depth of the seawater offshore of Drew Point deepens to 2 m within a distance of 500 m from the shoreline and increases to 3 m at distances of about 2,000 m from the coast (Jones et al., 2018).

3.3 Data acquisition

In marine ERT data acquisition, there is typically an excellent coupling between the floating electrodes and the seawater. This allows us to perform voltage measurements while the boat pulling the electrode streamer is in motion (preferably at constant speed) and, thus, to efficiently measure also profiles with a length in the order of km. The sources of errors during data acquisition are mainly related to misalignments of the electrode streamer (e.g., due to water currents), the precision of electrode positioning (which are given relative to boat position), vertical oscillation of electrodes (e.g., due to wavy conditions), and surface area limitation of injection voltage. Furthermore, due to the large variety of environmental settings, one must tailor the survey parameters to each field site, which includes varying the electrode spacing, the transmitter voltage, the measurement duration, the boat speed, the digital resolution of the potential measurements, and the sampling frequency.

In Table 3.1, we compare the acquisition parameters for our ERT data from Bykovsky and Drew Point, which were collected during two fieldwork campaigns in July 2017 and July 2018,

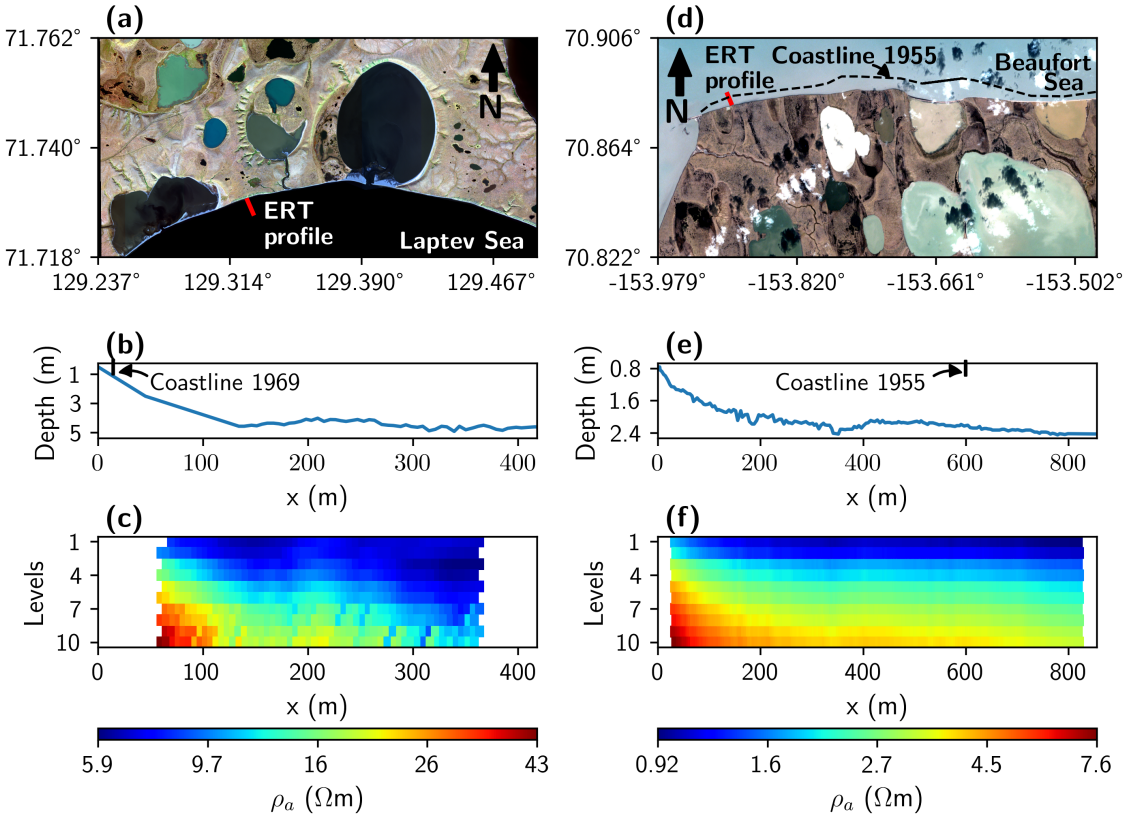

Fig. 3.1. Location and ERT data of our field studies. (a) Bykovsky field site located at the coast of the Laptev Sea in Northern Siberia (Sakha Republic, Russian Federation) and (d) Drew Point field site located at the coast of the Beaufort Sea in Northern Alaska (AK, United States of America), where the red lines indicate ERT profile locations and the black dashed line in panel (d) indicates the position of the 1955 coastline for Drew Point (Jones et al., 2008). (b) The recorded bathymetric profile along the ERT profile for Bykovsky and (e) for Drew Point indicating the 1969 (Schirrmeister et al., 2018) and 1955 coastline positions, respectively. The current coast position for both profiles is at $x \approx$ -10 m. (c) Pseudosection of the recorded raw ERT data for Bykovsky, and (f) for Drew Point. Satellite image Bykovsky: Worldview3 satellite product from September 2nd, 2016; copyright Digital Globe. Satellite image Drew Point: Planet satellite image from September 3rd, 2017.

respectively. The two ERT data sets were collected using an Iris^{TM} Syscal Pro Deep Marine system employing a streamer cable with 13 equally spaced floating electrodes. The resistivity measurements were acquired using a reciprocal Wenner-Schlumberger array configuration, where current was injected through the inner pair of electrodes and quasi-symmetric voltages were measured simultaneously with 10 channels using the outer pairs of electrodes (e.g., Overduin et al., 2012). The transmitter voltage was set at approximately 48 V at Bykovsky while, at Drew Point, it was reduced to 24 V to avoid exceeding the electrode surface area limits. Additionally, different electrode spacings were used. The Bykovsky data were recorded using a 10 m spacing between electrodes while, at Drew Point, 5 m spacing was chosen because the rapid coastal erosion rates suggested that the IBPT position at this field site should be shallower than at our Siberian field site for a given distance offshore. To collect the data along every profile, a cable was towed behind a small inflatable boat and voltages were measured as the boat moved at approximately constant speed of $\sim$ 1 m/s perpendicular to the shore.

The Bykovsky soundings were collected at spacings of $\sim$ 7.7 m along an 418 m long profile resulting in 540 measurements. At Drew Point, the soundings were collected at spacings of $\sim$ 4.7 m along a 854 m long profile resulting in 1,830 measurements. At both field sites, the electrode positions were estimated relative to the position of a GPS aboard the boat assuming a straight streamer cable. Complementary to the ERT measurements, we also recorded the water depth at each sounding location using a Garmin echo sounder attached to the boat (Fig. 3.1b, and e). Furthermore, we measured during each field campaign water resistivity and temperature at different depths close to our ERT profiles (the mean values are shown in the last two rows of Table 3.1) using a Sontek^{TM} CastAway device also known as CTD. In general, at our Drew Point field site, the seawater was shallower, less resistive, and slightly cooler than at our Bykovsky field site. Furthermore, the CTD measurements suggest low vertical and horizontal variations in the resistivity of the water layer at both field sites. For example, the largest variations are in the horizontal direction and are in the order of 1 Ωm and 0.04 Ωm for our Bykovsky and Drew Point data sets, respectively.

Table 3.1. Acquisition parameters for our ERT data sets and further site-specific information for our two field sites.

	Bykovsky, Siberia	Drew Point, Alaska
Number of electrodes	13	13
Electrode spacing (m)	10	5
Transmitter voltage (V)	48	24
Mean sounding separation (m)	7.7	4.7
Length of profile (m)	418	854
Number of data points	540	1830
Water resistivity (Ωm)	13.7	0.5
Water temperature ($^{\circ}$C)	7	5.5

The measured apparent resistivities ρ_a are presented as pseudosections in Fig. 3.1c and f. Here the x coordinates represent the center position of each quadripole, and the vertical axes represent the relative penetration also known as levels; i.e., level $=$ 1 is the shortest quadripole, while level $=$ 10 is the quadripole with maximum electrode spacing. The range of ρ_a for Bykovsky is 5.9 Ωm to 43 Ωm and for Drew Point 0.9 Ωm to 7.6 Ωm. The lower ρ_a values at Drew Point are mainly due to the lower resistivity of the seawater at the Alaskan coast, which is less influenced by freshwater discharge from large rivers than at our Bykovsky field site. Additionally, we notice that levels larger than seven in our Bykovsky data set are characterized by higher variations due to noise or 3D subsurface structures. In contrast, the Drew Point data not show obvious variations depending on the level number.

3.4 Methodology

In this study, we follow the workflow of Arboleda-Zapata et al. (2022b) who propose a layer-based model parameterization to globally invert 2D ERT data, which is used to generate an ensemble of representative model solutions. For completeness, we present a brief summary of this workflow in the following. For a more detailed analysis, we will also address complementary strategies such as 1D inversion tests as well as local and global sensitivity analyses.

3.4.1 2D layer-based model parameterization

One of the most important steps in any geophysical inversion workflow is defining a model parameterization that can properly represent the studied geological environment. Because a priori information suggests a layered subsurface (i.e., unfrozen sediments overlying frozen sediments) at both of our field sites, we choose a layer-based model parameterization considering an unstructured mesh with local refinements along the interfaces separating individual layers. Additionally, because resistivity variations within each layer are negligible compared to the variations between different layers, we assume homogeneous layers; i.e., each layer is characterized by one resistivity value. For more complex geological settings, one might allow for lateral and/or vertical variations within the layers (e.g., Auken and Christiansen, 2004; Akça and Basokur, 2010). To parameterize the interface geometry that defines the contact between the individual layers, we may use different strategies, for example, based on spline interpolation (e.g., Koren et al., 1991), Fourier coefficients (e.g., Roy et al., 2021), or sums of arctangent functions (Gebrande, 1976).

Allowing for abrupt changes along the interfaces is considered to be a critical point in subsea permafrost environments where high structural variability is often found. In such environments, we expect sharp boundaries and variations along the interfaces due to inundated thermokarst structures (Angelopoulos et al., 2021), pingo-like features, bottom-fast ice versus floating ice regime transitions in winter, or changes in the ratio of coastal erosion vs. degradation rate; i.e., changing from a period of fast thawing and low coastal erosion to a period of fast coastal erosion and slow thawing can result in a heterogeneous structure of the IBPT (e.g., Overduin et al., 2016). Because we expect some of these processes and structures at our field sites, we adopt a strategy based on the sums of arctangent functions because it allows for abrupt and smooth changes along the interfaces (e.g., Roy et al., 2005; Rumpf and Tronicke, 2015). Following Arboleda-Zapata et al. (2022b), the sums of arctangent functions for a single interface can be written as

$$z(x) = z_0 + \sum_{j=0}^{n_{nod}} \Delta z_j \left(0.5 + \frac{1}{\pi} tan^{-1}\left(x - \frac{x_j}{b_j}\right)\right), \tag{3.1}$$

where z is the depth, n_{nod} is the number of arctangent nodes, z_0 is the average depth of the interface, x_j is the horizontal location of an arctangent node, and Δz_j is the vertical throw

attained asymptotically over a horizontal distance of b_j. Such sets of coefficients are used to obtain $z(x)$ at horizontal distances x. Increasing the number of nodes allow to resolve more complex interfaces. During preliminary experiments and parameter testing, we noticed that using three to seven nodes allows to model rather complex interfaces. For both of our field studies, we fix the number of nodes to five, which results in 16 model parameters ($1 + 3n_{nod}$) per interface. Because we consider two interfaces, one for the seabed and the other for the IBPT separating three layers with homogeneous resistivities, our parameterization strategy results in total of 35 model parameters.

3.4.2 Inversion strategy

During inversion, we search for a combination of model parameters (i.e., those describing the geometry of interfaces using Eq. (Eq. (3.1)) and the resistivities of the homogeneous layers) that minimizes the root mean squared logarithmic error (RMSLE). To reduce the space of possible solutions, we consider some constraints in our layer-based parameterization approach. For both case studies, we constrain the seabed position (Fig. 3.1b and e) allowing vertical variations of up to $\pm$ 0.15 m which is the approximate error level of our echo sounder data for water depths $<$ 5 m. Considering our CTD measurements, we allow the resistivity of the water to vary between 11 Ωm to 15 Ωm for our Bykovsky data, and between 0.2 Ωm to 2 Ωm for our Drew Point data. Note that we consider additional freedom beyond the variabilities reported in Section 3.3 (1 Ωm for Bykovsky and 0.04 Ωm for Drew Point) to account for additional variations related to the different sensitivities and resolutions of our CTD and ERT data. Additionally, we set our search parameter range for the resistivity of the talik from 1 Ωm to 100 Ωm, and for the resistivity of the ice-bearing permafrost from 1 Ωm to 300,000 Ωm for both field studies.

Because we aim to find an inverse model independent of a reference or starting model, we use a global inversion strategy based on the particle swarm optimization (PSO) technique, which was originally introduced by Kennedy and Eberhart (1995). Over the last decade, the PSO algorithm has been widely used to invert different types of geophysical data sets because it has proven to be an effective tool for finding different local minima in objective functions with complicated topography (e.g., Tronicke et al., 2012; Fernández-Martínez et al., 2017).

In a first step, the PSO requires defining a set of particles where each particle represents a different model. The particles are initialized with random parameters bounded within realistic physical ranges. This defines our model space. The position of each particle is updated iteratively considering the best global position found so far by the entire swarm (i.e., the particle with the best fit performance in terms of the RMSLE), the best local position (i.e., the best fit performance in the history of each particle), and the inertia (i.e., the direction in which the particle is moving). These parameters are weighted and perturbed with random numbers drawn from a uniform distribution which helps avoid getting trapped in a local minimum. For every particle and every iteration, we calculate the forward response using the Python library

pyGIMLi (Rücker et al., 2017). Note that each particle contains model parameters that result in two different interface geometries, one representing the seabed and the other the IBPT. Thus, adding these interfaces to our finite-element mesh results in a different mesh geometry for each particle. To ensure good mesh quality, we constrain the minimum angle within each cell to 33.5° (Shewchuk, 1996). This parameterization strategy allows to calculate the forward response with high precision and with a reasonable amount of time (Arboleda-Zapata et al., 2022b). At the end, when the optimization reaches the maximum number of iterations or a minimum threshold in the objective function, we save the final best model. Using different seeds of the random number generator, we repeat this process until we obtain an ensemble $\boldsymbol{M}_{F0}$ consisting of several hundred independent models and an ensemble of corresponding residuals $\boldsymbol{\delta}_{F0}$. In this study, each residual vector is calculated as the difference between the observed and the corresponding modeled log-apparent resistivity values.

3.4.3 Ensemble interpretation

In a first step, to ease our ensemble analysis and interpretation in a pixel-wise fashion, all models in $\boldsymbol{M}_{F0}$ are interpolated using the nearest-neighbor algorithm on a densely discretized structured mesh (note that we use a unstructured mesh during inversion, Section 3.4.1). In a second step, we perform a cluster analysis using the *k*-means algorithm (MacQueen, 1967) and considering $\boldsymbol{M}_{F0}$ and $\boldsymbol{\delta}_{F0}$ as input to group similar solutions from our ensembles. To find an optimal number of clusters n_k, we use the criterion proposed by Caliński and Harabasz (1974) supported by a visual inspection of the clustering results. Finally, we characterize in a pixel-wise fashion each found cluster $\boldsymbol{M}_{Fi}$ and $\boldsymbol{\delta}_{Fi}$ (where $i = 0, 1, ..., n_k$; note $i = 0$ correspond to the whole ensemble and $i > 0$ to the clustered ensembles) by the median values $\mu_{1/2}(\boldsymbol{M}_{Fi})$ and $\mu_{1/2}(\boldsymbol{\delta}_{Fi})$ and the interquartile ranges IQR($\boldsymbol{M}_{Fi}$) and IQR($\boldsymbol{\delta}_{Fi}$). Additionally, we describe $\boldsymbol{\delta}_{Fi}$ in an overall fashion assessing the RMSLE($\boldsymbol{\delta}_{Fi}$), the IQR($\boldsymbol{\delta}_{Fi}$), and the quantile 90 % $q_{90}(\boldsymbol{\delta}_{Fi})$.

3.4.4 1D inversion

Often, we prefer 2D inversion algorithms in comparison to 1D strategies; especially for field data where the subsurface situation and its complexity are largely unknown. However, to investigate and understand, for example, the relationship between specific model parameters and the influence of a priori information and constraints, 1D approaches (also considering synthetic data examples) represent helpful interpretation tools (e.g., Sen and Stoffa, 1996; Malinverno, 2002).

In this study, we use 1D models consisting of five parameters, the depth of the seawater z_w, the depth of the contact between unfrozen and frozen sediments z_{pt} (i.e., IBPT), the water resistivity ρ_w, the resistivity of the unfrozen sediments ρ_{uf}, and the resistivity of the ice-bearing permafrost ρ_p. As for our 2D examples, we also consider PSO to invert our 1D synthetic data. Because for such 1D inversions the computational cost is significantly lower than for 2D problems, we can run several tests and create larger model ensembles. We use

such a 1D approach to tackle some specific questions regarding the considered application. For example, we investigate how constraining the depth of the water layer and its resistivity affects the final ensemble of 1D model solutions. Additionally, the limited number of parameters in our 1D model parameterization strategy allows us to study in a simpler way the posterior correlation matrix as proposed by Sen and Stoffa (2013). Although in this study we not consider cluster analysis to classify our 1D ensembles as implemented for our 2D analyses, this step may be adapted in future studies (e.g., investigating more complex model scenarios).

3.4.5 Sensitivity analysis

Sensitivity analysis is a powerful tool that can provide additional information to improve system or process understanding (Wainwright et al., 2014). In the context of subsea permafrost applications, several studies have shown the potential of the ERT method to image the IBPT position (e.g., Sellmann et al., 1989; Overduin et al., 2012). However, the sensitivity distribution of the ERT model parameters for such environments characterized by resistivity contrasts up to several orders of magnitude between unfrozen and frozen sediments is poorly understood. Adding sensitivity analysis to the interpretation workflow helps investigate the impact of our chosen model parameterization and the used constraints. Furthermore, such sensitivity studies might also help optimize ERT acquisition geometries and strategies before a field campaign.

In this study, we use 2D-local and 1D-global sensitivity analyses. To investigate which regions of the 2D discretized model have the greatest influence on our objective function, we consider the difference-based local sensitivity method of Günther et al. (2006), which is available within the pyGIMLi library (Rücker et al., 2017). For example, we assess the sensitivity of the shortest electrode configurations to understand if the corresponding measurements are influenced by both the water layer and the underlying unfrozen sediments. In turn, this helps to evaluate the reliability of imaging the uppermost water layer (e.g., for measurements where no CTD measurements are available). Furthermore, the longest electrode spreads (corresponding to the deepest levels in 2D pseudosections) and/or cumulative sensitivity distributions provide information on whether our ERT data are sensitive to the IBPT and/or the frozen sediments. For 1D model parameterizations and synthetic studies (considering z_w, z_{pt}, ρ_w, ρ_{uf}, and ρ_p as described in Section 3.4.4), we use the variance-based global sensitivity method of Sobol (Sobol, 2001; Saltelli et al., 2008) as implemented in the Python library SALib (Herman and Usher, 2017). Using this approach, we aim to understand how the total influence of the considered parameters might be affected by variations in ρ_p and z_{pt}.

3.5 Results

In the following, we present the 2D inversion results for the Bykovsky and Drew Point data sets in two separate subsections. Each subsection is complemented with 1D inversion results of synthetic data simulated considering the site-specific environmental and electrode settings

as well as with a 2D-local and a 1D-global sensitivity analysis.

3.5.1 Bykovsky

The geological and environmental settings of the Bykovsky area are described in Section 3.2.1 and a summary of the acquisition parameters and measured seawater properties is provided in Table 3.1. We invert the 540 apparent resistivity measurements recorded along a 418 m long profile (Fig. 3.1c) using a layer-based model parameterization as described in Section 3.4.1 and a PSO-based inversion strategy as outlined in Section 3.4.2. In the PSO, we use 60 particles and a maximum of 600 iterations as stopping criterion. To obtain a single inverted model (i.e., after one inversion run), we have to evaluate the forward response 36,000 times, which takes on average $\sim$ 40 h on a single core of a modern desktop computer. We repeat these inversion runs considering different initial seeds of the random number generator (note that this approach allows for a straightforward parallelization when multiple cores are available) until we obtain an ensemble $\boldsymbol{M}_{F0}$ consisting of 690 models.

Ensemble analysis

After the inversion, we interpolated all models to a refined structured mesh before performing any posterior statistical analyses (see Section 3.4.3). In Fig. 3.2a and b, we show the $\mu_{1/2}(\boldsymbol{M}_{F0})$ and IQR($\boldsymbol{M}_{F0}$) models calculated from the Bykovsky model ensemble. The $\mu_{1/2}(\boldsymbol{M}_{F0})$ model indicates that ρ_{uf} is $\sim$ 4 Ωm and ρ_p is $\sim$ 60,000 Ωm. However, when analyzing individual models, we note a bimodal distribution of ρ_p (some models with $\rho_p <$ 2,000 Ωm and others with $\rho_p >$ 100,000 Ωm) which is also illustrated by increased IQR($\boldsymbol{M}_{F0}$) values for the lowermost layer. These observations already indicate different groups of models with distinct resistivity characteristics.

In the next step, we performed cluster analysis (Section 3.4.3) and found that our ensemble $\boldsymbol{M}_{F0}$ can be divided into two model families $\boldsymbol{M}_{F1}$ and $\boldsymbol{M}_{F2}$. In Fig. 3.2b-c and e-f, we present the $\mu_{1/2}(\boldsymbol{M}_{Fi})$ and IQR($\boldsymbol{M}_{Fi}$) models (where i = 1, 2). Comparing these models illustrates that $\boldsymbol{M}_{F1}$ and $\boldsymbol{M}_{F2}$ show a similar IBPT shape dipping toward the open sea (i.e., depth of the IBPT increases with increasing profile distances). However, the IBPT position in $\boldsymbol{M}_{F1}$ is shallower than in $\boldsymbol{M}_{F2}$. We learn from this that for models favoring larger ρ_p values, the depth of the IBPT increases highlighting the trade-off between these two parameters that cause model variations along the IBPT. According to the depth of the IBPT and its gradients in the profile direction, we laterally subdivide the models into three main parts. The first part is found at $x <$ 130 m and is characterized by a gentle dipping slope with minor convexities and concavities. The second part is found at 130 m $< x <$ 280 m, where the IBPT is relatively flat with a minor change in depth at $x \sim$ 200 m. Finally, the abrupt change at x = 280 m marks the transition to the third part, where the IBPT reaches its deepest point and extends until the end of the profile at depths $>$ 20 m.

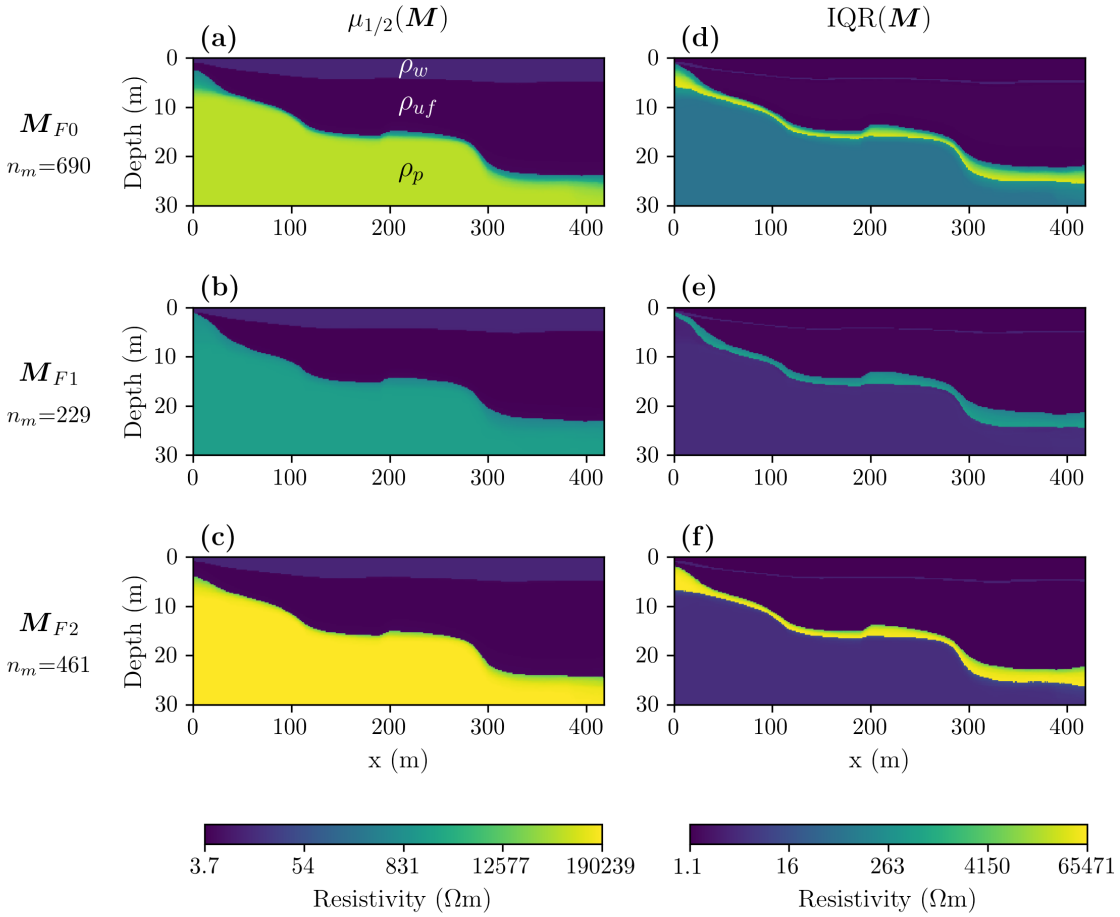

Fig. 3.2. Inversion results for the Bykovsky data set illustrated as summary statistics for all obtained models $\boldsymbol{M}_{F0}$ and for two model families $\boldsymbol{M}_{F1}$ and $\boldsymbol{M}_{F2}$ as found by cluster analysis. (a-c) Median and (d-f) interquartile range models. For each $\boldsymbol{M}_{Fi}$, n_m represents the number of models in the corresponding ensemble.

We assess the fit performance in a pixel-wise and in an overall fashion for the residuals associated with the ensemble containing all models $\boldsymbol{\delta}_{F0}$, as well as for the two clustered model families $\boldsymbol{\delta}_{F1}$ and $\boldsymbol{\delta}_{F2}$ (Fig. 3.3). Thus, we calculate $\mu_{1/2}(\boldsymbol{\delta}_{Fi})$ and IQR($\boldsymbol{\delta}_{Fi}$) (where i = 0, 1, 2) in a pixel-wise fashion and present them as pseudosections in Fig. 3.3a-f. When comparing these pseudosections to each other, we notice that the $\mu_{1/2}(\boldsymbol{\delta}_{Fi})$ and IQR($\boldsymbol{\delta}_{Fi}$) indicate similar fits of the data in terms of amplitudes and pseudosection patterns. The abrupt change from positive to negative residuals at $x \simeq 200$ m coincides with the highest point of the bathymetric profile for $x > 150$ m which also corresponds to a general change in the gradients of the bathymetric profile (Fig. 3.1b). Therefore, a 3D subsurface structure (which cannot be explained by our 2D inversion strategy) and related 3D effects are a reasonable explanation of the discussed features in the residuals. For example, because the landscape was partly covered by lakes (that acted as a source of heat) prior to seawater submergence, lateral temperature gradients and heterogeneous sediment properties could affect subsurface resistivity and its 3D variations. The overall statistics RMSLE($\boldsymbol{\delta}_{Fi}$), IQR($\boldsymbol{\delta}_{Fi}$), and $q_{90}(\boldsymbol{\delta}_{Fi})$ (where i = 0, 1, 2) are presented as histograms in Fig. 3.3g-i. The histograms are characterized by bimodal distributions, especially evident in all shown RMSLE($\boldsymbol{\delta}_{Fi}$) histograms. When comparing the

histograms of $\boldsymbol{\delta}_{F1}$ and $\boldsymbol{\delta}_{F2}$, we notice that they follow similar distributions (although in $\boldsymbol{\delta}_{F1}$ there are less models). From these analyses of the residuals, we are not able to prefer one of the model families and, thus, we perform some synthetic exercises to deepen our understanding of this inverse problem and the found model solutions.

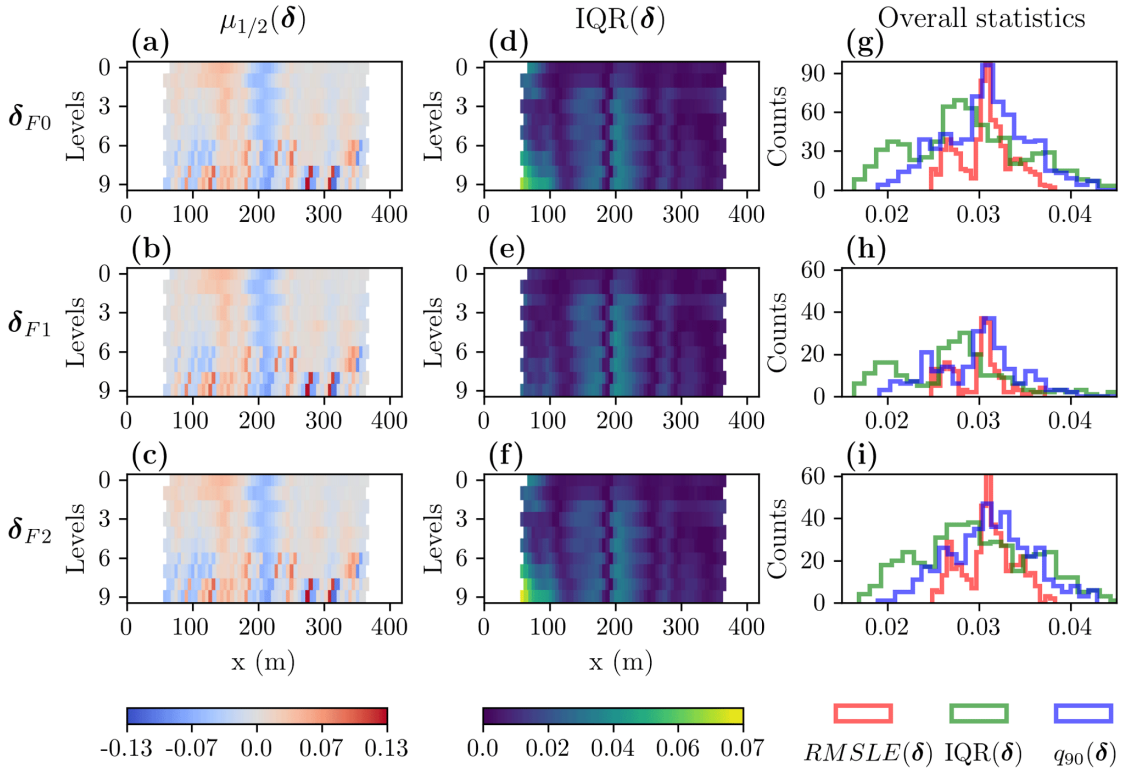

Fig. 3.3. Summary statistics of the residuals for the Bykovsky data set corresponding to all models $\boldsymbol{\delta}_{F0}$ and for the two clustered families $\boldsymbol{\delta}_{F1}$ and $\boldsymbol{\delta}_{F2}$. (a-c) Median and (d-f) interquartile range calculated in a pixel-wise fashion. (g-i) Histograms illustrating the overall distribution of different statistical measures including RMSLE($\boldsymbol{\delta}$), IQR($\boldsymbol{\delta}$), and $q_{90}(\boldsymbol{\delta})$.

1D inversion of synthetic data

To complement our understanding of the formulated inverse problem, we perform 1D inversions of a synthetic data set created considering a 1D subsurface model (see "Input model" in Table 3.2) as described in Section 3.4.4. The 1D subsurface model parameters were chosen by analyzing our 2D model solutions (e.g., Fig. 3.2b-c at $x \simeq 150$ m). We calculate the forward response of 10 quadripoles considering the same electrode configurations as used for recording the Bykovsky field data (Table 3.1). We invert the simulated apparent resistivity data using two scenarios for constraining z_w and ρ_w, while the constraints for all other parameters remain unchanged (see Table 3.2). The resulting inverted models are shown in Fig. 3.4a and c. For all models, we have achieved RMSLE < 0.028, which is equivalent to the noise level applied to the calculated synthetic data and comparable to the RMSLE achieved for the 2D inversion results of the Bykovsky field data. Comparing the results shown in Fig. 3.4a and c illustrates that constraining the water layer significantly decreases the non-uniqueness of the inverse problem. We also notice that the median model represents a good approximation to the input model

except for ρ_p which is overestimated as illustrated by the larger ρ_p of the quantile 25 % model compared to the input ρ_p. Additionally, from all models visualized in Fig. 3.4a and c, we calculate the corresponding posterior correlation matrices (Fig. 3.4b and d). For both cases, we see that [ρ_{uf}, z_{pt}] is the model parameter pair with the highest positive correlation while the rest of the model parameter pairs are characterized by negative correlations with different amplitudes (except for pairs with ρ_p which show correlations approaching zero).

Table 3.2. Parameters of the 1D synthetic model of Bykovsky and for two scenarios indicating the lower and upper bounds parameter constraints.

	Input model	Scenario 1	Scenario 2
Depth seawater z_w (m)	4.5	3, 6	4, 5
Depth IBPT z_{pt} (m)	15	6.5, 25	6.5, 25
Resistivity seawater ρ_w (Ωm)	13.7	1, 50	11, 15
Resistivity unfrozen sediments ρ_{uf} (Ωm)	4	1, 100	1, 100
Resistivity permafrost ρ_p (Ωm)	4,000	1, 200,000	1, 200,000

Sensitivity analysis

To understand the sensitivity distribution for our three-layer model (representing seawater and unfrozen sediments overlying frozen sediments), we calculate the cumulative sensitivity, and the sensitivity for the shortest and widest quadripoles considering two model scenarios (Fig. 3.5). In the first scenario, we consider the same input model as for the 1D inversion exercise (Table 3.2). In the second scenario, we set $z_{pt} = 25$ m while all other parameters remain unchanged. From the cumulative sensitivity plots (Fig. 3.5a and d), we learn that areas of sensitivities extend throughout the layer of unfrozen sediments for both scenarios. This suggests that we could interpret our inverted models even underneath the outer electrode positions; i.e., if the boat together with the electrode streamer is moving toward the right (i.e., increased x coordinates) to collect additional sounding curves, our interpretation of the inverted model should start at $x \sim$ -60 m. Note that a more conservative model interpretation might start at $x \sim$ -25 m, where we start having more significant cumulative sensitivities. When analyzing Fig. 3.5b and e, we see that the shortest quadripole is sensitive to both the water layer and the unfrozen sediments. For a wider electrode spacing and an IBPT located at a depth of 15 m (Fig. 3.5c), the sensitivities are focused around the inner electrodes but also with some minor contributions from the outer electrodes (note the reddish colors in the unfrozen sediments at $x <$ -60 m and at $x >$ 60 m), which may be critical when significant 2D or 3D resistivity variations are present. For a deeper IBPT (Fig. 3.5f), we notice that we are still sensitive at depths of $\sim$ 25 m; however, the lateral extensions of the sensitivity patterns within the unfrozen sediments appear to be reduced.

As noticed in our 2D sensitivity analysis, the high resistivity contrast between the unfrozen and frozen sediments seems to limit the penetration depth down to the IBPT. To complement

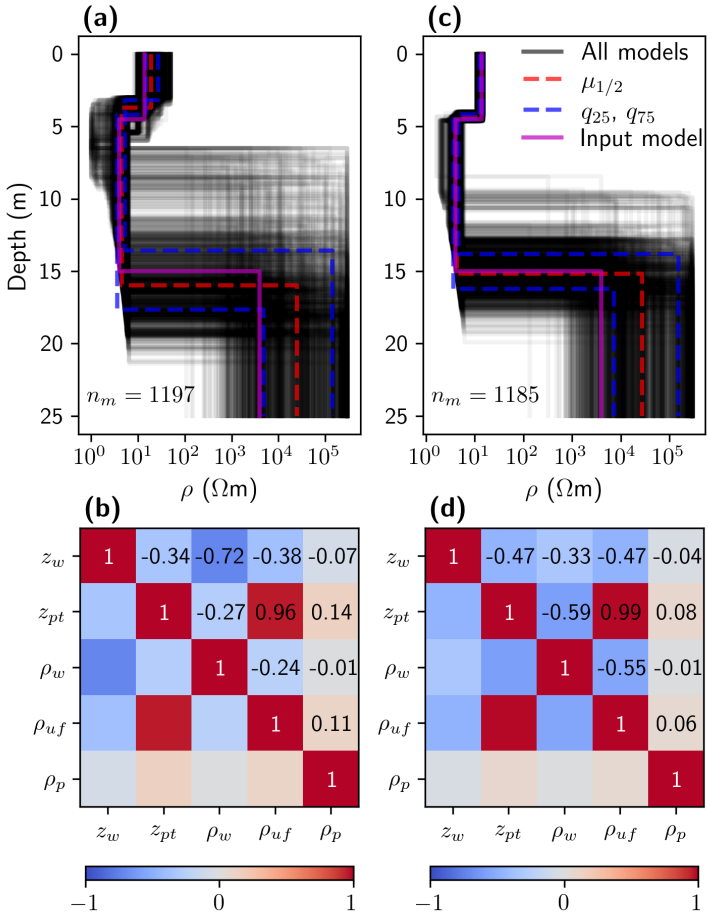

Fig. 3.4. 1D inversion results of synthetic data for 1D subsurface scenarios developed for the Bykovsky field site. (a) Ensemble with n_m model solutions and b) the corresponding symmetric correlation matrix for scenario 1 (water layer parameters with large freedom during inversion), and (c-d) the same for scenario 2 (with constrained z_w and ρ_w). Black lines in panels (a) and (c) are plotted with transparency and, therefore, the darker areas indicate higher density models. The numbers in panels (b) and (d) are the corresponding correlation values.

and better understand our results of 2D sensitivity analysis, we investigate the global sensitivities (Section 3.4.5) of different 1D model parameterizations. Specifically, we use models where $z_w = 4.5$ m, $\rho_w = 13.7$ Ωm, and $\rho_{uf} = 4$ Ωm are fixed, while ρ_p varies between 10 Ωm and 10,000 Ωm (eight values in total) and the IBPT is located at three different depths; i.e., $z_{pt} = 25$ m, $z_{pt} = 15$ m, and $z_{pt} = 5$ m (Fig. 3.6a-c). Note, defining eight different values for ρ_p and three for z_{pt} results in 24 different 1D models. For the calculation of the total sensitivity for each of our five parameters in these 24 models, we set the parameters ranges to $z_w = [4, 6]$ m, $z_{pt} = [6.5, 30]$ m, $\rho_w = [0.2, 20]$ Ωm, $\rho_{uf} = [1, 20]$ Ωm, and $\rho_p = [5, 20000]$ Ωm. For these specific models and parameter ranges, our results (Fig. 3.6) suggest ρ_w is the most influential parameter followed by ρ_{uf}, which shows approximately half of the influence compared to ρ_w. The influence of z_{pt} is slightly larger than z_w, although z_{pt} is set up with a wider range than z_w. Furthermore, although we allow ρ_p to vary over three orders of magnitude the result of this sensitivity analysis demonstrates that ρ_p is the parameter with the lowest influence, but it is not null as indicated by the results of our 2D sensitivity analyses (Fig. 3.5a and d). Such low sensitivity values help to explain the large variation of ρ_p

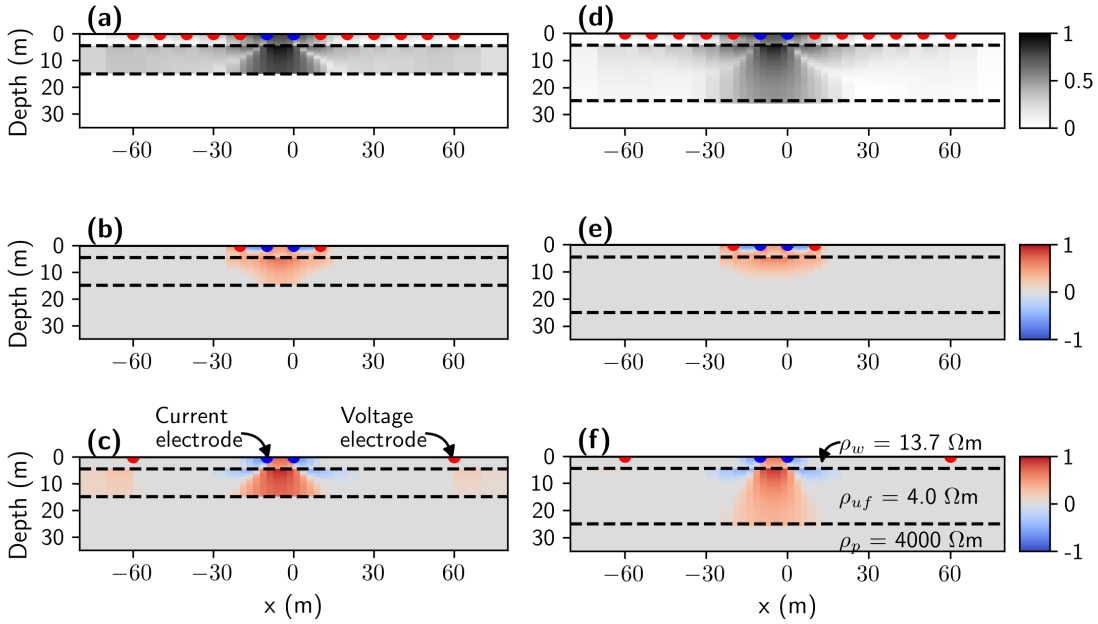

Fig. 3.5. 2D normalized sensitivities for two different model scenarios developed for the Bykovsky field site. Position of the the IBPT at a depth of (a-c) 15 m, and (d-f) 25 m. From top to bottom, we show the cumulative sensitivity and the sensitivity for the shortest and widest quadripole, respectively.

in our 1D and 2D ensembles. Interestingly, we also notice in Fig. 3.6a-c that in general when increasing ρ_p (for $\rho_p < 100$ Ωm) the total sensitivity index of the other parameters tend to decrease.

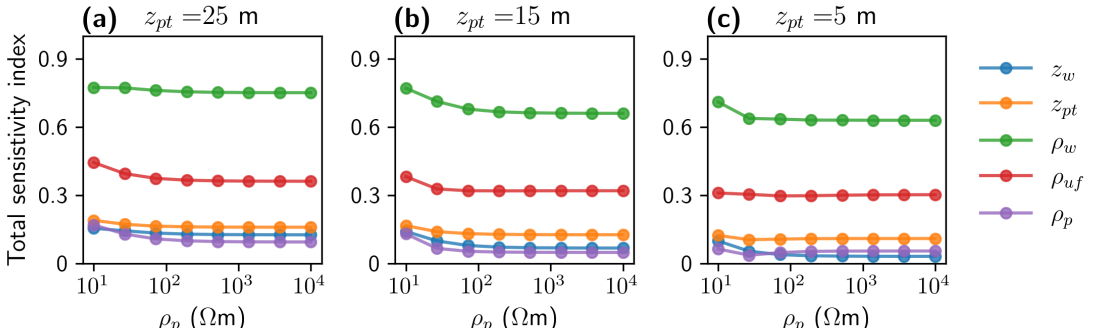

Fig. 3.6. Global sensitivity results for the Bykovsky field site considering different 1D model scenarios with an IBPT at a depth of (a) 25 m, (b) 15 m, and (c) 5 m.

3.5.2 Drew Point

The geological and environmental settings of the Drew Point area are described in Section 3.2.2 and a summary of the acquisition parameters and measured seawater properties is provided in Table 3.1. We invert the 1830 apparent resistivity measurements recorded along an 854 m long profile (Fig. 3.1f) considering a layer-based model parameterization as described in Section 3.4.1 and a PSO-based inversion strategy as outlined in Section 3.4.2. In the PSO, because we notice that the inversion of the Drew Point data set converges much faster than

in our Bykovsky example, we decide to lower the number of particles to 30 and the number of iterations to 400, thus, allowing us to save some computational cost. Considering these settings, to obtain a single inverted model, we have to evaluate the forward response 12,000 times, which takes on average 57 h on a single core of a modern desktop computer. We repeat these inversion runs considering different initial seeds of the random number generator (using different processors in parallel) until we obtain an ensemble $\boldsymbol{M}_{F0}$ consisting of 416 models.

Ensemble analysis

After the inversion, we interpolate all models to a refined structured mesh before performing any posterior statistical analyses (Section 3.4.3). In Fig. 3.7a and b, we present the $\mu_{1/2}(\boldsymbol{M}_{F0})$ and IQR($\boldsymbol{M}_{F0}$) models calculated from the Drew Point model ensemble. The irregular variations in the IQR($\boldsymbol{M}_{F0}$) model and the bimodal distribution of ρ_p (some models with $\rho_p <$ 500 Ωm and others with $\rho_p >$ 100,000 Ωm) already indicate different groups of models with distinct resistivity characteristics and IBPT positions.

In the next step, we performed cluster analysis (Section 3.4.3) and found that our ensemble $\boldsymbol{M}_{F0}$ can be divided into three model families ($\boldsymbol{M}_{F1}$, $\boldsymbol{M}_{F2}$, and $\boldsymbol{M}_{F3}$). In Fig. 3.7b-d and f-h, we present the $\mu_{1/2}(\boldsymbol{M}_{Fi})$ and IQR($\boldsymbol{M}_{Fi}$) models (where i = 1, 2, 3). Comparing these models illustrates that $\boldsymbol{M}_{F1}$ and $\boldsymbol{M}_{F2}$ present a similar IBPT shape dipping toward the open sea. However, for $\boldsymbol{M}_{F3}$ the IBPT position is dipping toward the coast which is not in agreement with our background knowledge of this field site. When comparing the $\boldsymbol{M}_{F1}$ and $\boldsymbol{M}_{F2}$ models in more detail, we note that the IBPT position in $\boldsymbol{M}_{F1}$ is shallower than in $\boldsymbol{M}_{F2}$. Comparable to the Bykovsky example, models favoring high ρ_p values tend to show increased depths of the IBPT resulting in thicker unfrozen sediments also near the coast. According to the depth of the IBPT and its gradients in the profile direction for $\boldsymbol{M}_{F1}$ and $\boldsymbol{M}_{F2}$, we laterally subdivide the model into four main parts. The first part is found at $x <$ 100 m and it is characterized by an intermediate convex slope. The second part is found at 100 m $< x <$ 500 m and the IBPT shows a gentle convex slope whereas in the third part (at 500 m $< x <$ 700 m) the IBPT is almost flat. Finally, the fourth part is found at $x >$ 750 m, where the IBPT may be located at depths $\geq$ 20 m.

We assess the fit performance for the residuals associated with the ensemble containing all models $\boldsymbol{\delta}_{F0}$, as well as for the three clustered model families $\boldsymbol{\delta}_{F1}$, $\boldsymbol{\delta}_{F2}$, and $\boldsymbol{\delta}_{F3}$ (Fig. 3.8). We calculate $\mu_{1/2}(\boldsymbol{\delta}_{Fi})$ and IQR($\boldsymbol{\delta}_{Fi}$) (where i = 0,1,2,3) in a pixel-wise fashion and present them as pseudosections in Fig. 3.8a-h. When comparing these pseudosections to each other, we notice that $\mu_{1/2}(\boldsymbol{\delta}_{Fi})$ indicate similar fits of the data in terms of amplitudes and pseudosection patterns (although with slightly higher values for $\boldsymbol{\delta}_{F3}$). When comparing the IQR($\boldsymbol{\delta}_{Fi}$) plots, we note that IQR($\boldsymbol{\delta}_{F0}$) is characterized by several patches which are less prominent in the clustered residuals Fig. 3.8f-h. This indicates that our clustering results are properly grouping models with similar residuals. Furthermore, we associate the vertical feature at x = 400 m in Fig. 3.8e-h to the variation in our models to locate the left edge of a bulge structure of the

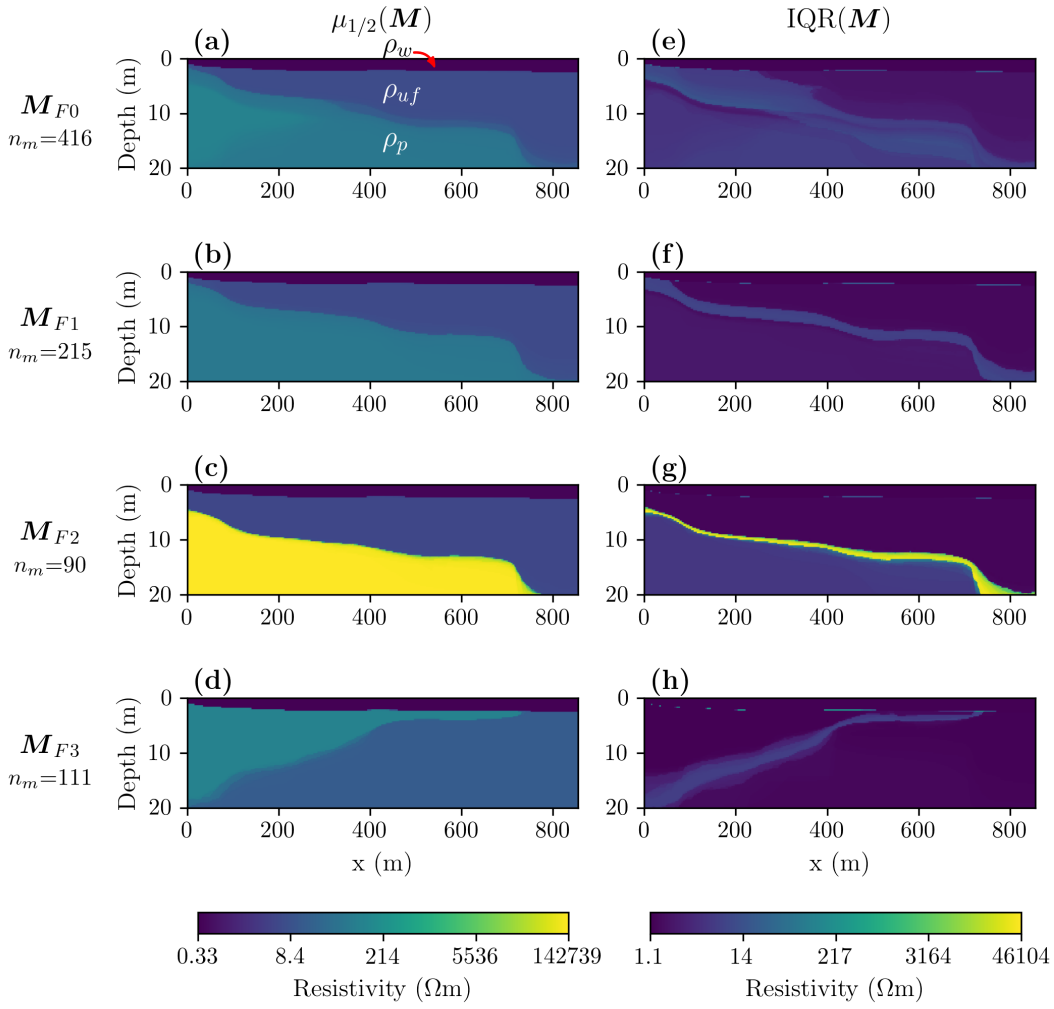

Fig. 3.7. Inversion results for the Drew Point data set illustrated as summary statistics for all obtained models $\boldsymbol{M}_{F0}$ and for three model families $\boldsymbol{M}_{F1}$, $\boldsymbol{M}_{F2}$, and $\boldsymbol{M}_{F3}$ as found by cluster analysis. (a-d) Median and (e-h) interquartile range models. For each $\boldsymbol{M}_{Fi}$, n_m represents the number of models in the corresponding ensemble.

seabed (see Fig. 3.1e). This illustrates the applicability of exploring such residual statistics to identify possible drawbacks in our inversion results and, thus, allow us to re-evaluate our parameterization strategy. For example, we might consider to improve the inversion results by adding a node to our sums of arctangent functions around $x = 400$ m. The overall statistics RMSLE($\boldsymbol{\delta}_{Fi}$), IQR($\boldsymbol{\delta}_{Fi}$), and $q_{90}(\boldsymbol{\delta}_{Fi})$ (where $i = 0, 1, 2, 3$) are presented as histograms in Fig. 3.8i-l. The histograms in Fig. 3.8i are characterized by bimodal distributions. Such bimodal distributions are less pronounced for the clustered families (Fig. 3.8j-l), however, small tails to the right are also evident for $\boldsymbol{\delta}_{F1}$ and $\boldsymbol{\delta}_{F2}$. One may tend to reject the models falling in these tails, especially, when using the mean to estimate the central trend. However, because we consider robust statistical measures (e.g., median and IQR), we do not expect a significant impact from these models on our results and conclusions.

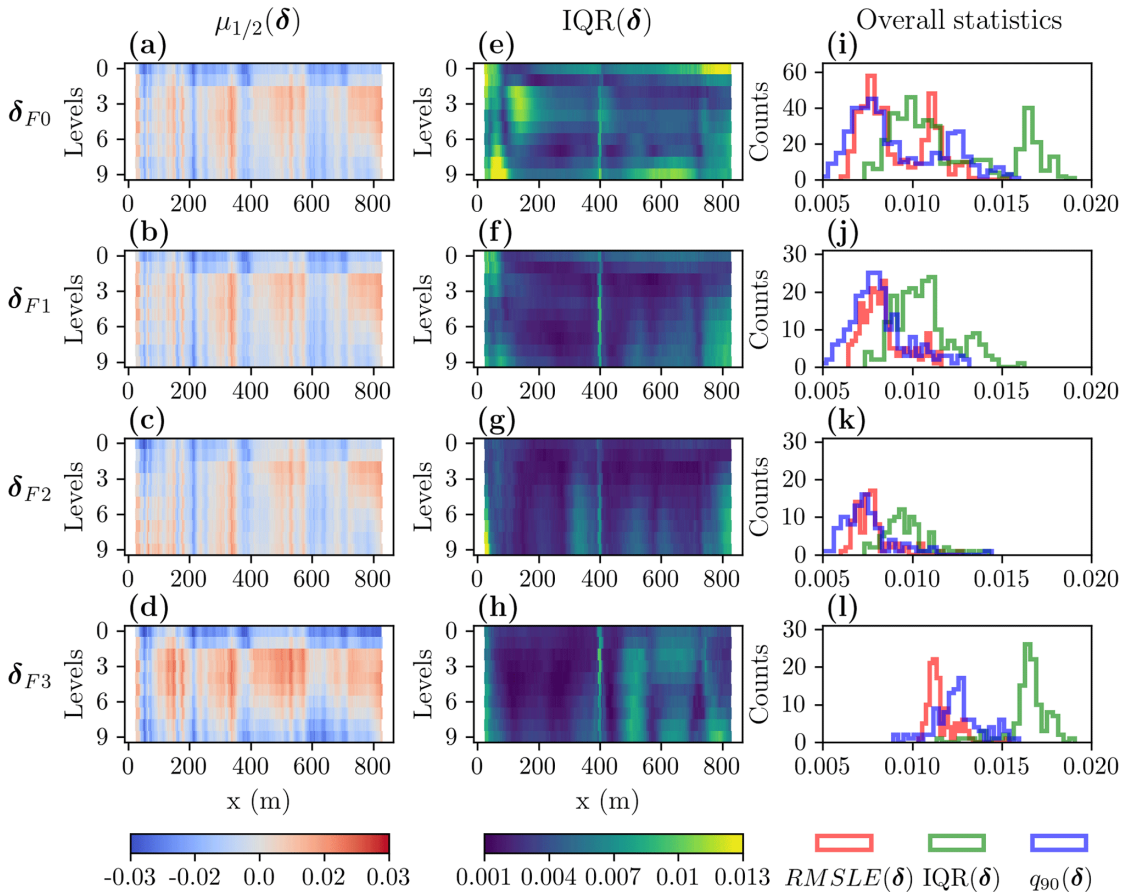

Fig. 3.8. Summary statistics of the residuals for the Drew Point data set corresponding to all models $\boldsymbol{\delta}_{F0}$ and for the three clustered families $\boldsymbol{\delta}_{F1}$, $\boldsymbol{\delta}_{F2}$, and $\boldsymbol{\delta}_{F3}$. (a-d) Median and (e-h) interquartile range calculated in a pixel-wise fashion. (i-l) Histograms illustrating the overall distributions of different statistical measures including RMSLE($\boldsymbol{\delta}$), IQR($\boldsymbol{\delta}$), and $q_{90}(\boldsymbol{\delta})$.

1D inversion of synthetic data

Following Section 3.4.4 and Section 3.5.1, we perform 1D inversions of a synthetic data set created considering a 1D subsurface model (see "Input model" in Table 3.3). The 1D model parameters were chosen by analyzing our 2D model solutions (e.g., Fig. 3.7b-c at $x \approx 600$ m). Note ρ_p is the same as in the 1D synthetic example from Section 3.5.1 which allows us to better compare the results of our 1D synthetic exercises. We calculate the forward response of 10 quadripoles considering the same electrode configurations as used for recording the Drew Point field data (Table 3.1). We invert the simulated apparent resistivity data considering two scenarios for constraining z_w, ρ_w, and ρ_{uf}, while the constraints for z_{pt} and ρ_p remain unchanged (see Table 3.3). The resulting inverted models are shown in Fig. 3.9a and c. For all models, we have achieved RMSLE < 0.007, which is equivalent to the noise level applied to the calculated synthetic data and comparable to the RMSLE achieved for the 2D inversion results of the Drew Point field data. Comparing the results shown in Fig. 3.9a and c illustrates that the applied constraints improve the median model. However, we also observe an increase in the variability of the models around z_{pt} in Fig. 3.9c. Additionally, from all the models visualized in Fig. 3.9a and c, we calculate the corresponding posterior correlation matrix (Fig. 3.9b

and d). For both cases, we see that the largest negative correlations are found for the model parameter pairs [ρ_{uf}, ρ_w] and [ρ_w, z_{pt}] while the most significant positive correlation is found for [ρ_{uf}, z_{pt}]. Note that the absolute correlations of these model parameter pairs are larger in Fig. 3.9d compared to Fig. 3.9c. Finally, we want to point out that the signs for the most significant parameter correlations are the same as the ones found for Bykovsky in Fig. 3.4d.

Table 3.3. Parameters of the 1D synthetic model of Drew Point and for two scenarios indicating the lower and upper bounds parameter constraints.

	Input model	Scenario 1	Scenario 2
Depth seawater z_w (m)	2	1.5, 2.5	1.9, 2.1
Depth IBPT z_{pt} (m)	12	3.5, 20	3.5, 20
Resistivity seawater ρ_w (Ωm)	0.4	0.2, 2	0.2, 0.6
Resistivity unfrozen sediments ρ_{uf} (Ωm)	5	0.2, 100	0.2, 20
Resistivity permafrost ρ_p (Ωm)	4,000	1, 200,000	1, 200,000

Sensitivity analysis

For the sensitivity analysis, we consider the two model scenarios indicated in Fig. 3.10. In the first scenario, we consider the same input model as for the 1D inversion exercise (Table 3.3). In the second scenario, we set $z_{pt} = 16$ m while all other parameters remain unchanged. From analyzing the cumulative sensitivity plots (Fig. 3.10a and d), we infer that an interpretation of our inversion results should focus on the area around the inner electrodes; i.e., if the boat is moving toward the right to collect additional sounding curves, our interpretation of the inverted model should start at $x \sim$ -10 m. When analyzing Fig. 3.10b and e, we see that we are most sensitive to the water layer. Interestingly, when comparing Fig. 3.10c and f in detail, we realize that the sensitivity distribution in Fig. 3.10c reaches the IBPT interface while the sensitivity distribution in Fig. 3.10f is almost null for depths $>$ 12 m.

We perform the global sensitivity analyses (Section 3.4.5) considering 1D models described by five model parameters as used for the above presented 1D inversions. We consider models where $z_w = 2$ m, $\rho_w = 0.4$ Ωm, and $\rho_{uf} = 5$ Ωm are fixed, while ρ_p varies between 10 Ωm and 10,000 Ωm (eight values in total), and the IBPT is located at three different depths; i.e., $z_{pt} = 16$ m, $z_{pt} = 10$ m, and $z_{pt} = 4$ m (Fig. 3.11a-c). For the calculation of the total sensitivity for each of our five parameters in the resulting 24 models, we set the parameter ranges to z_w = [0.5, 3] m, z_{pt} = [3.5, 20] m, ρ_w = [0.2, 20] Ωm, ρ_{uf} = [1, 20] Ωm, ρ_p = [5, 20,000] Ωm. For these specific models and parameters ranges, our results (Fig. 3.11) suggest that ρ_w and ρ_{uf} are the most influential parameters and the other three parameters (z_{pt}, z_w and ρ_p) are characterized in all cases by rather low total sensitivities. Furthermore, we also notice in Fig. 3.11a-c that ρ_w is the parameter showing the most significant changes when varying ρ_p and z_{pt}.

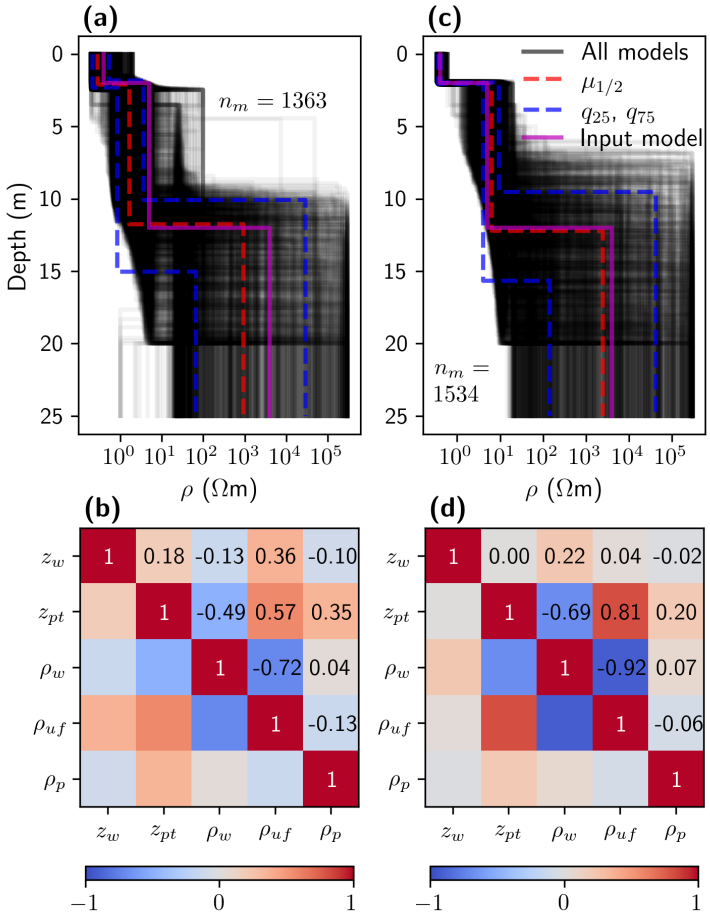

Fig. 3.9. 1D inversion results of synthetic data for 1D subsurface scenarios developed for the Drew Point field site. (a) Ensemble with n_m model solutions and (b) the corresponding symmetric correlation matrix for scenario 1 (water layer parameters with large freedom during inversion), and (c-d) the same for scenario 2 (with constrained z_w, ρ_w, and ρ_{uf}). Black lines in panels (a) and (c) are plotted with transparency and, therefore, the darker areas indicate higher density models. The numbers in panels (b) and (d) are the corresponding correlation values.

3.6 Discussion

Knowledge of how fast permafrost thaws would improve predictive models of greenhouse gas release and coastal erosion, as well as coastal infrastructure design. The ERT method has been successfully used to image the unfrozen sediments overlying the permafrost layer in subsea permafrost environments, especially using smooth inversion approaches (e.g., Overduin et al., 2012; Pedrazas et al., 2020). In typical subsea permafrost environments, there might be a gradual transition zone consisting of a mixture of water and ice between fully unfrozen and frozen ice-bonded sediments. However, during ERT inversion, the nature of this transition can be either enlarged when using smooth inversion approaches, or reduced to a single interface when using layer-based strategies. Whether we have a smooth or sharp transition between unfrozen and frozen sediments, there must be a threshold in the ice content that creates sufficient contrast in resistivity also influencing the penetration of the injected current and, thus, our apparent resistivity measurements (e.g., Kang and Lee, 2015). Because we wanted

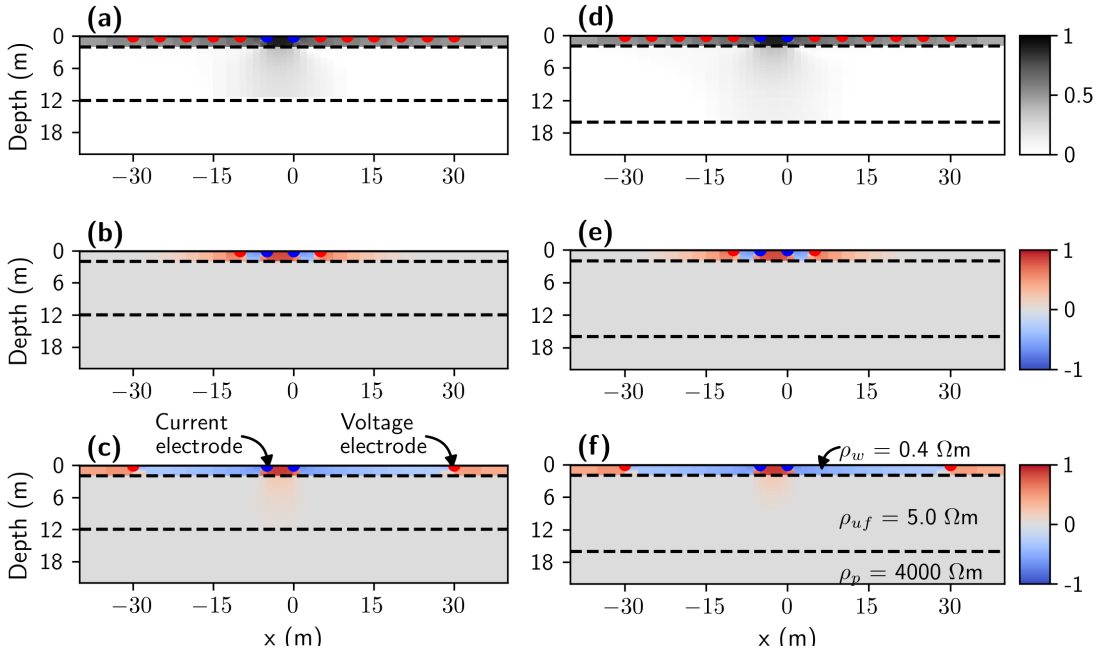

Fig. 3.10. 2D normalized sensitivities for two different model scenarios developed for the Drew Point field site. Position of the the IBPT at a depth of (a-c) 12 m, and (d-f) 16 m. From top to bottom, we show the cumulative sensitivity and the sensitivity for the shortest and widest quadripole, respectively.

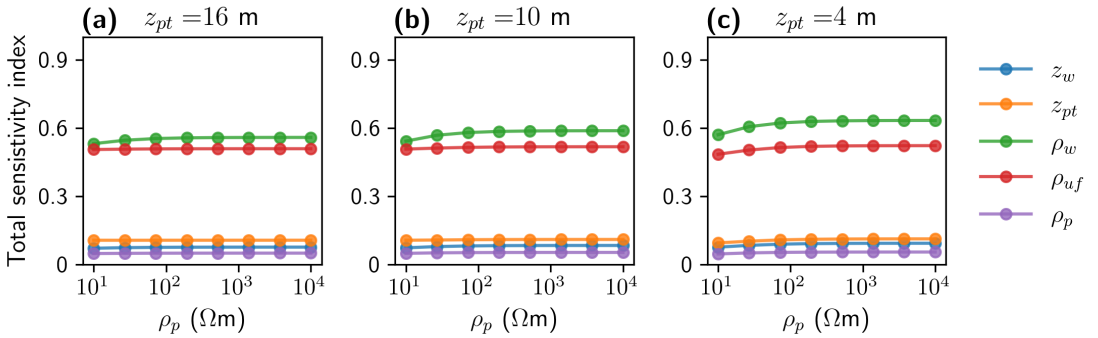

Fig. 3.11. Global sensitivity results for the Drew Point field site considering different 1D model scenarios with an IBPT at a depth of (a) 16 m, (b) 10 m, and (c) 4 m.

to target the interface defined by such a resistivity contrast (interpreted here as the IBPT), we considered a layer-based model parameterization to invert our ERT data. Additionally, we obtained estimates of uncertainties using an ensemble approach. For the sake of completeness, we provide the smooth inversion models for both of our field studies in Appendix Section 3.8.

3.6.1 Insights from our parameterization and inversion strategies

We used a 2D layer-based model parameterization to globally invert marine ERT data and obtain different ensembles (e.g., after cluster analysis) of model solutions. We demonstrated with the two case studies that such ensembles allow us to reliably image the IBPT position with its associated uncertainties. The main advantage of using a layer-based model parameterization strategy is that we do not assume an arbitrary resistivity threshold or gradient to interpret

the IBPT position, as we would need to do for our smooth inversion results (see Fig. 3.12a-b). This may be advantageous to compare ERT profiles collected at the same position in different years to track changes along the IBPT or in environments where the freezing point of the sediment porewater changes spatially. For example, offshore surveys that encounter submerged hypersaline lagoon deposits may show relatively low resistivity values for partially frozen sediments compared to colder ice-bonded permafrost with fresh porewater (Angelopoulos et al., 2021). Indeed, this interface may be related to a threshold in ice content. However, associating the IBPT with a certain ice content requires calibration by using borehole data or by additional geophysical information; e.g., by using the joint inversion approach of ERT and seismic refraction data of Wagner et al. (2019). Such thresholds may vary from site to site depending on properties of the sediments including temperature, grain size distribution, and the salinity of the porewater. Furthermore, we consider it convenient to use the sum of arctangent functions to parameterize the IBPT because there may be cases where the IBPT position varies steeply (as the ones we identified at the end of the median models in Figs. Fig. 3.2a-c and Fig. 3.7a-c) associated, for example, with submerged thermokarst structures or changes in the ratio of coastal erosion vs. degradation rate.

To find reliable and stable 2D model solutions, we performed experiments in which we ran the PSO several times to find the appropriate parameter settings for our layer-based ERT inversion. In a first stage, when performing our 2D inversions without considering any constraints, we found model solutions that were unrealistic according to our prior knowledge of our field sites. Therefore, we constrained our inversions considering our bathymetric and CTD measurements (see Section 3.4.2). Although the 2D inverted models without considering constraints are not shown in this study, we demonstrated with our 1D inversions how such constraints significantly improved the inversion results while reducing the number of possible solutions. Another exercise in the experimental phase consisted in using more than three layers in our parameterization strategy. However, we did not observe any significant improvement in the final median models when increasing the number of layers and, thus, restricted our inversion and analyses to three-layer scenarios.

One disadvantage of using a layer-based model parameterization relying on homogeneous layers is that it is not possible to resolve small-scale resistivity variations (e.g., horizontal heterogeneities at a spatial scale of meters). However, our workflow allowed us to inspect and evaluate model performance including the appropriateness of the model parameterization. For example, in the Bykovsky and Drew Point case studies, we observed in the residual pseudo-sections some regular lateral variations (see Fig. 3.3 and Fig. 3.8). This indicates that we were not completely explaining the data, either because of lateral subsurface resistivity variations or 3D effects. To tackle this problem, it could be beneficial to measure 3D bathymetric data around each ERT profile and collect additional parallel and perpendicular ERT profiles to better understand 3D resistivity variations at our field sites. Furthermore, direct measurement of the resistivity of water and unfrozen sediments (e.g., using additional water samples

and drilling cores) might help to inform the model parameterization (e.g., account for lateral variations) and inversion strategies. We should notice that adding complexity to our model parameterization comes with the trade-off of increased computational cost to solve the inverse problems. An alternative to obtaining more complex resistivity models is to use our layer-based global inversion results as reference models to perform smoothness-constrained inversions (e.g., Günther et al., 2006).

The error level of ERT data is usually unknown; especially for marine data, where repeated or reciprocal measurements are not practical because the data are acquired while the boat is moving. This represents a challenge during the inversion when specifying an appropriate fit level. One alternative to get insights into the noise level is to perform repeated measurements in a static fashion (avoiding bending of the cable by wind or swells) for a certain section of the profile. For example, this can be achieved at the coast on a calm day where one end of the cable is secured to the beach and the other end is fastened to an anchored boat. However, such repeat measurements were not available for our field sites. Therefore, we set our stopping criterion by considering a fixed number of iterations rather than using a minimum threshold in our objective function. With this approach, we obtained model solutions characterized by different fit levels. For example, for the Bykovsky data, we found RMSLE values between 0.025 and 0.038 (Fig. 3.3g-i), while for our Drew Point data, we found RMSLE values between 0.007 and 0.016 (Fig. 3.8i-l). Although the RMSLE values for Drew Point are significantly lower than for Bykovsky, we found a family of models in the Drew Point study, which was considered as geologically unrealistic (Fig. 3.7d). This highlights the importance of estimating different ensembles of solutions with different fit levels, and having an accurate estimate of data noise. Because the misfits for the model in Fig. 3.7d were higher, this family of models could potentially be discarded if they were found to exceed expected error levels without considering any prior knowledge of the environmental setting.

3.6.2 Parameter learning from 1D inversion

Our 2D inversion results showed large variations in the modeled resistivities of the permafrost, and we also noticed that, typically, the variabilities of IBPT position increase with depth. These observations indicate decreasing resolution capabilities of our ERT data with depth and limited penetration of the injected current in the frozen permafrost layers. To better understand these results in a more quantitative fashion, we reduced the number of parameters to five and performed selected 1D inversion experiments using synthetic data inspired by our 2D inversion results. Because such 1D inversions are significantly faster than 2D inversions, they represent an efficient way to explore the influence of constraining different parameters. For example, we noticed from our 1D inversion results that constraining the water layer significantly decreased the non-uniqueness of the inverse problem. This is essential for a reliable estimation of the IBPT position and for establishing petrophysical relations, for example, to estimate porewater salinity and ice content. Additionally, we noticed that the 1D inversion results for the Bykovsky data (Fig. 3.4c) provided similar uncertainties around the IBPT as the 2D inversion results at

$x = 150$ m (Fig. 3.2d-f). However, the 1D inversion results for the Drew Point data (Fig. 3.9c) showed uncertainties around the IBPT three times larger compared to the 2D inversion results at $x \approx 600$ m (Fig. 3.7f and g). This indicates that there is no general best way of using the results of such complementary synthetic 1D studies; the success and feasibility rather depends on the characteristics of the field site and analyzed data set. On the other hand, we can use our 1D inversion results to assess the posterior correlation matrix that, as we showed in our examples, can be helpful to identify interactions between the model parameters. Furthermore, comparing the changes across different posterior correlation matrices (e.g., associated with different model constraints) can help us detect changes in the parameters interactions and, thus, quantify the impact of our model constraints. Such straightforward but informative analysis provides a deeper understanding of the inversion process and the suitability of the entire inversion strategy.

Our 1D inversion results indicated some problems if we want to infer relative permafrost characteristics from ERT measurements. The 1D input models for our 1D synthetic examples (see Table 3.2 and Table 3.3) assumed identical resistivities of the ice-bearing permafrost layer ($\rho_p = 4{,}000$ Ωm) and similar resistivities for the unfrozen sediments as found by our 2D inversion results. In contrast, the resistivity and depth of the seawater layer between both models were set according to field measurements at our field sites. Although the resistivities of the unfrozen and frozen layers were similar in both models, we noticed that for model scenarios derived from the Bykovsky site, the inverted ρ_p values were generally overestimated where already the q_{25} model indicate ρ_p values larger than the input ρ_p (Fig. 3.4c). On the contrary, for settings inspired by the Drew Point field site, the input ρ_p fell within the range defined by q_{25} and q_{75} models but showed more significant variabilities than our 1D Bykovsky experiment (Fig. 3.9c). These results demonstrated the influence of the depth and resistivity of the seawater layer in the inverted models which may be critical for subsequent interpretations. For example, assuming the same temperature and porewater salinity, the resistivity of the sediments increases with ice-content (e.g., Pearson et al., 1986; Fortier et al., 1994; Kang and Lee, 2015). Thus, our results may lead us to conclude that the ice-bearing permafrost layer holds higher ice content at Bykovsky compared to Drew Point. Over- or under-estimating the ice-bearing permafrost resistivity may lead to potentially erroneous interpretations, for example, related to the sediment's ice content, temperature, and composition. We would need complementary field information or further analyses like sensitivity assessments to avoid misleading interpretations.

3.6.3 System understanding with sensitivity analysis

We obtained an additional model understanding (e.g., in view of delineating confident and reliable model areas) by performing sensitivity analyses. From our examples, we learned that if the resistivity of the seawater were higher than the resistivity of the unfrozen sediments (as in the Bykovsky case study, Fig. 3.5), this would result in increased sensitivities inside the unfrozen sediments and, thus, to changes along the IBPT position. This type of situation may

be prevalent in subsea permafrost areas affected by freshwater river discharge in summer. On the other hand, if the seawater were less resistive than the unfrozen sediments (e.g., as in the Drew Point case study, Fig. 3.10), we were more sensitive to the water layer and, therefore, to bathymetric changes. This emphasizes the importance of accurate water depth measurements. We highlight the fact that although the local 2D sensitivities for the Drew Point data were rather small for the unfrozen sediments, the IQR of the models (Fig. 3.7f-g) showed equivalent variability around the depth of IBPT (1.5 m to 2 m for depths $\sim$ 12 m) in comparison to the Bykovsky example (Fig. 3.2d-f), where the sensitivities showed a more pronounced influence within the unfrozen sediments.

This study used global sensitivity analysis considering only five parameters as needed for our 1D inversion examples. The Sobol approach proved to be a powerful method to distinguish the most influential parameters. After evaluating how the permafrost resistivity and the IBPT position may influence the rest of the parameters in our 1D three-layer examples, we noted some relevant differences. For example, in the Bykovsky example (Fig. 3.6), we noticed that for larger values of ρ_p and shallower z_{pt} the total influence of the rest of the parameters decreased. On the other hand, for the Drew Point example (Fig. 3.9), increasing ρ_p increased the total sensitivity of the rest of the parameters, while varying z_{pt} at shallower depths mainly increased the influence of ρ_w. We also want to highlight that ρ_w, ρ_{uf}, and z_{pt} were the parameters with the largest total sensitivity in both examples and were also the parameters that formed model parameter pairs showing the largest correlation (see Fig. 3.4d and Fig. 3.9d). Encouragingly, ρ_w and ρ_{uf} can be informed from CTD casts and shallow sediment sampling, respectively. We must be aware that such a global sensitivity analysis is highly dependent on the pre-defined constraining parameter range and should be applied to address specific questions to allow, for example, parameter reduction or to guide our sampling strategies and experimental design.

3.6.4 Subsea permafrost features (Bykovsky vs. Drew Point)

The inverted ERT profiles yielded new insights into how subsea permafrost thaws because the Bykovsky Peninsula and Drew Point are characterized by distinct seawater properties and geological histories. The Bykovsky 2D inversion results at x = 150 m, which corresponds to an inundation period of 357 years assuming an erosion rate of 0.42 m yr^{-1} (e.g., Lantuit et al., 2011), showed a median depth to the IBPT of $\sim$ 15 m (Fig. 3.2). This resulted in an average degradation rate of $\sim$ 0.04 m yr^{-1}. On the other hand, the Drew Point 2D inversion results at $x \approx$ 600 m showed a median depth to the IBPT of $\sim$ 12 m. Note that this location coincides with the 1955 coastline position (see Fig. 3.1d-e), which corresponds to 63 years of inundation yielding an average degradation rate of $\sim$ 0.19 m yr^{-1}. At Bykovsky, 63 years of inundation (again assuming an erosion rate of 0.42 m yr^{-1}) correspond to an offshore distance of $\sim$ 26 m which corresponds to a median IBPT depth in the 2D inversion results at most 6 m (Fig. 3.2). Although the mean annual IBPT degradation rate slows with inundation time as the temperature gradient driving diffusive heat fluxes weakens (Angelopoulos et al., 2019), it is evident that the permafrost at Drew Point may thaw faster, presumably because Drew Point

sediments are primed with salts in the pore space prior to inundation (Black, 1964; Sellmann, 1989).

Since salt diffusion is typically slower than heat diffusion (Harrison and Osterkamp, 1978), the IBPT degradation rate at Bykovsky should theoretically be faster than at Drew Point, provided that the permafrost sediments are similar. However, it appears that dissolved salts in the pore space of the sediments at Drew Point play an important role in lowering the permafrost freezing point and resulting in higher IBPT degradation rates than at Bykovsky. In fact, the top of onshore cryotic and saline unfrozen sediment layers (cryopegs) were observed near the Drew Point shoreline during coring (Bull et al., 2020; Bristol et al., 2021). This can lead us to interpret a faster IBPT degradation rate at Drew Point compared to Bykovsky in two ways: 1) a layer of submerged Drew Point sediments was already unfrozen upon inundation (e.g., $\boldsymbol{M}_{F2}$ in Fig. 3.7); 2) the frozen layers at Drew Point contained less ice and had a lower freezing point. Jones et al. (2018) suggested that warming permafrost temperatures at Drew Point (3 °C to 4 °C over the past several decades) have made saline permafrost more susceptible to erosion, potentially contributing to the enhanced coastal erosion rate (2.5 times that of the historical average) observed between 2007 and 2016. Warming by seawater submergence would presumably result in cryopeg spreading and IBPT degradation.

As shown in Fig. 3.1a and d, the coastal plains at our field sites consist of numerous thermokarst lakes and drained lake basins. When thermokarst lakes are breached by coastal erosion, the unfrozen sediments underneath the lake become integrated into the subsea permafrost environment, leading to bowl-shaped electrical resistivity structures. For example, Angelopoulos et al. (2021) showed steep IBPT gradients along ERT profiles parallel to the southern Bykovsky shoreline that traverse submerged thermokarst and undisturbed permafrost. These authors also suggested that drained lake basins, which have undergone thaw-refreeze cycles, are more susceptible to quicker thaw compared to undisturbed terrain. Comparing the first 400 m of our inverted median models for our field sites, we noticed that, in general, the IBPT at Drew Point is smoother than at Bykovsky. This might be the result of the higher erosion rates at Drew Point ($>$ 10 m yr^{-1}) than at Bykovsky ($<$ 1 m yr^{-1}) that expose coastal areas to inundation in a shorter time. Because of the longer inundation time at Bykovsky, we expect fluctuations in different environmental controls (e.g., water temperature, seawater salinity) that might result in step-like features as the one at $x \approx 280$ m. Furthermore, layered strata alternating between ice-rich and relatively ice-poor sediment may also contribute to step-like IBPT features. Similarly, in the Drew Point 2D inversion (Fig. 3.7a-c), there was a steep median IBPT decline observed at $x \approx 750$ m where the IBPT deepened from $\sim$ 12 m to $\geq$ 20 m. Although the resolution capabilities of our ERT data at these depths are limited, we suggest that thermokarst processes prior to seawater submergence may be responsible for the nature of this IBPT dip.

3.7 Conclusions

In this study, we illustrated how we could use ERT data to reliably estimate the IBPT position in shallow coastal areas of the Arctic. We found that using a layer-based model parameterization helps us target the IBPT position directly from the inversion of ERT data with the trade-off of omitting small-scale heterogeneities. To improve the inversion result, we noticed that constraining the water layer depth and resistivity reduces the non-uniqueness of the ERT inverse problem improving the estimation of the resistivity of the unfrozen sediments (talik and/or cryopeg) and the IBPT position. However, even when constraining the water layer, we still found large variabilities in the resistivity of the frozen sediments. We suggest that constraining the resistivity of the unfrozen sediments (e.g., sediment sampling) during ERT inversion could improve resistivity estimates of the frozen layer and, thus, further permafrost's physical properties (e.g., ice content). Properly imaging the IBPT position may allow us to improve the estimation of the permafrost degradation rate, which might be used to better understand greenhouse gas emissions and coastal erosion processes. The workflow and methods presented in this study can guide future field campaigns and may be used as a reference for more detailed parameterizations and/or inversion strategies.

3.8 Appendix - Smooth inversion

Although comparing different inversion strategies is beyond the scope of this study, for the sake of completeness, we show the smooth inversion results for our Bykovsky and Drew Point data sets in Fig. 3.12a-b. To invert these data sets, we use the inversion routine of the Python library pyGIMLi (Rücker et al., 2017). For both cases, we constrain the seawater layer by using the bathymetric profile data as collected by a Garmin echo sounder (see Section 3.3). The Bykovsky model (Fig. 3.12a) show the highest resistivities to the left (near the coast), while resistivities drop in the offshore direction. For our Drew Point model (Fig. 3.12b), the highest resistivities are also present near the coast, but the resistivities decrease in the offshore direction more gradually than in the Bykovsky model. To derive the IBPT position from these models, we would need to assume or measure (e.g., through borehole data) the resistivity threshold that separates the talik from the ice-bearing permafrost layer (e.g., Overduin et al., 2016; Sherman et al., 2017; Angelopoulos et al., 2021). Because no ground-truth data is available and to avoid assuming a resistivity threshold, we decide to target such an interface using a layer-based model parameterization approach as explained in Section 3.4.1. Please refer to Angelopoulos et al. (2019) where a smooth inversion of the Bykovsky data set presented in this study is discussed in more detail, as well as Angelopoulos et al. (2021) where laterally constrained inversions of additional datasets offshore of Bykovsky are shown.

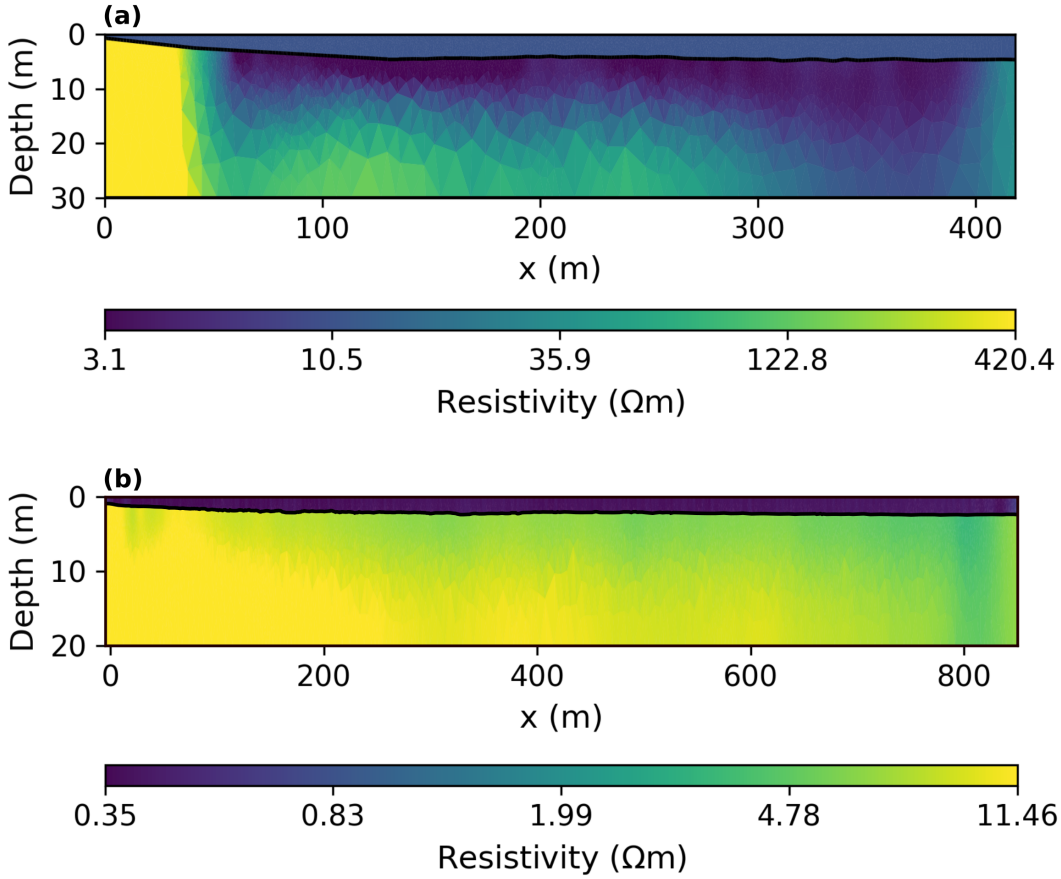

Fig. 3.12. Smooth inversion models for (a) the Bykovsky and (b) Drew Point data sets. To enhance the resistivity contrast in our ERT models presented in panels (a) and (b), we limited the lower and upper resistivities considering quantiles 0.04 and 0.96, respectively.

4

Tracing past extreme floods on an alluvial fan using geophysical surveying

---

This chapter was submitted (13.09.2022) for publication to the journal Earth Surface Processes and Landforms:

Arboleda-Zapata, M., Guillemoteau, J., Ana Lucía., Joachim Eberle, J., Tronicke, J., Korup, O., 2022. Tracing past extreme floods on an alluvial fan using geophysical surveying [manuscript submitted for publication*].

*Note that, unlike the rest of the chapters in this thesis, this chapter is written in British English to follow the guideline of the journal.

Abstract

In May 2016, a rare flash flood caused unprecedented erosion and sedimentation in several low-order tributaries of the Kocher and Jagst valleys in the cuesta landscape of southwestern Germany. While comparable events and their geomorphic and sedimentary legacy have been studied mostly in mountainous terrain, little evidence of such events in much gentler topography is known. In this study, we consider the Grimmbach alluvial fan near the village of Braunsbach, which was heavily impacted by sediment and wood loads during the 2016 flood. Sedimentary units in alluvial fans may reveal gradual transport and deposition during multiple floods or sediment-laden flows or, conversely, during few catastrophic events. To gain insights into the local sedimentary architecture and past floods, we explore the fanhead deposits of the Grimmbach using detailed topographic data and geophysical imaging based on electromagnetic induction, electrical resistivity tomography (ERT), and ground-penetrating radar. Our geophysical results reveal former channel courses and two coarse bar deposits up to 3 m below the surface, which are comparable with the more extensive bar deposits of the 2016 flood. From the ERT models, we interpret coarse, up to 5 m thick, gravel lag overlying bedrock at a maximum depth of 10 m. Our geophysical results also highlight patches of finer materials derived from gradual sedimentation and soil development. Overall, our results indicate that the Grimmbach alluvial fan may have formed and reshaped during catastrophic flows, which likely caused channel avulsions. Independent evidence comes from outcrops of cobble-rich layers that are comparable to those mobilised in the 2016 flood. Published radiocarbon dates indicate that at least three floods similar to the one in 2016 may have occurred since the 17th century. Our findings highlight the need to reconsider flash flood and debris-flow hazards in many similar headwaters and fans of this cuesta landscape in southern Germany.

4.1 Introduction

On May 29, 2016, heavy rainstorms delivered about 150 mm precipitation in a single day, and with a peak of 130 mm in only two hours (Bronstert et al., 2018), to different low-order tributaries of the Kocher and Jagst valleys in the cuesta landscape of southwestern Germany (Fig. 4.1). The rainstorm triggered flash floods and sediment-laden flows that entrained large amounts of soil from the plateau and coarse debris from the steeper creeks and hillslopes resulting in sediment-laden floods (Lucía et al., 2018; Ozturk et al., 2018). Judging from the extreme rainfall intensities, discharge, and sediment loads, the May 2016 flash flood has been considered a rare event for this region of moderate relief (Bronstert et al., 2018). Among the most affected areas were different catchments of the Braunsbach municipality, especially the Orlacher Bach catchment, which drains an area of $\sim$ 6 km^2 with an average slope of 0.12. This creek flows through the village centre of Braunsbach, and had a specific peak discharge of 12-30 $m^3s^{-1}km^{-2}$ estimated from a rainfall-runoff model (Bronstert et al., 2018); the lower limit of this estimate already exceeds the 100-year return level. Ozturk et al. (2018) inferred the volume of sediments moved at $\sim$ 7,000 m^3km^{-2} with yield rates that rival those of flash flood prone catchments in semiarid to Mediterranean climates. The adjacent catchment to the south, the Grimmbach catchment, was also severely affected. This catchment drains an area of $\sim$ 30 km^2, with an average slope of 0.11. Lucía et al. (2018) estimated a specific peak discharge for the Grimmbach creek of 23-25 $m^3s^{-1}km^{-2}$ using the Manning-Strickler formula. They also reported large wood recruitment of $\sim$ 167 m^3km^{-2}, similar to that in Orlacher Bach ($\sim$ 172 m^3km^{-2}). These rates are characteristic of much steeper catchments draining mountainous terrain (Lucía et al., 2018). Based on aerial photographs before and after the 2016 event, Lucía et al. (2018) also reported that the Grimmbach widened seven-fold on average, while the Orlacher Bach widened three-fold on average.

The alluvial fans impacted by the 2016 event may record information about past flash floods, thus filling in substantial knowledge gaps about the recurrence of such destructive events. The sediments stored in an alluvial fan are a fraction of those transported from its feeder catchment, but nonetheless document the legacy of floods, sediment-laden flows, and debris flows (Korup, 2004; Davies and Korup, 2007; Bruni et al., 2021). Careful investigations and analyses of such sediments may provide a key understanding of how and under which conditions sediments were transported, deposited, and preserved (e.g., Crosta and Frattini, 2004; Bardou and Jaboyedoff, 2008). Inferring the frequency of such events may help to inform and improve hazard models of extreme sediment transport (Santangelo et al., 2012; Crosta and Frattini, 2004; Schürch et al., 2016). The sedimentary architecture of alluvial fan systems results from different cycles of erosion and sedimentation (e.g., Harvey, 2012; Mather et al., 2017; de Haas et al., 2019). Yet studies in aggrading or recently aggraded settings can rely only on few, if any, natural exposures (Hickin et al., 2009). In this context, near-surface geophysical techniques can constrain the dimensions, internal architecture, composition, and petrophysical properties of different sedimentary units of alluvial fans (Hornung et al., 2010;

Schoch-Baumann et al., 2022).

Electrical, electromagnetic, and seismic imaging are among the most popular geophysical techniques for studying alluvial fans. For example, Hornung et al. (2010) and Franke et al. (2015) used ground-penetrating radar (GPR) data to probe the sedimentary architecture of two alluvial fans in the Swiss Alps up to depths of 10 m. These studies used GPR with 100 MHz and 200 MHz antennas to delineate former fan surfaces and depositional structures, which were attributed to environmental changes. Similarly, Ékes and Hickin (2001) used GPR with 50 MHz antennas to study a 40 m thick alluvial fan in the Coast Mountains of British Columbia, Canada. Schoch-Baumann et al. (2022) combined GPR with 40 MHz and 200 MHz antennas and electrical resistivity tomography (ERT) to characterise massive postglacial debris-flow deposits (up to 40 m deep) that generated large fans in the upper Rhone valley, Swiss Alps. Gonzales Amaya et al. (2019) applied ERT and transient electromagnetic induction methods to distinguish sediment calibre up to depths of 150 m on two alluvial fans in Valle Alto, Bolivia, to refine hydrogeological models in the area. Dietrich and Krautblatter (2017) showed that ERT can help to identify contacts between debris-flow deposits and morainic till of an alluvial fan in the Austrian Alps. Considering the interpreted interface and using an idealised pyramid model and inter- and extrapolations, these authors estimated the total Holocene/Lateglacial debris-flow volume of the studied alluvial fan. Savi et al. (2014) and Brardinoni et al. (2018) used seismic methods together with borehole data and radiocarbon dating to understand the postglacial sedimentary development of two alluvial fans in the Italian Alps with thicknesses exceeding 100 m. Both studies concluded that sedimentation rates in the investigated catchments decreased after the Last Glacial Maximum and provide evidence that the sediments of the corresponding alluvial fans are impacted by deep-seated gravitational slope deformations.

Most geophysical studies of alluvial fans have thus focused on mountainous terrain, where erosion and sediment deposition rates are high. Little is known, however, about the sedimentary architecture of alluvial fans in more moderate terrain with commensurately lower rates of geomorphic process activity. Even such seemingly quiescent fans can be subject to catastrophic events, such as those in the Olacher Bach and Grimmbach streams in 2016. Our objective is to test and evaluate whether and how well we can resolve evidence of past floods in the Grimmbach alluvial fan sediments with different geophysical imaging techniques, including electromagnetic induction (EMI), ERT, and GPR.

4.2 Study area

Our study focuses on the catchment outlet of the Grimmbach, with its ~ 0.1 km^2 large alluvial fan at the confluence with the Kocher river near the village of Braunsbach, northeastern Baden-Württemberg, Germany (Fig. 4.1a). The annual average temperature in this region is 8.6 °C, and the mean annual precipitation is 860 mm, representing a temperate oceanic climate (Bronstert et al., 2018). The Grimmbach catchment is part of the regional cuesta landscape,

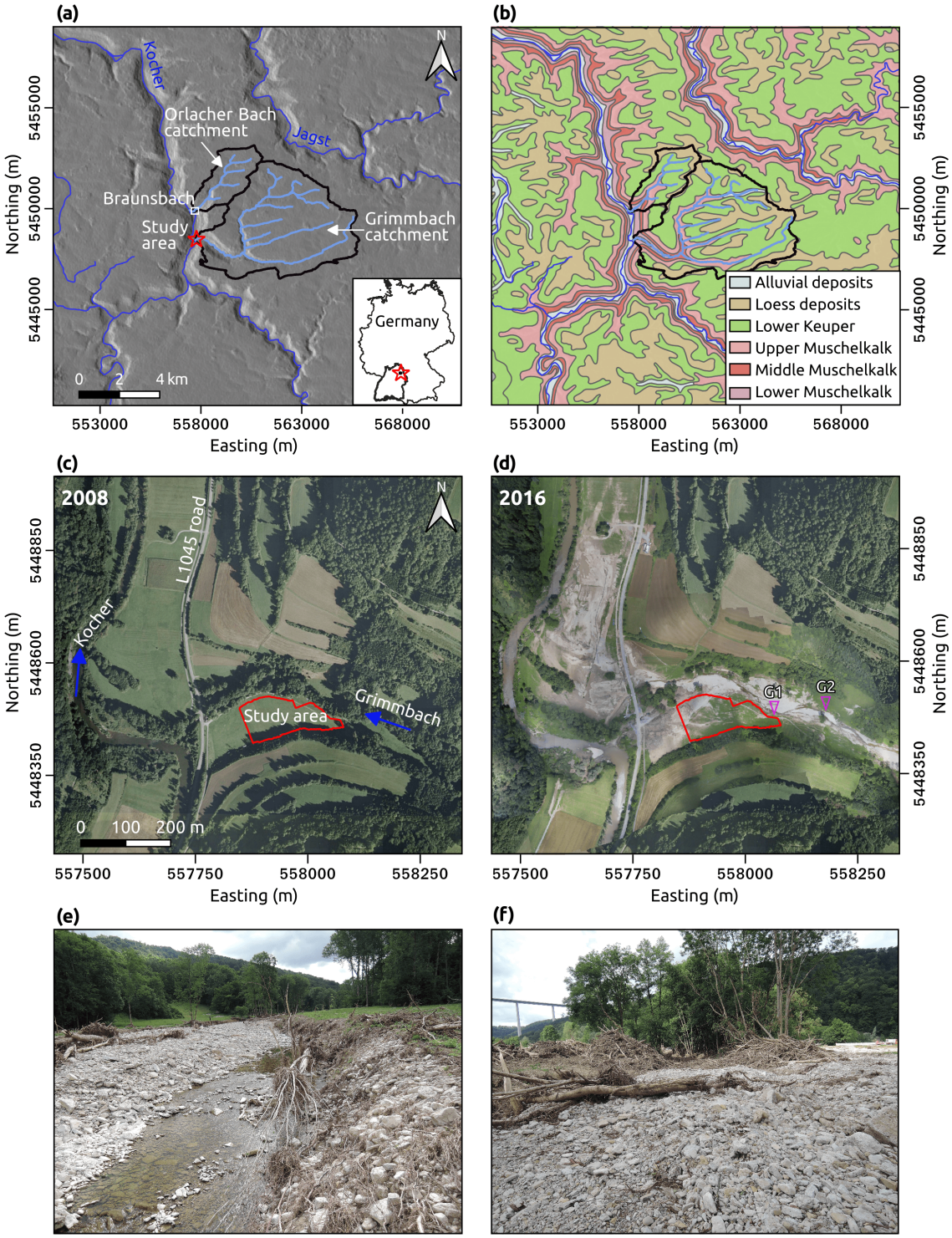

Fig. 4.1. General setting of our study area and context of the 2016 flash flood. (a) Hillshaded digital elevation model of the cuesta landscape in northeastern Baden-Württemberg, Germany derived from the Shuttle Radar Topography Mission data (lpdaac.usgs.gov/products/srtmgl1v003/). (b) Geological map in scale 1:300,000 adapted from the Landesamt für Geologie, Rohstoffe und Bergbau, Baden-Württemberg. (c) Google Earth image of the Grimmbach alluvial fan taken in December 2008. (d) Orthophoto taken one month after the May 2016 sediment-laden flood with the location of cut-bank profiles, G1 and G2, from Schönleber et al. (2022). Photos of coarse debris deposits (e) upstream and (f) downstream moved during the 2016 flash flood. We used UTM zone 32 N (EPSG:25832) coordinate system in panels (a-d).

where numerous creeks dissect the Kocher-Jagst plateau forming short, steep, and gully-like valleys with rectangular drainage patterns (Fig. 4.1a). The headwaters of the Grimmbach are located on a plateau at a height between 420 m and 460 m a.s.l. The plateau surface is gently inclined (slopes up to ~ 0.05) and mainly used for agriculture, small settlements, and rural roads except for highway A6, which crosses the plateau along the southern catchment boundary. The headwater streams are narrow, steep (local slopes of up to 1.1), and mostly covered by forest. In total, the Grimmbach drains an area of about 30 km^2 with an average slope of ~ 0.11. The stream flows across the plateau for ~ 4 km before cutting into bedrock at the plateau margin, running another 6.6 km before joining the Kocher river at the height of ~ 245 m a.s.l. The average slope of the stream along 4 km upstream of this confluence is 0.024, characterised by a single-thread to braided river pattern (Schönleber et al., 2022).

The geological map in scale 1:300,000 by the Landesamt für Geologie, Rohstoffe und Bergbau, Baden-Württemberg (LGRB, maps.lgrb-bw.de/) depicts the underlying geology as mainly horizontal Triassic calcareous rocks (Fig. 4.1b). The plateau is mainly formed by the Lower Keuper formation (Upper Triassic), featuring claystone, marlstone, sandstone, and dolomite beds. When weathered, these rocks produce loamy-clayey Cambisols and Luvisols, while some soils on the plateau derive from Quaternary loess. These plateau soils have low permeability and saturate quickly following rain (Schönleber et al., 2022). According to the LGRB, the plateau soils are prone to moderate to high annual erosion rates ranging from 100 t/km^2 to 600 t/km^2. Incised creeks expose different sections of the Middle Triassic Muschelkalk formation including the Upper, Middle, and Lower Muschelkalk units, featuring limestone, marlstone, dolomite rocks, claystone, and sandstone. Lenses of gypsum, anhydrite, and salt are common, especially in the Middle Muschelkalk formations. The uppermost reaches of the Grimmbach run along the Upper Muschelkalk, whereas the middle reaches are dominated by the Middle Muschelkalk, which can be traced topographically by more gentle slopes. The lower Muschelkalk is present in the lowermost flanks of the last 2 km of the Grimmbach and exposed in a cliff on the left flank of the Kocher opposite the Grimmbach outlet. The main soil types are Calcaric Leptosols and Calcaric Regosols, which are less than 0.5 m thick. The active channel bed of the Grimmbach alluvial fan runs along the true right and is incised into the floodplain by up to 2 m, exposing alternating unconsolidated fine and coarse beds.

4.3 Geophysical surveying

To gain insights into the sedimentary architecture of the Grimmbach alluvial fan, we performed two geophysical field campaigns in November 2019 and September 2020. In the first campaign, we collected ERT and GPR data, while in the second we collected EMI (including topography as a by-product of our EMI surveying strategy) and additional ERT data. In this study, we use the term "electrical conductivity" instead of its reciprocal, "electrical resistivity", to avoid switching units when referring to EMI and ERT data and models. We are not considering other kinds of conductivities (e.g., hydraulic or thermal conductivities); therefore, in this study, con-

ductivity refers to electrical conductivity.

Fan sediments feature high electrical conductivity contrasts (e.g., Gonzales Amaya et al., 2019; Schoch-Baumann et al., 2022), which is ideal for electromagnetic and ERT techniques. Low conductivity values (resulting from EMI and ERT measurements) and high GPR amplitudes are often related to coarse materials, while high conductivity values and low GPR amplitudes indicate sandy to loamy materials. We perform soundings along different profile lines (Fig. 4.2a) to visualise the general structural sedimentation patterns and to infer the spatial context of sub-surface deposits like channels, lobes, levees, and soils.

Our geophysical measurements focused on the fanhead (Fig. 4.2a-e), where there is an inactive 2 m high floodplain to the left of the active channel of the Grimmbach. This location allowed us to focus more on past geomorphic processes associated with the Grimmbach rather than those resulting from the interactions of the Grimmbach with the Kocher. The surveyed area is mainly used for grazing and is free of infrastructure, except for a minor unpaved road parallel to the Grimmbach stream (Fig. 4.2c-d). Some 50 m downstream from our surveyed area, the state road L1045 with a parallel cycle-path crosses the alluvial fan (Fig. 4.1c). To avoid repetition, we provide in the following brief outlines of each geophysical technique used at our field site together with the relevant findings.

4.3.1 Electromagnetic induction (EMI)

An EMI device (loop-loop system) consists of one transmitter loop emitting a time-harmonic electromagnetic field that induces eddy currents in the subsurface. These eddy currents generate a secondary magnetic field, which is sensed by a receiver loop. The recorded secondary magnetic field is proportional to the subsurface electrical conductivity (McNeill, 1980). Using coils with different orientations (e.g., vertical and horizontal) and spacings allows the estimation of the subsurface electrical conductivity at different depths and within different subsurface volumes. By moving an array of coils along multiple profile lines, we can recover (after inversion) a 3D subsurface distribution of conductivity (e.g., von Hebel et al., 2014; Guillemoteau and Tronicke, 2016; Guillemoteau et al., 2017).

We collected our EMI data in September 2020 using a DUALEM-21S system mounted on a cart at a fixed height of 0.25 m above the ground surface. This system consists of a horizontal transmitter coil (operating at 9 kHz), and two horizontal (HCP) and two vertical (PERPx) receiver coils. The HCP coils are located at 1 m and 2 m offset from the transmitter coil, while the PERPx coils are at distances of 1.1 m and 2.1 m. Following Böniger and Tronicke (2010), we recorded the relative positions (x-, y-, and z-coordinates) using a self-tracking total station to localise our EMI data and to generate a digital elevation model of the surveyed area (Fig. 4.2b). We collected data points following profile lines approximately perpendicular to the Grimmbach valley axis to target linear or elongated deposits such as channel fills, bars, and levees with suspected main axes aligned along that of the valley. In total, we collected 387

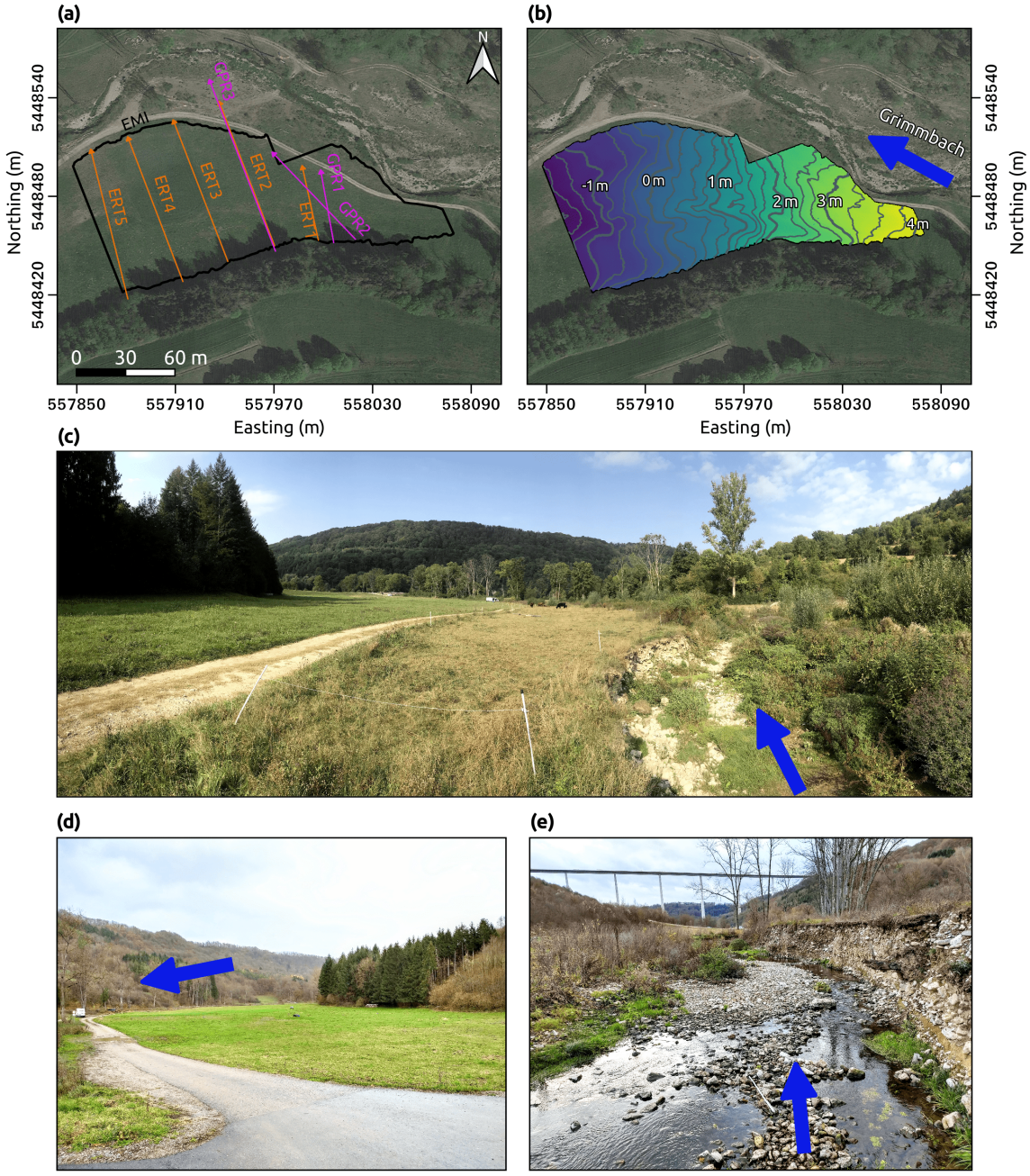

Fig. 4.2. Details of our study area on the Grimmbach alluvial fan. (a) location of geophysical soundings; the tail and head of the thin arrows indicate the origin and end of each profile, respectively. (b) Elevation map (altitude above a reference point) obtained alongside EMI measurements. (c) Photo of the study area from upstream and (d) downstream. (e) Detail of the active channel and its right cut bank deposits. Thick blue arrows in panels (b-e) indicate flow direction. In panels (a-b), we used a background Google Earth image (2020) presented in the UTM zone 32 N (EPSG:25832) coordinate system.

lines with a spacing of $\sim$ 0.5 m and an in-line average point spacing of $\sim$ 0.07 m covering an area of $\sim$ 13,800 m^2, which resulted in 397,544 four-configuration soundings (after removing low-quality data points).

We inverted the EMI data set using the full non-linear 1D laterally constrained inversion

based on the minimum gradient support regularisation, as proposed by Klose et al. (2022). For the inversion, we resampled our data to obtain in-line and cross-line sounding spacings of $\sim$ 0.5 m in the resulting pseudo-3D model. The focusing parameter was set to 1, and the number of layers to 15 with increasing thickness towards deeper layers. The deepest layer is an infinite homogeneous half-space whose top boundary was set at a depth of 4 m.

In Fig. 4.3a-e, we present our EMI inversion results. To visualise our 3D model, we extracted two horizontal slices at depths of 1 m and 2 m, and two profiles (vertical slices EMI1 and EMI2) at the locations of profiles ERT2 and ERT5, respectively (see also Fig. 4.2a). In Fig. 4.3a, we highlight three main structures labelled C1, R1, and R2. Structure C1 spans the entire length of the southern survey area and shows high conductivities (> 0.02 Sm^{-1}). It appears to be several meters wide upstream (eastward) and narrows in the downstream (westward) direction. The low conductive structure R1 represents a linear pattern of conductivities < 0.003 Sm^{-1} that separates into two sub-parallel branches downstream. Another notable low conductivity structure (labelled R2) in the northeastern part of the survey area is characterised by a semicircular shape and slightly higher conductivities than R1. In the vertical slices at 1 m and 2 m (Fig. 4.3b-c), C1 and R1 are still traceable at these depths, while R2 is almost absent at a depth of 2 m. Our 2D profiles EMI1 and EMI2 (Fig. 4.3d-e) show that C1 is well defined down to 1 m depth, though it can reach depths below 3 m with sightly lower conductivities (Fig. 4.3d). Profiles EMI1 and EMI2 indicate that R1 is $\sim$ 3 m thick while profile EMI1 shows a maximum depth of $\sim$ 2 m for R2. The effective investigation depths for our EMI models is $\sim$ 3 m; hence the maximum depth of R1 needs to be evaluated using our deeper penetrating ERT data.

4.3.2 Electrical resistivity tomography (ERT)

During ERT data collection, an electric current is injected into the ground through two electrodes (current electrodes) and the voltage is measured using another pair of electrodes (voltage electrodes). Systematically moving such a four-electrode array configuration along a profile and increasing the electrode spacing allows for recording a 2D pseudo-section of apparent electrical conductivity, which needs to be inverted to obtain a 2D subsurface model of electrical conductivity.

We collected five semi-parallel profiles about 30 m apart from each other during two different field campaigns (Fig. 4.2a). Two ERT profiles (ERT2 and ERT5) were collected in November 2019 under moist conditions with some light rain and wet soils, while the other three (ERT1, ERT3, and ERT4) were collected in September 2020 (like the EMI data) under dry conditions without rain before or during surveying. We used a Syscal Pro system considering a Wenner-Schlumberger array configuration with an in-line electrode spacing of 1 m. Using 48 electrodes for profile ERT1 and 96 electrodes for profiles ERT2 to ERT5, we recorded 564, 2209, 2376, 2376, and 2209 apparent conductivity measurements for profiles ERT1 to ERT5, respectively.

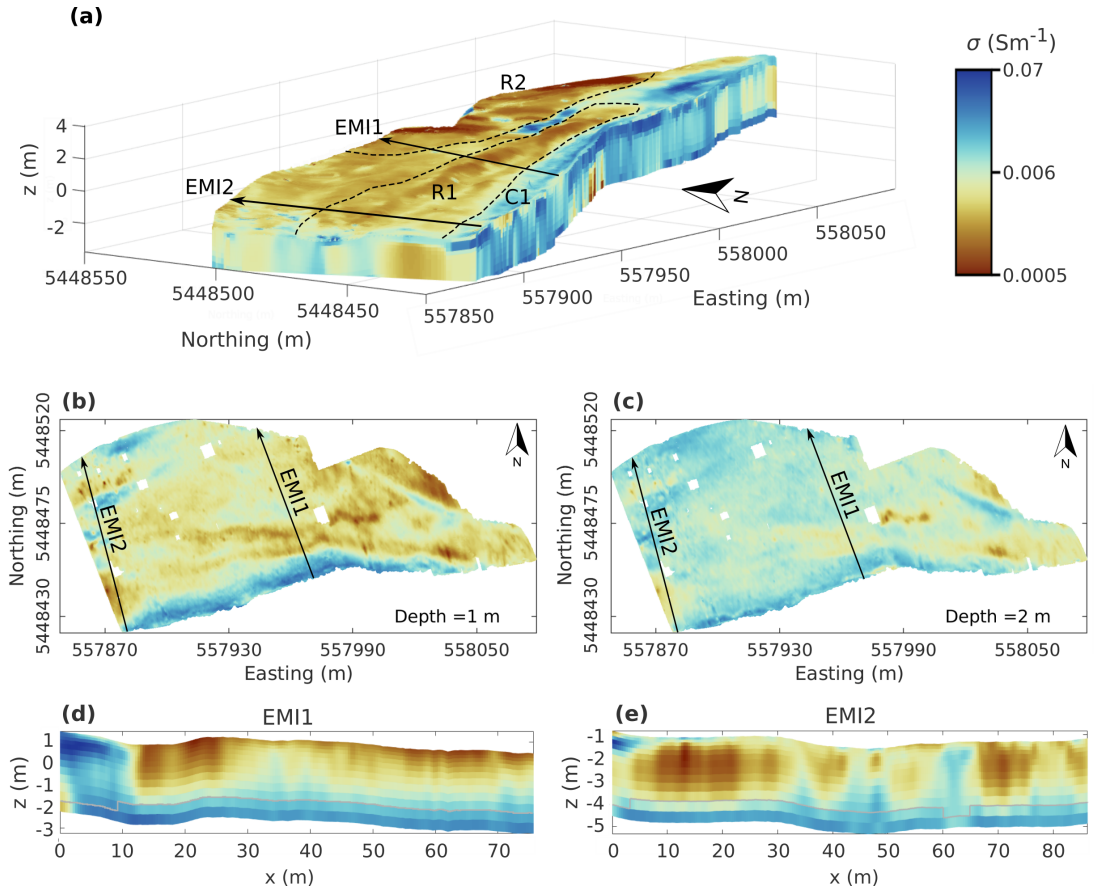

Fig. 4.3. Inverted electrical conductivity model of the EMI data. (a) 3D view of the EMI conductivity model. (b) Horizontal slices at 1 m and (c) 2 m depth. (d) Vertical slices (2D profiles) EMI1 and (e) EMI2 with effective investigation depth shown as grey lines. Panels (b-e) share the same colour map as shown in panel (a). In panels (b) and (c), the tail and head of the arrows indicate the origin and end of each profile, respectively.

We inverted our ERT data using the open-source finite-element library pyGIMLi (Rücker et al., 2017). To favour geologically plausible models consistent with our geological understanding of the Grimmbach fan, we considered different geostatistical regularisation constraints as proposed by Jordi et al. (2018). For this inversion strategy, we need to set four parameters: the regularisation or trade-off parameter λ, the correlation lengths along the horizontal (Cx) and vertical (Cz) axes, and a rotation angle to describe inclined structures. After some initial parameter testing, we found that $1 < \lambda < 20$ provided similar and stable results and fixed $\lambda = 10$. For the correlation lengths, we follow Gelhar (1993) and Tronicke and Holliger (2005) who suggest a ratio Cz/Cx of about 0.1 to characterise alluvial sediments. We considered Cx-Cz pairs (in units of meters) of [10, 1], [20, 2], [30, 3], and [40, 4], which is also consistent with the size of the structures observed in the channel bank and current channel deposits (Fig. 4.1e-f, and Fig. 4.2c, and e), as well as our EMI results (Fig. 4.3). Because we expect horizontal to sub-horizontal structures, we fix the rotation angle at zero degrees.

In Fig. 4.4, we present the inversion results for ERT2, which show consistent models of the overall electrical conductivity structure for the different pairs of correlation lengths considered. Larger correlation lengths result in slightly smoother models with similar relative root mean

square errors (RRMSE) shown at the bottom right of Fig. 4.4a-d. These results demonstrate that using different reasonable correlation lengths yields similar results, which is comparable to the findings of Jordi et al. (2018). Therefore, we chose $Cx = 20$ m and $Cz = 2$ m to invert all our ERT data sets consistently. In Fig. 4.5a-e, we illustrate the resulting electrical conductivity models. All of these models are characterised by alternating (sub-)horizontal layers of high and low conductivity with some horizontal variations. We recall that, because of different weather and soil moisture conditions, the conductivity values of the ERT profiles collected in summer 2020 show overall lower conductivity values than those collected in autumn 2019, especially in the shallowest parts. Thus, we display our results considering different colour scales to highlight conductivity contrasts and structures, respectively. Yet, some of the most prominent structures, although showing different absolute values of conductivity, can be tracked between neighbouring profiles. For example, the low conductive structure on the right side of all profiles between 5 m to 10 m depth is evident in all models.

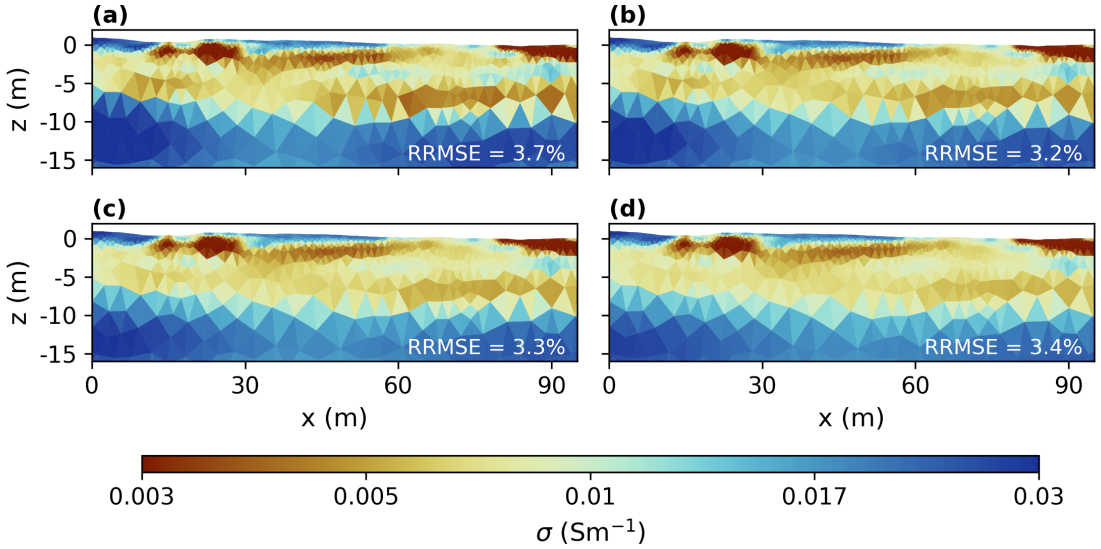

Fig. 4.4. Inverted electrical conductivity models of profile ERT2 considering different horizontal (Cx) and vertical (Cz) correlation lengths for geostatistical regularisation during data inversion. (a) $Cx = 10$ m and $Cz = 1$ m, (b) $Cx = 20$ m and $Cz = 2$ m, (c) $Cx = 30$ m and $Cz = 3$ m, and (d) $Cx = 40$ m and $Cz = 4$ m.

4.3.3 Ground-penetrating radar (GPR)

A GPR system emits a high-frequency electromagnetic wavelet (for geological applications, commonly in the order of 40 MHz to 500 MHz) from a transmitter antenna into the subsurface. The wavefield is reflected at interfaces where the dielectric properties change and is recorded by a receiver antenna. By moving the pair of antennas along a profile, we obtain, after some data processing, a 2D image of subsurface structures such as layer interfaces in sedimentary environments.

We collected our GPR data in November 2019 using a PulseEKKo Pro GPR system equipped with a pair of 100 MHz antennas mounted on a sledge with a fixed offset of 1 m.

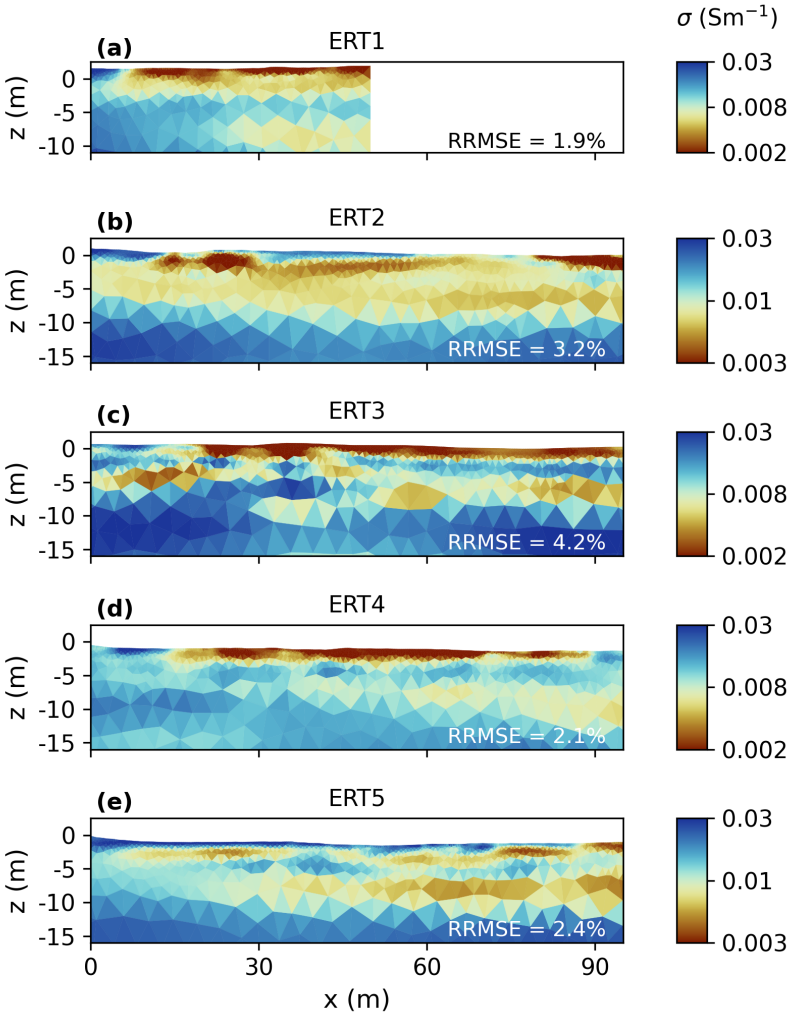

Fig. 4.5. Inverted electrical conductivity models of the five profiles ERT1 to ERT5 (for locations see Fig. 4.2a) considering correlation lengths of $Cx = 20$ m and $Cz = 2$ m. Note that the colour bar varies for the data sets collected in late autumn 2019 (ERT2, ERT5) and late summer 2020 (ERT1, ERT3, ERT4).

Similar to our EMI survey, the positions of the recorded traces were measured using a self-tracking total station (Böniger and Tronicke, 2010). We also collected common-midpoint (CMP) data to derive a subsurface propagation velocity of 0.077 m/ns using spectral velocity analysis. This velocity estimate is used for migrating our common-offset data and to perform a time-to-depth conversion. We also consider other standard data processing steps such as band-pass filtering, amplitude scaling, and removing the direct arrivals of the air and ground waves by applying a local background removal.

In Fig. 4.6 and Fig. 4.7a, we present the migrated profiles GPR1, GPR2, and GPR3 using a conventional grey-scale colour map ranging from white (minimum negative amplitudes) to black (maximum positive amplitudes) colors. These GPR lines are characterised by continuous events that vary laterally in amplitude. We can also identify locally some concave-up reflectors as pointed by the white arrows in Fig. 4.6 and Fig. 4.7a and a concave-down reflector highlighted by the dashed line in Fig. 4.7a. In general, areas with higher amplitudes are partly

associated with larger penetration depths (up to 3 m). The overall penetration depth is limited to $\sim$ 2 m. For a qualitative comparison between the profile GPR3 and the subsurface electrical conductivity from our EMI and ERT data, we superimpose the EMI1 (Fig. 4.3d) and ERT2 (Fig. 4.4d) models onto the migrated GPR3 data Fig. 4.7b-c, respectively. A one-one comparison of the conductivities from EMI1 and ERT2 is intractable because they were collected under different soil moisture conditions. However, we still expect some correlation associated with the main structures. For example, we notice in profile GPR3 that the high amplitudes in the concave-down structure correspond to low conductivities in models EMI1 and ERT2. In contrast, low amplitudes like the ones observed at the beginning of our profile ($x < 10$ m) and at 35 m $< x <$ 55 m are associated with high conductivities.

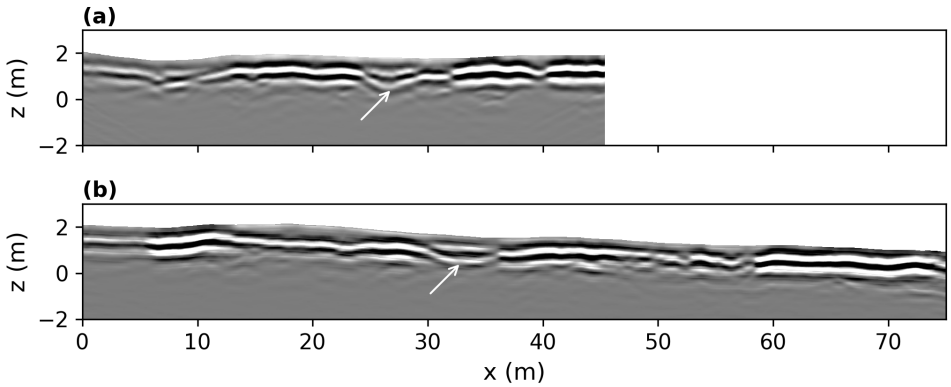

Fig. 4.6. GPR cross sections. (a) GPR1, (b) GPR2 profiles (see locations in Fig. 4.2). The white arrows point to concave-up structures.

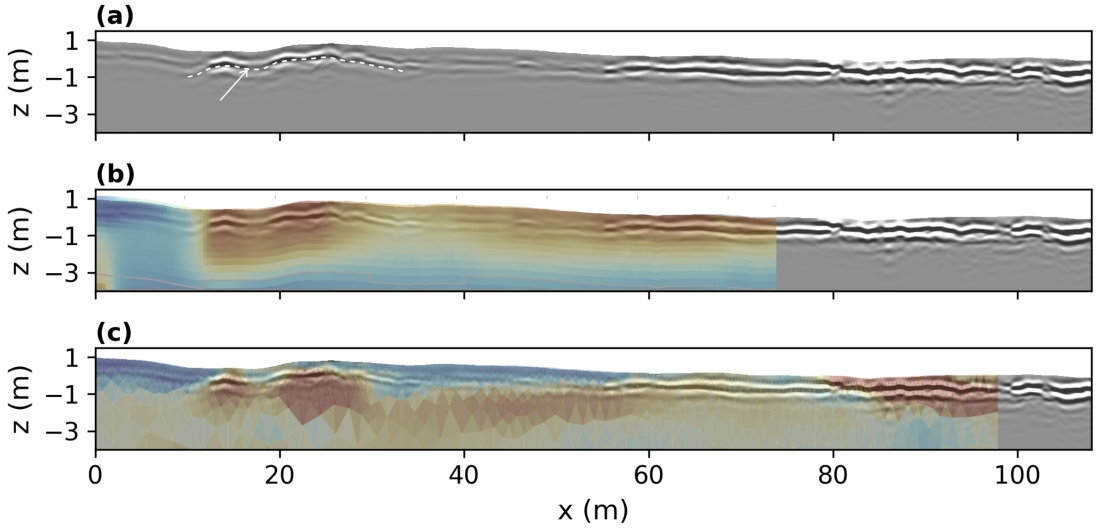

Fig. 4.7. Comparing GPR with electrical conductivity responses. (a) GPR3 profile overlying (b) EMI1 and (c) ERT2 models. The white dashed line in panel (a) indicates a general concave-down structure with a little concave-up structure marked by the white arrow. In panels (b) and (c), we use the same colour map as in Fig. 4.3a and Fig. 4.5b.

4.4 Discussion

4.4.1 Past hydro-geomorphic events recorded in the Grimmbach fan

Our geophysical data provide insights into the geomorphic and sedimentary history of the lower Grimmbach. Reconciling all geophysical and geological information, we identify both elliptic structures and linear patterns below the fan surface (black and blue dashed lines, respectively, Fig. 4.8). We interpret the elliptical structures as former bars, while the linear structures likely correspond to former channels.

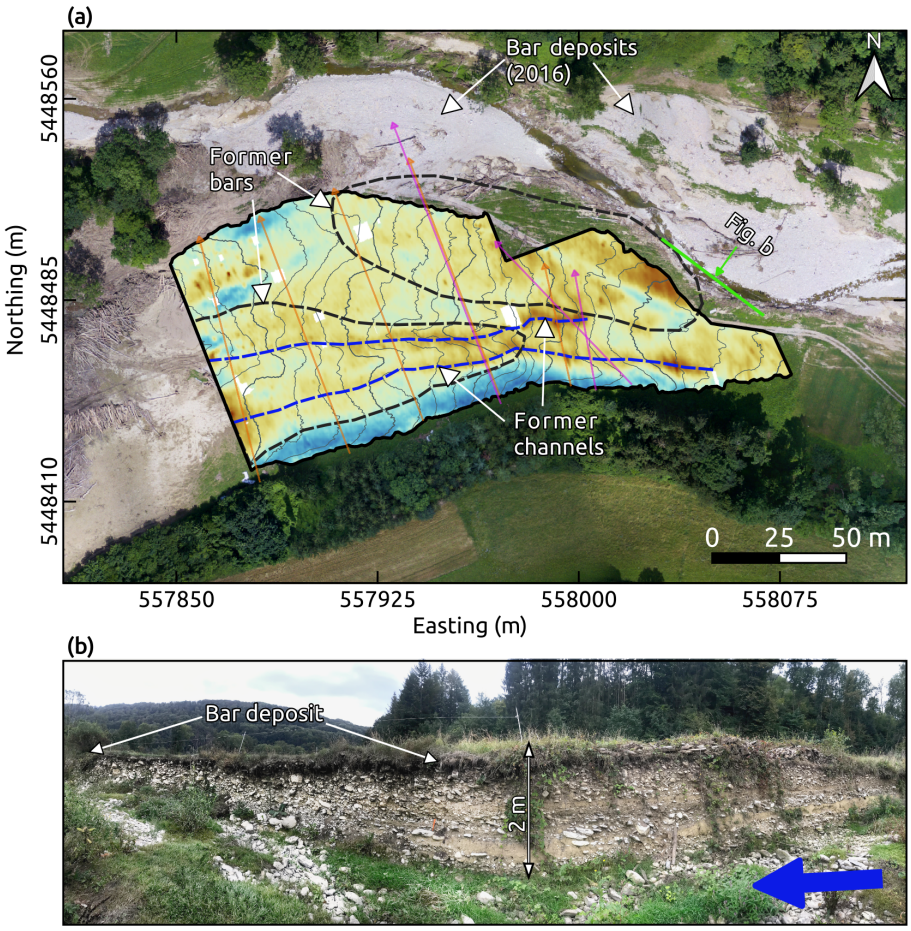

Fig. 4.8. Sedimentary evidence of abrupt channel shift (avulsion) and inferred past flash floods deposits. (a) EMI slice at 1 m depth (with the same colour map for visualising EMI conductivities as in Fig. 4.3) including elevation contours (Fig. 4.2b), and profile locations (with the same symbols and colours as in Fig. 4.2a). (b) Panoramic view of an outcrop upstream of our study area (blue arrow indicates flow direction); approximate location is shown in panel (a).

The bar structure to the far left of the current channel has an area of ~ 4000 m^2 (Fig. 4.8a) and is ~ 3 m thick (Fig. 4.7b-c). Judging by the shape of this structure, we are likely only seeing a fraction of its total size, which may extend in the downstream direction. Our profile GPR3 (Fig. 4.7a) crosses this structure upstream and shows a concave-down structure at

10 m $< x <$ 35 m, with a minor concave-up structure at $x = 17$ m. Although our profiles GPR1 and GPR2 do not cross this inferred bar, they also show concave-up structures (Fig. 4.6) that can be followed downstream in our EMI model as low conductive bodies (Fig. 4.8). These linear structures are likely former channels that are associated with the bar; a modern analogy of this sedimentary association is exposed along the active cut banks as in Fig. 4.1e.

The interpreted bar closer to the current channel has an area of $\sim$ 5000 m^2 (Fig. 4.8a) and is $\sim$ 2 m thick (Fig. 4.3). This structure is characterised in our EMI model (Fig. 4.8a) by low conductivities upstream that gradually increase downstream, likely reflecting sediments of decreasing calibre. We extended the interpretation of this structure in the direction of the current channel considering the ERT2 and GPR3 profiles (Fig. 4.7c), in which we noticed at 35 m $< x <$ 60 m and $z =$ -2 m low conductivities and at 60 m $< x <$ 80 m and $z = 0$ m intermediate conductivities and a flat-lying, high-amplitude GPR reflector. We interpret the low conductive and high-amplitude GPR reflectors at 80 m $< x <$ 100 m in Fig. 4.7c as amalgamated bar deposits containing in the shallowest part coarse deposits from the 2016 flood (see Fig. 4.8a). Profiles GPR1 and GPR2 also cross this structure upstream with similar responses to GPR3; however, these profiles are too short for delineating the outer boundary of the bar. Therefore, we delineate the upstream limit of this bar structure by considering a 2 m height outcrop (Fig. 4.8b) characterised by a sudden transition of layered sediments to a poorly stratified layer consisting of up to 50 cm large cobbles, which are consistent with a coarse-grained bar deposit.

To investigate deeper structures in the Grimmbach valley fill including the depth to bedrock, we rely on our ERT conductivity models, which effectively reach depths of up to $\sim$ 16 m. We interpret bedrock in our ERT models as the lowermost conductive layer at maximum depths of $\sim$ 10 m. This interpretation agrees with two boreholes in the nearby Orlacher Bach alluvial fan, in which depth to bedrock was found at 12 m to 13 m below ground surface (Ozturk et al., 2018). However, to confirm and validate this interpretation, complementary geophysical surveys such as seismic refraction (e.g., Juhojuntti and Kamm, 2015) or borehole-based explorations are needed. Furthermore, using layer-based parameterisation approaches to invert the geophysical data (e.g., Arboleda-Zapata et al., 2022a,b) might be helpful to resolve the bedrock structure. Overlying this inferred bedrock, all ERT profiles show a low conductive layer with a thickness of up to 5 m, which may represent coarse gravel lag deposits. The layer may also indicate massive sedimentation following bedrock incision in the early history recorded by this alluvial fan. This coarse layer is topped by a more conductive layer, indicating finer sediments deposited by either less competent flows or distal portions of high-energy flows linked to sediment depletion upstream. Like in our EMI inversions, the shallowest sediments ($<$ 3 m) are characterised by low conductivities associated with channels and bars, and may indicate a new, younger cycle of fine to coarse sedimentation.

Repeated deposition and entrenchment have formed intercalated fine and coarse beds,

such as those exposed along the cut channel banks in the Grimmbach fanhead (Fig. 4.2e, and Fig. 4.8b). While the gravel beds can be interpreted as evidence of past floods, the fine layers were likely formed during periods of relative geomorphic quiescence, favouring the gradual accumulation of fine particles and soil development. Some loamy to sandy layers could also represent overbank deposits dumped by the Kocher river (e.g., Schönleber et al., 2022). From our geophysical results, we can infer the location of some fine-grain lenses in the floodplain. For example, we interpret the linear, high conductive structure at the extreme left of the active channel (C1 in Fig. 4.3a) as a silty/clayey bed. This bed likely corresponds to a colluvial deposit associated with the steep and vegetated slope that abuts the Grimmbach channel to the south (Fig. 4.8a). These colluvial deposits correspond to the slightly inclined low amplitude reflector located in the first section of our GPR profiles (Fig. 4.6 and Fig. 4.7a). In the profile GPR3 (Fig. 4.7a), a similar structure is observed adjacent to the interpreted former channel at 35 m $< x <$ 55 m. Assuming a common origin for these units, we can infer that such colluvial deposits were incised by the inferred former channel in Fig. 4.8a.

4.4.2 Independent evidence

Sedimentary records and historical evidence suggest that flash floods like the one in 2016 had occurred in this region earlier. Ozturk et al. (2018) showed photographic records of massive sedimentation of debris, mud, and large wood on June 12, 1927, covering houses and roads in Cröffelbach, which has a similar-sized alluvial fan 5 km southeast of Braunsbach. These authors also interpreted poorly rounded limestone clasts of the uppermost 4 m of a borehole in the alluvial fan of the Orlacher Bach (in the village of Braunsbach) as past debris-flow deposits.

Ozturk et al. (2018) suggested that the Orlacher Bach is prone to major sediment pulses even during rainstorms of lower intensities than the one observed in 2016. The situation may differ for the Grimmbach given its wider floodplain, larger channel, and lower slope. These characteristics only favour sediment transport over short distances. Only major flash floods such as the one in 2016, which transported blocks of up to 0.5 m, may be capable of leaving distinct sedimentary evidence in the alluvial fan beds (e.g., Lucía et al., 2018). The displacement of the Kocher channel by the fans of the Grimmbach and Orlacher Bach indicates that these creeks contribute substantial sediment loads that the trunk channel is unable to evacuate swiftly.

Assuming that coarser materials of the Grimmbach can only be mobilised by discharges similar to that during the 2016 flood of up to 25 $m^3s^{-1}km^{-2}$ (Lucía et al., 2018), we interpret the coarse layers intercalated with sandy-loamy layers as deposits from past flash floods. Schönleber et al. (2022) reported detailed sedimentary analyses and radiocarbon dates of two cut-bank profiles of the Grimmbach alluvial fan (G1 and G2 Fig. 4.9a-b) and proposed that at least another three flash floods may have occurred in the Grimmbach catchment since the 17th century. These historical events may have had magnitudes similar to the one in 2016.

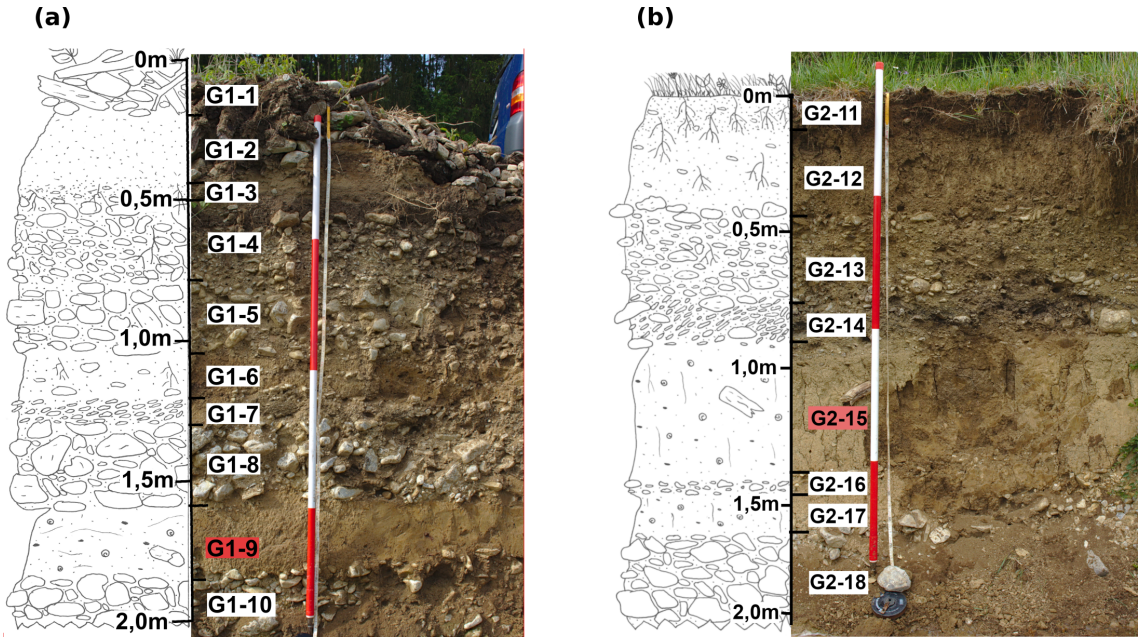

Fig. 4.9. Stratigraphic sections of the Grimmbach alluvial fan from Schönleber et al. (2022). (a) profile G1 and (b) G2 with the locations indicated in Fig. 4.1d. The units G1-9 and G2-15 highlighted in red were sampled for radiocarbon dating.

The 2016 flood highlighted how the Grimmbach alluvial fan had changed during a single flash flood, when most of the sediments that reached the alluvial fan were deposited in the widened channel and also on the $\sim$ 2 m high floodplain. These overbank deposits top a fine material layer with a sharp contact between units G1-1 and G1-2 (Fig. 4.9a). Similar contacts are at deeper levels like the one between units G1-8 and G1-9. Aerial photos taken after the 2016 flood show that coarser sediments remained on the fanhead, while finer sediments spread out over the distal fan after overcoming the state road L1045 (Fig. 4.1d). Without any engineering interventions, this event could have caused an avulsion, thus pushing the Grimmbach toward its right flank (Fig. 4.1d).

The 2016 flood formed bar deposits with sizes of up to 5,000 m^2 with thickness < 1 m. Our two inferred bars have similar areas (Fig. 4.8a) though they are likely thicker. For the bar deposit adjacent to the current channel, some faint bedding supports the idea of several deposition episodes instead of a single one, calling for a more detailed and rigorous sedimentological study of more outcrops as they emerge. However, we lack available outcrops in the southern part of our surveyed area to check if this gravelly deposit may correspond to a single or multiple floods.

In Fig. 4.10d, we summarise our general understanding of the sedimentary architecture of the Grimmbach fanhead. We consider the section along the profile ERT2 and extend it to both flanks of the current channel. The bedrock is interpreted as a bowl-shaped valley with a maximum depth of 10 m. The bedrock at this location corresponds to the Lower Muschelkalk formation, which is outcropping on the left flank of the Kocher opposite the Grimmbach outlet (see Fig. 4.10f). The valley fill has a basal gravel lag, especially in the central part, and is

likely mixed with lateral contributions from hillslopes similar to modern conditions some 3-4 km upstream of our survey area (Fig. 4.10g). In general, we expect thicker colluvial deposits close to the hillslopes but also soil development in the middle of the valley (Fig. 4.10c and e), as also has been suggested in a study in a similar setting by Hirsch et al. (2008). The sediments overlying the gravel lag deposits have larger concentrations of fine materials related to a period that favoured soil accumulation and development. In the shallowest part, in contrast, we identified accumulations of several bar deposits such as the ones interpreted in Fig. 4.8a and visualised in Fig. 4.10b. The bar deposit at the far left flank has been reworked, forming channel-like structures (as observed in Fig. 4.10a) characterised by concave-up GPR reflectors and low conductivities.

To learn more about the history of this alluvial fan, direct exploration via boreholes that allow for centimetre-scale resolution of the stratigraphy and dating at different depth levels may be necessary. In this context, the fanhead area may be more informative than the distal alluvial fan, which is likely influenced by the trunk channel of the Kocher. In terms of hazard assessment, alluvial fan information may be complemented with other catchment processes like supply of sediments and their renewal development, as well as possible triggering factors such as rainfall thresholds (Bardou and Jaboyedoff, 2008; Schürch et al., 2016; Savi et al., 2014).

4.5 Conclusions

The 2016 flash floods in southern Germany have shown that this cuesta landscape with gentle relief is prone to rare ($>$ 100 years return period) but catastrophic episodes of erosion and sedimentation that rival those in mountain regions. Our study shows that events such as the May 2016 flash floods in northeastern Baden-Württemberg can be recorded in alluvial deposits of tributary fans. While outcrops are a valuable source of direct information to constrain past processes, such exposures are scarce, especially in aggrading rivers or those that have been subject to recent catastrophic sedimentation. Non-invasive geophysical surveying elucidates the sedimentary architecture and offers insights into the past dynamics of alluvial fan systems. For the Grimmbach fan, we inferred traces of two bars and former channel fills at shallow depths below the surface, as well as buried soils. Such characteristics indicate that the current channel has been incising, favouring stable floodplains and soil development interrupted only by sudden channel avulsions. Future sampling in the floodplain (e.g., using trenches) may focus on patches of intermediate conductivities and low GPR amplitudes, because these areas may be characterised by intercalated fine and coarse materials (e.g., overbank deposits) with sharp contacts indicative of different floods. The methods and workflow presented in this study might be followed to guide similar geophysical exploration of valley fills in the area. Stratigraphic information archived in alluvial fans may be useful in hazard models of extreme sediment transport, especially in areas with poor records of such events.

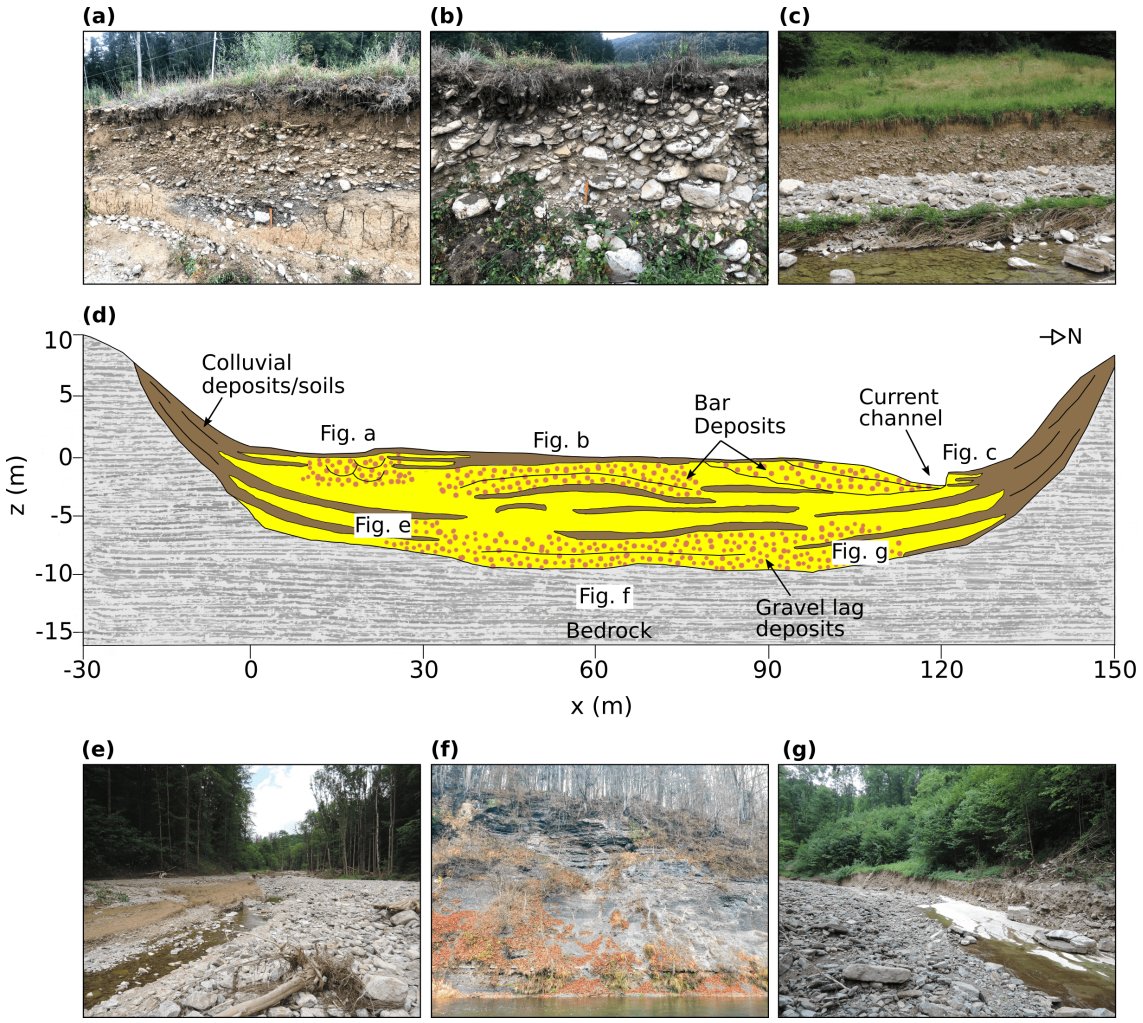

Fig. 4.10. Sedimentary architecture of the Grimmbach fan. (a) Channel fill structure found $\sim$ 500 m upstream of the Grimmbach-Kocher confluence. (b) Detail of the interpreted bar deposit of Fig. 4.8b. (c) Colluvial deposits are overlying channel-bed deposits $\sim$ 570 m upstream from the Grimmbach-Kocher confluence. (d) Inferred and idealised fan stratigraphy considering profiles ERT2, EMI1, GPR3, and available outcrops, where $x = 0$ m corresponds to the origin of the ERT2 profile and $x = 95$ m to its end. (e) Deposits of the last flood overlay a layer composed of fine materials in the middle reach of the Grimmbach (1-2 km upstream from our field site). (f) Outcrop of the bedrock on the left flank of the Kocher opposite the Grimmbach outlet. (g) Coarse material in the left flank and fine material to the right flank overlying bedrock in the upper reach of the Grimmbach (3-4 km upstream from our field site).

In summary, the hazard of extreme geomorphic and hydrologic processes (e.g., flash floods and debris flows) may have been underestimated in this southern German region, as demonstrated by the widespread damage to settlements of villages and towns in the alluvial fan areas. One lesson from the 2016 flash flood is the importance of low-permeable soils of the plateau tops that are mainly used for agriculture, promoting fast runoff and high amounts of soil erosion during major rainstorms. Both runoff and erosion created a dense flow of water and fine particles that mobilised coarser material and woody debris from channel banks and shallow landslides and deposited this material on downstream alluvial fans. Hence, we expect similar deposits on many of the small tributary fans in the greater region.

5

General discussion and conclusions

Many applications of the ERT method aim at imaging layers with rather sharp contacts or interfaces as illustrated in our field examples in Chapter 2 and Chapter 3. Local inversion methods based on smoothing and damping strategies usually fail to retrieve layered structures, resulting in smeared images of the subsurface. Common approaches to favor more layered structures during local inversions consist of weighting (at different levels) the horizontal and vertical gradients and using geostatistical regularization approaches. In the end, such approaches will always smear sharp interfaces. Therefore, a user-specified threshold or gradient-based edge detection algorithm might be used to interpret a plausible sharp boundary; however, its reliability highly depends on the accuracy of the inverted model. When prior information from outcrops, boreholes, and other geophysical methods suggests a layered subsurface, a practical strategy is to consider a layer-based model parameterization (LBMP) strategy.

In Chapter 2 and Chapter 3, we used a LBMP and a global inversion algorithm (PSO) to generate ensembles of inverted models associated with 2D ERT data acquired in a coastal aquifer and two subsea permafrost environments, respectively. In these examples, we demonstrated how such parameterization and inversion strategies helped to obtain plausible model solutions and the associated uncertainties around the found interfaces. In our synthetic (Section 2.3.1) and two permafrost examples (Section 3.5.1 and Section 3.5.2), we showed that using a parameterization relying on the arctangent function was helpful and allowed us to resolve abrupt changes along the subsurface interfaces. Furthermore, we demonstrated in our Dunkirk example (Section 2.3.2) that the arctangent function can also result in sub-horizontal interfaces. Overall, these examples illustrated the capabilities of the arctangent function to adapt to complex and simple subsurface scenarios, which is useful when we do not know the general shape of the subsurface interfaces. It is important to highlight that there are also other popular interface parameterization strategies, such as the ones relying on cubic spline interpolations (Koren et al., 1991) and Fourier coefficients (e.g., Roy et al., 2021). These strategies may be considered if preliminary information suggests that smoothed interfaces are expected. However, a comparative study in terms of the applicability (suitable scenarios) and performance (i.e., adaptability and development during inversion) of these parameterization strategies have not yet been performed. Finally, instead of using layers with homogeneous resistivities like in Chapter 2 and Chapter 3, we could also allow lateral variation to account for slight variations as suggested by Auken and Christiansen (2004) and Akça and Basokur (2010).

During the global inversion of our ERT data sets, we only considered the RMSLE as our objective function. However, other cost functions could be studied to infer their impact in the final inverted models (e.g., Barboza et al., 2018). To our knowledge, for example, comparing the results of L_1 and L_2 norms (or other objective functions) for inversion approaches based on LBMP has not yet been performed. In addition, one aspect we did not discuss in our manuscripts is that when we considered the logarithm of the resistivity, our inversion runs converged faster than when considering the resistivity on a linear scale. This highlights the logarithmic behavior of this physical property and the importance of its representation on a logarithmic scale.

Global evaluation of the residual (e.g., RMSE) may help to compare the performance across models, while residual analysis across pseudosection pixels is helpful to qualitatively infer which areas of the model fit the data the best or worst. Auken and Christiansen (2004) suggested that when using a LBMP strategy to invert 2D ERT data, we should seek the model with the minimum possible error to account for the reduced number of model parameters that cannot result in complex model solutions. They also indicate that this approach is not wanted for highly undetermined smooth inversion problems, which may result in huge overfitting. However, regardless of the inversion strategy, it is challenging to ensure if we are overfitting or underfitting the data. For example, our residual pseudosections in Chapter 3 showed that some areas were better fitted than others. This can be a compromise of the LBMP strategy, which is trying to fit most data points while likely overfitting and/or underfitting some areas of the model. This problem can be better addressed and understood by considering ensembles of model solutions. For example, when calculating the median model in an ensemble of models, the areas that could have been overfitted are smeared if they are not persistent across the ensemble of models. Additionally, the variability in each ensemble will indicate the persistence of the structures across the models and can be interpreted as model uncertainties.

Generating ensembles of 2D ERT model solutions with a global inversion algorithm is computationally expensive. Therefore, it might be helpful to perform several tests to learn about the impact of different hyperparameters (e.g., number of particles in PSO) or model parameters (e.g., number of layers and resistivity ranges). An alternative to learning and obtaining important hints about model parameter ranges and trade-offs is using a 1D global inversion approach, which is significantly faster than 2D global inversions. However, we should be aware that 1D and 2D inversions can result in partially different models at the same considered vertical profile. Therefore, as we already pointed out in Chapter 3, the success and feasibility of 1D inversion results rather depend on the characteristics of the field site and analyzed data set. Additionally, we could also take advantage of the fast convergence rates of the local inversion approaches for obtaining a general idea about a plausible subsurface structure and resistivity distributions (e.g., Fernández-Martínez et al., 2017).

As illustrated in Chapter 2 and Chapter 3, a global inversion algorithm does not ensure

convergence into a global minimum. Therefore, the model solutions may be characterized by ensembles or families of equivalent model solutions (i.e., similar structures and misfit values). To group equivalent model solutions, we used a k-means algorithm. However, before performing cluster analysis, in Chapter 2, we proposed a model selection criteria where we first choose the models with better misfits and then perform cluster analysis. Another practical approach that we could have evaluated is first to perform cluster analysis and, after analyzing misfit distributions, remove the non-converged models from each cluster. In our clustering strategy, we consider not only the model resistivities but also their corresponding data residuals and, thus, ensure models that fit the data in a similar fashion. In addition, it might be interesting to test the impact of including the first principal components (i.e., after principal component analysis) of each model as an additional input parameter in the clustering strategy. An additional aspect that can be considered when performing cluster analysis of ERT models is to account for resolution loss with depth; for example, by weighting the model parameters and data by considering the sensitivity matrix and the geometrical factors, respectively.

A critical parameter in most clustering techniques is to define an optimum number of clusters or families. To address this problem, several indexes like the variance ratio criterion (Caliński and Harabasz, 1974) can provide a good reference for the expected number of families. However, we should always be careful with such indexes and try to visualize scenarios considering also different numbers of families. Although in this thesis we only consider the k-means algorithm to group equivalent models, evaluating and comparing the performance of other clustering strategies like spectral or agglomerative clustering approaches might be beneficial to guide future studies considering ensembles of ERT model solutions.

It is important to highlight that the statistical descriptors chosen to summarize the information within each cluster of models have an impact on the resulting model. For example, to evaluate the central trend model the mean model can result in smeared interfaces because it is highly influenced by the resistivity values falling at the extremes of the considered resistivity distributions. In contrast, median models are less affected by the values in the tails of resistivity distributions and result in sharper models than the mean models.

There may be complex geological scenarios where LBMP may be unsuitable or require more complex adaptations. Such scenarios can be, for example, subsurface models with short wavelength structures like karstic and alluvial systems (e.g., Hermans and Irving, 2017; Barboza et al., 2019). For example, in Chapter 4, we applied the workflow of Chapter 2 to invert our ERT data sets from Grimmbach. However, models usually converged to a local minimum with large misfit values and unrealistic solutions (note that such results are not shown in this thesis). Therefore, geostatistical regularizations, which are broadly used to investigate alluvial sediments (Irving and Singha, 2010), were adopted instead and yielded models more consistent with our geological understanding of the studied area. One interesting approach to broadly explore the space of solutions could be to combine geostatistical regularizations and a global

inversion approach. Additionally, a zonal parameterization approach could also allow for deriving sharp layers and might be more suitable when dealing with more complex subsurface scenarios (Paasche and Tronicke, 2007; Herman and Usher, 2017).

In Chapter 3, we showed how sensitivity analyses provide additional model understanding. In addition, we noted that 2D local sensitivity analyses presented some differences from 1D global sensitivity analyses. For example, while the 2D local sensitivity analyses in Chapter 3 indicated no sensitivity within the frozen sediments, the 1D global sensitivity analyses showed some sensitivity associated with the frozen layer. However, to have a more explicit and clear comparison, it might be interesting to assess 2D global sensitivities and, thus, explore the sensitivities associated with different regions of the cost function topography. Additionally, performing sensitivity analysis before a field campaign (e.g., considering conceptual subsurface models) may help to anticipate logistics aspects like defining an appropriated array configuration.

In summary, the ERT method is a powerful tool and can offer significant understanding in different terrestrial and aquatic environments. Many applications of the ERT method are usually performed in layered environments. In such cases, considering LBMP may be more revealing than traditional cell-based model parameterizations. Additionally, by obtaining several solutions to the ERT inverse problem using a LBMP approach and performing summary statistics, it is possible to derive representative or equivalent model solutions with their associated uncertainties. We could use such results to propagate the uncertainties associated with the position of the found interfaces to report, for example, the area of a specific layer (e.g., the 2D section of a sediment fill). On the other hand, uncertainties associated with resistivity may be considered for petrophysical translation. To reduce uncertainties related to the non-uniqueness of the inverse problem, we should consider all available and reliable information (e.g., known depths to interfaces by boreholes) to constrain model parameters. This way, we can guide the inversion towards more realistic model solutions. Although the strategies presented in this thesis focused on 2D ERT data to investigate layered environments, they are general and might be adapted to investigate other environments and to solve the inverse problem of other kinds of geophysical data sets such as those obtained from seismic, gravity, magnetic, and electromagnetic surveys. In addition, global inversion strategies offer enormous flexibility to perform the inversion of individual data sets, which could also be advantageous for performing more advanced inversion strategies like joint inversions.

Bibliography

Akça, I. and Basokur, A. T. (2010). Extraction of structure-based geoelectric models by hybrid genetic algorithms. *Geophysics*, 75(1):F15–F22.

Aleardi, M., Vinciguerra, A., and Hojat, A. (2021a). A geostatistical Markov chain Monte Carlo inversion algorithm for electrical resistivity tomography. *Near Surface Geophysics*, 19(1):7–26.

Aleardi, M., Vinciguerra, A., and Hojat, A. (2021b). Ensemble-based electrical resistivity tomography with data and model space compression. *Pure and Applied Geophysics*, 178(5):1781–1803.

Allroggen, N. and Tronicke, J. (2016). Attribute-based analysis of time-lapse ground-penetrating radar data. *Geophysics*, 81(1):H1–H8.

Angelopoulos, M. (2022). Mapping subsea permafrost with electrical resistivity surveys. *Nature Reviews Earth & Environment*, 3(1):6.

Angelopoulos, M., Overduin, P. P., Jenrich, M., Nitze, I., Günther, F., Strauss, J., Westermann, S., Schirrmeister, L., Kholodov, A., Krautblatter, M., Grigoriev, M. N., and Grosse, G. (2021). Onshore Thermokarst Primes Subsea Permafrost Degradation. *Geophysical Research Letters*, 48:e2021GL093881.

Angelopoulos, M., Overduin, P. P., Miesner, F., Grigoriev, M. N., and Vasiliev, A. A. (2020a). Recent advances in the study of Arctic submarine permafrost. *Permafrost and Periglacial Processes*, 31(3):442–453.

Angelopoulos, M., Overduin, P. P., Westermann, S., Tronicke, J., Strauss, J., Schirrmeister, L., Biskaborn, B. K., Liebner, S., Maksimov, G., Grigoriev, M. N., and Grosse, G. (2020b). Thermokarst Lake to Lagoon Transitions in Eastern Siberia: Do Submerged Taliks Refreeze? *Journal of Geophysical Research: Earth Surface*, 125(10):e2019JF005424.

Angelopoulos, M., Westermann, S., Overduin, P. P., Faguet, A., Olenchenko, V., Grosse, G., and Grigoriev, M. N. (2019). Heat and Salt Flow in Subsea Permafrost Modeled with CryoGRID2. *Journal of Geophysical Research: Earth Surface*, 124(4):920–937.

Arboleda-Zapata, M., Angelopoulos, M., Overduin, P. P., Grosse, G., Jones, M., and Tronicke, J. (2022a). Exploring the capabilities of electrical resistivity tomography to study subsea permafrost. *The Cryosphere*, 16:4423–4445.

Arboleda-Zapata, M., Guillemoteau, J., and Tronicke, J. (2022b). A comprehensive workflow to analyze ensembles of globally inverted 2D electrical resistivity models. *Journal of Applied Geophysics*, 196(January):104512.

Are, F. (2003). Shoreface of the Arctic seas - A natural laboratory for subsea permafrost dynamics. In Philips, M. and Springman, S. M., editors, *Proceedings of the 8th International Conference on Permafrost*, pages 27–38. Balkema, Lisse, Netherlands.

Aster, R. C., Borchers, B., and Thurber, C. H. (2013). *Parameter estimation and inverse problems*. Elsevier.

Auken, E. and Christiansen, A. V. (2004). Layered and laterally constrained 2D inversion of resistivity data. *Geophysics*, 69(3):752–761.

Auken, E., Christiansen, A. V., Jacobsen, B. H., Foged, N., and Sørensen, K. I. (2005). Piecewise 1D laterally constrained inversion of resistivity data. *Geophysical Prospecting*, 53:497–506.

Baines, D., Smith, D. G., Froese, D. G., Bauman, P., and Nimeck, G. (2002). Electrical resistivity ground imaging (ERGI): A new tool for mapping the lithology and geometry of channel-belts and valley-fills. *Sedimentology*, 49(3):441–449.

Barboza, F. M., Medeiros, W. E., and Santana, J. M. (2018). Customizing constraint incorporation in direct current resistivity inverse problems: A comparison among three global optimization methods. *Geophysics*, 83(6):E409–E422.

Barboza, F. M., Medeiros, W. E., and Santana, J. M. (2019). A user-driven feedback approach for 2D direct current resistivity inversion based on particle swarm optimization. *Geophysics*, 84(2):E105–E124.

Bardou, E. and Jaboyedoff, M. (2008). Debris flows as a factor of hillslope evolution controlled by a continuous or a pulse process? In Gallagher, K., Jones, J., and Wainwright, J., editors, *Landscape evolution: Denudation, climate and tectonics over different time and space scales*, volume 296, pages 63–78. Geological Sociaty of London.

Barnhart, K. R., Anderson, R. S., Overeem, I., Wobus, C., Clow, G. D., and Urban, F. E. (2014). Modeling erosion of ice-rich permafrost bluffs along the Alaskan Beaufort Sea coast. *Journal of Geophysical Research: Earth Surface*, 119(5):1155–1179.

Bazin, S. and Pfaffhuber, A. A. (2013). Mapping of quick clay by electrical resistivity tomography under structural constraint. *Journal of Applied Geophysics*, 98:280–287.

Beauvais, A., Ritz, M., Parisot, J. C., Bantsimba, C., and Dukhan, M. (2004). Combined ERT and GPR methods for investigating two-stepped lateritic weathering systems. *Geoderma*, 119(1-2):121–132.

Befus, K. M., Cardenas, M. B., Tait, D. R., and Erler, D. V. (2014). Geoelectrical signals of geologic and hydrologic processes in a fringing reef lagoon setting. *Journal of Hydrology*, 517:508–520.

Bergmann, P., Ivandic, M., Norden, B., Rücker, C., Kiessling, D., Lüth, S., Schmidt-Hattenberger, C., and Juhlin, C. (2014). Case history: Combination of seismic reflection and constrained resistivity inversion with an application to 4D imaging of the CO2 storage site, Ketzin, Germany. *Geophysics*, 79(2):B37–B50.

Black, R. F. (1964). Gubik formation of Quaternary age in northern Alaska. Technical report, US Government Printing Office.

Boiero, D. and Socco, L. V. (2014). Joint inversion of Rayleigh-wave dispersion and P-wave refraction data for laterally varying layered models. *Geophysics*, 79(4):EN49–EN59.

Böniger, U. and Tronicke, J. (2010). On the potential of kinematic GPR surveying using a self-tracking total station: Evaluating system crosstalk and latency. *IEEE Transactions on Geoscience and Remote Sensing*, 48(10):3792–3798.

Brardinoni, F., Picotti, V., Maraio, S., Bruno, P. P., Cucato, M., Morelli, C., and Mair, V. (2018). Postglacial evolution of a formerly glaciated valley: Reconstructing sediment supply, fan building, and confluence effects at the millennial time scale. *Bulletin of the Geological Society of America*, 130(9-10):1457–1473.

Bristol, E. M., Connolly, C. T., Lorenson, T. D., Richmond, B. M., Ilgen, A. G., Choens, R. C., Bull, D. L., Kanevskiy, M., Iwahana, G., Jones, B. M., and McClelland, J. W. (2021). Geochemistry of Coastal Permafrost and Erosion-Driven Organic Matter Fluxes to the Beaufort Sea Near Drew Point, Alaska. *Frontiers in Earth Science*, 8:598933.

Bronstert, A., Agarwal, A., Boessenkool, B., Crisologo, I., Fischer, M., Heistermann, M., Köhn-Reich, L., López-Tarazón, J. A., Moran, T., Ozturk, U., Reinhardt-Imjela, C., and Wendi, D. (2018). Forensic hydro-meteorological analysis of an extreme flash flood: The 2016-05-29 event in Braunsbach, SW Germany. *Science of the Total Environment*, 630:977–991.

Brothers, L. L., Herman, B. M., Hart, Patrick, E., and Ruppel, Carolyn, D. (2016). Subsea ice-bearing permafrost on the U.S. Beaufort Margin: 1. Minimum seaward extent defined from multichannel seismic reflection data. *Geochemistry, Geophysics, Geosystems*, 17:4354–4365.

Bruni, E. T., Ott, R. F., Picotti, V., Haghipour, N., Wegmann, K. W., and Gallen, S. F. (2021). Stochastic alluvial fan and terrace formation triggered by a high-magnitude Holocene landslide in the Klados Gorge, Crete. *Earth Surface Dynamics*, 9(4):771–793.

Bull, D. L., Bristol, E. M., E. Brown, R. C. Choens, C. T. Connolly, C.Flanary, Frederick, J. M. M., Jones, B. M., C.A.Jones, M.Ward Jones, McClelland, J. W., A. Mota, and I. Tezaur (2020). Arctic Coastal Erosion : Modeling and Experimentation (No. SAND2020-10223). Technical report, Sandia National Labs. (SNL-NM), Alburqueque, NM (United States); Sandia National Lab. (SNL-CA), Livermore, CA (United States).

Caliński, T. and Harabasz, J. (1974). A dendrite method for cluster analysis. *Communications in Statistics-theory and Methods*, 3(1):1–27.

Caterina, D., Hermans, T., and Nguyen, F. (2014). Case studies of incorporation of prior information in electrical resistivity tomography: Comparison of different approaches. *Near Surface Geophysics*, 12(4):451–465.

Chambers, J. E., Wilkinson, P. B., Wardrop, D., Hameed, A., Hill, I., Jeffrey, C., Loke, M. H., Meldrum, P. I., Kuras, O., Cave, M., and Gunn, D. A. (2012). Bedrock detection beneath river terrace deposits using three-dimensional electrical resistivity tomography. *Geomorphology*, 177-178:17–25.

Clair, J. S., Moon, S., Holbrook, W. S., Perron, J. T., Riebe, C. S., Martel, S. J., Carr, B., Harman, C., Singha, K., De Richter, D. B., St Clair, J., Moon, S., Holbrook, W. S., Perron, J. T., Riebe, C. S., Martel, S. J., Carr, B., Harman, C., Singha, K., deB Richter, D., Clair, J. S., Moon, S., Holbrook, W. S., Perron, J. T., Riebe, C. S., Martel, S. J., Carr, B., Harman, C., Singha, K., and De Richter, D. B. (2015). Geophysical imaging reveals topographic stress control of bedrock weathering. *Science*, 350(6260):534–538.

Constable, S., Orange, A., and Key, K. (2015). And the geophysicist replied: "Which model do you want?". *Geophysics*, 80(3):E197–E212.

Cordua, K. S., Hansen, T. M., and Mosegaard, K. (2012). Monte Carlo full-waveform inversion of crosshole GPR data using multiple-point geostatistical a priori information. *Geophysics*, 77(2):H19–H31.

Coscia, I., Greenhalgh, S. A., Linde, N., Doetsch, J., Marescot, L., Günther, T., Vogt, T., and Green, A. G. (2011). 3D crosshole ERT for aquifer characterization and monitoring of infiltrating river water. *Geophysics*, 76(2).

Crawford, M. M., Zhu, J., and Webb, S. E. (2015). Geologic, geotechnical, and geophysical investigation of a shallow landslide, eastern Kentucky. *Environmental and Engineering Geoscience*, 21(3):181–195.

Crosta, G. B. and Frattini, P. (2004). Controls on modern alluvial fan processes in the Central Alps, Northern Italy. *Earth Surface Processes and Landforms*, 29(3):267–293.

Dahlin, T. (2001). The development of DC resistivity imaging techniques. *Computers & Geosciences*, 27:1019–1029.

Dahlin, T. and Zhou, B. (2004). A numerical comparison of 2D resistivity imaging with 10 electrode arrays. *Geophysical Prospecting*, 52:379–398.

Davies, T. and Korup, O. (2007). Persistent alluvial fanhead trenching resulting from large, infrequent sediment inputs. *Earth Surface Processes and Landforms*, 32:725–742.

Day-Lewis, F. D., Singha, K., and Binley, A. M. (2005). Applying petrophysical models to radar travel time and electrical resistivity tomograms: Resolution-dependent limitations. *Journal of Geophysical Research: Solid Earth*, 110(8):B08206.

Day-Lewis, F. D., White, E. A., Johnson, C. D., Lane, J. W., and Belaval, M. (2006). Continuous resistivity profiling to delineate submarine groundwater discharge - Examples and limitations. *Leading Edge (Tulsa, OK)*, 25(6):724–728.

de Groot-Hedlin, C. D. and Vernon, F. L. (1998). An evolutionary programming method for estimating layered velocity structure. *Bulletin of the Seismological Society of America*, 88(4):1023–1035.

de Haas, T., Densmore, A. L., den Hond, T., and Cox, N. J. (2019). Fan-Surface Evidence for Debris-Flow Avulsion Controls and Probabilities, Saline Valley, California. *Journal of Geophysical Research: Earth Surface*, 124(5):1118–1138.

De Pasquale, G., Linde, N., Doetsch, J., and Holbrook, W. S. (2019). Probabilistic inference of subsurface heterogeneity and interface geometry using geophysical data. *Geophysical Journal International*, 217(2):816–831.

Dietrich, A. and Krautblatter, M. (2017). Evidence for enhanced debris-flow activity in the Northern Calcareous Alps since the 1980s (Plansee, Austria). *Geomorphology*, 287:144–158.

Doetsch, J., Linde, N., Pessognelli, M., Green, A. G., and Günther, T. (2012). Constraining 3-D electrical resistance tomography with GPR reflection data for improved aquifer characterization. *Journal of Applied Geophysics*, 78:68–76.

Douma, H. and Haney, M. (2013). Exploring nonlinearity and nonuniqueness in surface-wave inversion for near-surface velocity estimation. *The Leading Edge*, 32(6):648–655.

Douma, H., Snieder, R., and Lomax, A. (1996). Ensemble inference in terms of empirical orthogonal functions. *Geophysical Journal International*, 127(2):363–378.

Ékes, C. and Hickin, E. J. (2001). Ground penetrating radar facies of the paraglacial Cheekye Fan, Southwestern British Columbia, Canada. *Sedimentary Geology*, 143(3-4):199–217.

Everett, M. E. (2013). *Near-Surface Applied Geophysics*. Cambridge University Press.

Fernández-Martínez, J. L. (2015). Model reduction and uncertainty analysis in inverse problems. *Leading Edge*, 34(9):1006–1016.

Fernández-Martínez, J. L., Fernández Muñiz, M. Z., and Tompkins, M. J. (2012). On the topography of the cost functional in linear and nonlinear inverse problems. *Geophysics*, 77(1):w1–w15.

Fernández-Martínez, J. L., García Gonzalo, E., Fernández Álvarez, J. P., Kuzma, H. A., and Menéndez Pérez, C. O. (2010). PSO: A powerful algorithm to solve geophysical inverse problems Application to a 1D-DC resistivity case. *Journal of Applied Geophysics*, 71(1):13–25.

Fernández-Martínez, J. L., Xu, S., Sirieix, C., Fernández-Muniz, Z., and Riss, J. (2017). Uncertainty analysis and probabilistic segmentation of electrical resistivity images: the 2D inverse problem. *Geophysical Prospecting*, 65:112–130.

Fortier, R., Allard, M., and Seguin, M. K. (1994). Effect of physical properties of frozen ground on electrical resistivity logging. *Cold Regions Science and Technology*, 22(4):361–384.

Franke, D., Hornung, J., and Hinderer, M. (2015). A combined study of radar facies, lithofacies and three-dimensional architecture of an alpine alluvial fan (Illgraben fan, Switzerland). *Sedimentology*, 62(1):57–86.

Frederick, J. M. and Buffett, B. A. (2015). Effects of submarine groundwater discharge on the present-day extent of relict submarine permafrost and gas hydrate stability on the Beaufort Sea continental shelf. *Journal of Geophysical Research: Earth Surface*, 120(3):417–432.

Fuchs, M., Palmtag, J., Juhls, B., Overduin, P. P., Grosse, G., Abdelwahab, A., Bedington, M., Sanders, T., Ogneva, O., Fedorova, I. V., Zimov, N. S., Mann, P. J., and Strauss, J. (2022). High-resolution bathymetry models for the Lena Delta and Kolyma Gulf coastal zones. *Earth System Science Data Discussions*, 14:2279–2301.

Furman, A., Ferre, T. P. A., and Warrick, A. W. (2003). A Sensitivity Analysis of Electrical Resistivity Tomography Array Types Using Analytical Element Modeling. *Vadose Zone Journal*, 2(3):416–423.

Garré, S., Günther, T., Diels, J., and Vanderborght, J. (2012). Evaluating experimental design of ERT for soil moisture monitoring in contour Hedgerow intercropping systems. *Vadose Zone Journal*, 11(4):vzj2011.0186.

Gebrande, H. (1976). A seismic-ray tracing method for two dimensional inhomogeneous media. In *Explosion seismology in Central Europe: data and results*, pages 162–167. Springer-Verlag, New York.

Gelhar, L. W. (1993). *Stochastic subsurface hydrology*. Prentice-Hall, Inc.

Giao, P. H., Weller, A., Hien, D. H., and Adisornsupawat, K. (2008). An approach to construct the weathering profile in a hilly granitic terrain based on electrical imaging. *Journal of Applied Geophysics*, 65:30–38.

Gonzales Amaya, A., Ortiz, J., Durán, A., and Villazon, M. (2019). Hydrogeophysical methods and hydrogeological models: basis for groundwater sustainable management in Valle Alto (Bolivia). *Sustainable Water Resources Management*, 5(3):1179–1188.

Gourry, J. C., Vermeersch, F., Garcin, M., and Giot, D. (2003). Contribution of geophysics to the study of alluvial deposits: A case study in the Val d'Avaray area of the River Loire, France. *Journal of Applied Geophysics*, 54(1-2):35–49.

Grana, D., Passos De Figueiredo, L., and Azevedo, L. (2019). Uncertainty quantification in Bayesian inverse problems with model and data dimension reduction. *Geophysics*, 84(6):M15–M24.

Grigoriev, M. N. (2008). *Kriomorfogenez i litodinamika pribrezhno- shelfovoi zony morei Vostochnoi Sibiri (Cryomorphogenesis and lithodynamics of the East Siberian near-shore shelf zone)*. PhD thesis, Melnikov Permafrost Institute, Russian Academy of Sciences, Siberian Branch, Yakutsk.

Grosse, G., Schirrmeister, L., Siegert, C., Kunitsky, V. V., Slagoda, E. A., Andreev, A. A., and Dereviagyn, A. Y. (2007). Geological and geomorphological evolution of a sedimentary periglacial landscape in Northeast Siberia during the Late Quaternary. *Geomorphology*, 86(1-2):25–51.

Guillemoteau, J., Christensen, N. B., Jacobsen, B. H., and Tronicke, J. (2017). Fast 3D multichannel deconvolution of electromagnetic induction loop-loop apparent conductivity data sets acquired at low induction numbers. *Geophysics*, 82(6):E357–E369.

Guillemoteau, J. and Tronicke, J. (2016). Evaluation of a rapid hybrid spectral-spatial domain 3D forward-modeling approach for loop-loop electromagnetic induction quadrature data acquired in low-induction-number environments. *Geophysics*, 81(6):E447–E458.

Günther, T., Rücker, C., and Spitzer, K. (2006). Three-dimensional modelling and inversion of dc resistivity data incorporating topography – II. Inversion. *Geophys. J. Int*, 166(2):506–517.

Harrison, W. D. and Osterkamp, T. E. (1978). Heat and mass transport processes in subsea permafrost 1. An analysis of molecular diffusion and its consequences. *Journal of Geophysical Research*, 83(C9):4707–4712.

Harvey, A. (2012). The coupling status of alluvial fans and debris cones: A review and synthesis. *Earth Surface Processes and Landforms*, 37(1):64–76.

Herman, J. and Usher, W. (2017). SALib: an open-source Python library for sensitivity analysis. *Journal of Open Source Software*, 2(9):97.

Hermans, T. and Irving, J. (2017). Facies discrimination with electrical resistivity tomography using a probabilistic methodology: Effect of sensitivity and regularization. *Near Surface Geophysics*, 15:13–25.

Hermans, T., Nguyen, F. F., and Caers, J. (2015). Uncertainty in training image-based inversion of hydraulic head data constrained to ERT data: Workflow and case study. *Water Resources Research*, 51(7):5332–5352.

Hermans, T. and Paepen, M. (2020). Combined inversion of land and marine electrical resistivity tomography for submarine groundwater discharge and saltwater intrusion characterization. *Geophysical Research Letters*, 47(3):e2019GL085877.

Hickin, A. S., Kerr, B., Barchyn, T. E., and Paulen, R. C. (2009). Using ground-penetrating radar and capacitively coupled resistivity to investigate 3-D fluvial architecture and grain-size distribution of a gravel floodplain in northeast British Columbia, Canada. *Journal of Sedimentary Research*, 79(6):457–477.

Hilbich, C., Hauck, C., Mollaret, C., Wainstein, P., and Arenson, L. U. (2022). Towards accurate quantification of ice content in permafrost of the Central Andes-Part 1: Geophysics-based estimates from three different regions. *The Cryosphere*, 16:1845–1872.

Hirsch, M., Bentley, L. R., and Dietrich, P. (2008). A comparison of electrical resistivity, ground penetrating radar and seismic refraction results at a river terrace site. *Journal of Environmental and Engineering Geophysics*, 13(4):325–333.

Hoffmann, R. and Dietrich, P. (2004). An approach to determine equivalent solutions to the geoelectrical 2D inversion problem. *Journal of Applied Geophysics*, 56(2):79–91.

Hornung, J., Pflanz, D., Hechler, A., Beer, A., Hinderer, M., Maisch, M., and Bieg, U. (2010). 3-D architecture, depositional patterns and climate triggered sediment fluxes of an alpine alluvial fan (Samedan, Switzerland). *Geomorphology*, 115(3-4):202–214.

Houthuys, R., De Moor, G., and Somme, J. (1993). Shaping of the French-Belgian North Sea Coast throughout recent geology and history. *Coastal Zone: Proceedings of the Symposium on Coastal and Ocean Management*, pages 27–40.

Hsu, H. L., Yanites, B. J., Chen, C. c., Chen, Y. G., chih Chen, C., Chen, Y. G., Chen, C. c., and Chen, Y. G. (2010). Bedrock detection using 2D electrical resistivity imaging along the Peikang River, central Taiwan. *Geomorphology*, 114(3):406–414.

Hubbard, S. S., Gangodagamage, C., Dafflon, B., Wainwright, H., Peterson, J., Gusmeroli, A., Ulrich, C., Wu, Y., Wilson, C., Rowland, J., Tweedie, C., and Wullschleger, S. D. (2013). Quantifying and relating land-surface and subsurface variability in permafrost environments using LiDAR and surface geophysical datasets. *Hydrogeology Journal*, 21(1):149–169.

Irving, J. and Singha, K. (2010). Stochastic inversion of tracer test and electrical geophysical data to estimate hydraulic conductivities. *Water Resources Research*, 46(11):W11514.

Jones, B. M., Arp, C. D., Jorgenson, M. T., Hinkel, K. M., Schmutz, J. A., and Flint, P. L. (2009). Increase in the rate and uniformity of coastline erosion in Arctic Alaska. *Geophysical Research Letters*, 36(3):L03503.

Jones, B. M., Farquharson, L. M., Baughman, C. A., Buzard, R. M., Arp, C. D., Grosse, G., Bull, D. L., Günther, F., Nitze, I., Urban, F., Kasper, J. L., Frederick, J. M., Thomas, M., Jones, C., Mota, A., Dallimore, S., Tweedie, C., Maio, C., Mann, D. H., Richmond, B., Gibbs, A., Xiao, M., Sachs, T., Iwahana, G., Kanevskiy, M., and Romanovsky, V. E. (2018). A decade of remotely sensed observations highlight complex processes linked to coastal permafrost bluff erosion in the Arctic. *Environmental Research Letters*, 13(11):115001.

Jones, B. M., Hinkel, K. M., Arp, C. D., and Eisner, W. R. (2008). Modern erosion rates and loss of coastal features and sites, Beaufort Sea coastline, Alaska. *Arctic*, 61(4):361–372.

Jordi, C., Doetsch, J., Günther, T., Schmelzbach, C., and Robertsson, J. O. A. (2018). Geostatistical regularization operators for geophysical inverse problems on irregular meshes. *Geophysical Journal International*, 213(2):1374–1386.

Juhojuntti, N. and Kamm, J. (2015). Joint inversion of seismic refraction and resistivity data using layered models-applications to groundwater investigation. *Geophysics*, 80(1):EN43–EN55.

Kang, M. and Lee, J. S. (2015). Evaluation of the freezing-thawing effect in sand-silt mixtures using elastic waves and electrical resistivity. *Cold Regions Science and Technology*, 113:1–11.

Kennedy, J. and Eberhart, R. (1995). Particle swarm optimization. In *Proceedings of the IEEE International Joint Conference on Neural Networks*, pages 1942–1948.

Klingler, S., Leven, C., Cirpka, O. A., and Dietrich, P. (2020). Anomaly effect-driven optimization of direct-current geoelectric mapping surveys in large areas. *Journal of Applied Geophysics*, 176:104002.

Klose, T., Guillemoteau, J., Vignoli, G., and Tronicke, J. (2022). Laterally constrained inversion (LCI) of multi-configuration EMI data with tunable sharpness. *Journal of Applied Geophysics*, 196(January):104519.

Kneisel, C., Hauck, C., Fortier, R., and Brian, M. (2008). Advances in geophysical methods for permafrost investigations. *Permafrost and Periglacial Processes*, 19:157–178.

Koren, Z., Mosegaard, K., Landa, E., Thore, P., and Tarantola, A. (1991). Monte Carlo estimation and resolution analysis of seismic background velocities.

Korup, O. (2004). Landslide-induced river channel avulsions in mountain catchments of southwest New Zealand. *Geomorphology*, 63(1-2):57–80.

Lantuit, H., Atkinson, D., Overduin, P. P., Grigoriev, M., Rachold, V., Grosse, G., and Hubberten, H. W. (2011). Coastal erosion dynamics on the permafrost-dominated Bykovsky Peninsula, north Siberia, 1951-2006. *Polar Research*, 30(1):7341.

Loke, M. H., Acworth, I., and Dahlin, T. (2003). A comparison of smooth and blocky inversion methods in 2D electrical imaging surveys. *Exploration Geophysics*, 34:182–187.

Loke, M. H. and Barker, R. D. (1996). Rapid least-squares inversion of apparent resistivity pseudosections by a quasi-Newton method. *Geophysical Prospecting*, 44(1):131–152.

Loke, M. H., Chambers, J. E., Rucker, D. F., Kuras, O., and Wilkinson, P. B. (2013). Recent developments in the direct-current geoelectrical imaging method. *Journal of Applied Geophysics*, 95:135–156.

Lomax, A. and Snieder, R. (1995). Identifying sets of acceptable solutions to non-linear, geophysical inverse problems which have complicated misfit functions. *Nonlinear Processes in Geophysics*, 2(3/4):222–227.

Lucía, A., Schwientek, M., Eberle, J., and Zarfl, C. (2018). Planform changes and large wood dynamics in two torrents during a severe flash flood in Braunsbach, Germany 2016. *Science of the Total Environment*, 640-641:315–326.

Lück, A. (2020). *Subsea permafrost degradation and coastline retreat at Drew Point (Alaska)*. Master Thesis, University of Potsdam, Potsdam, Germany.

MacQueen, J. (1967). Some methods for classification and analysis of multivariate observations. In *Proceedings of the fifth Berkeley symposium on mathematical statistics and probability*, pages 281–297.

Malinverno, A. (2002). Parsimonious Bayesian Markov chain Monte Carlo inversion in a nonlinear geophysical problem. *Geophysical Journal International*, 151(3):675–688.

Mather, A. E., Stokes, M., and Whitfield, E. (2017). River terraces and alluvial fans: The case for an integrated Quaternary fluvial archive. *Quaternary Science Reviews*, 166:74–90.

McNeill, J. D. (1980). Electromagnetic terrain conductivity measurement at low induction numbers. Technical Report TN–6, Geonics Ltd.

Nickschick, T., Flechsig, C., Mrlina, J., Oppermann, F., Löbig, F., and Günther, T. (2019). Large-scale electrical resistivity tomography in the Cheb Basin (Eger Rift) at an International Continental Drilling Program (ICDP) monitoring site to image fluid-related structures. *Solid Earth*, 10(6):1951–1969.

Olayinka, A. I. and Yaramanci, U. (2000). Use of block inversion in the 2-D interpretation of apparent resistivity data and its comparison with smooth inversion. *Journal of Applied Geophysics*, 45(2):63–81.

Oldenburg, D. W. and Li, Y. (1999). Estimating depth of investigation in DC resistivity and IP surveys. *Geophysics*, 64(2):403–416.

Osterkamp, T. E. (2001). Sub-sea Permafrost. In *Encyclopedia of Ocean Sciences*, pages 2902–2912. Academic Press, New York, and London.

Overduin, P. P., Haberland, C., Ryberg, T., Kneier, F., Jacobi, T., Grigoriev, M. N., and Ohrnberger, M. (2015a). Submarine permafrost depth from ambient seismic noise. *Geophysical Research Letters*, 42(18):7581–7588.

Overduin, P. P., Liebner, S., Knoblauch, C., Günther, F., Wetterich, S., Schirrmeister, L., Hubberten, H.-W., and Grigoriev, M. N. (2015b). Methane oxidation following submarine permafrost degradation: Measurements from a central Laptev Sea shelf borehole. *Journal of Geophysical Research: Biogeosciences*, 120:965–978.

Overduin, P. P., Westermann, S., Yoshikawa, K., Haberlau, T., Romanovsky, V., and Wetterich, S. (2012). Geoelectric observations of the degradation of nearshore submarine permafrost at Barrow (Alaskan Beaufort Sea). *Journal of Geophysical Research: Earth Surface*, 117(2):F02004.

Overduin, P. P., Wetterich, S., Günther, F., Grigoriev, M. N., Grosse, G., Schirrmeister, L., Hubberten, H. W., and Makarov, A. (2016). Coastal dynamics and submarine permafrost in shallow water of the central Laptev Sea, East Siberia. *The Cryosphere*, 10(4):1449–1462.

Ozturk, U., Wendi, D., Crisologo, I., Riemer, A., Agarwal, A., Vogel, K., López-Tarazón, J. A., and Korup, O. (2018). Rare flash floods and debris flows in southern Germany. *Science of the Total Environment*, 626:941–952.

O'Neill, H. B., Roy-Leveillee, P., Lebedeva, L., Ling, F., O'Neill, H. B., Roy-Leveillee, P., Lebedeva, L., Ling, F., O'Neill, H. B., Roy-Leveillee, P., Lebedeva, L., and Ling, F. (2020). Recent advances (2010–2019) in the study of taliks. *Permafrost and Periglacial Processes*, 31(3):346–357.

Paasche, H. and Tronicke, J. (2007). Cooperative inversion of 2D geophysical data sets: A zonal approach based on fuzzy c-means cluster analysis. *Geophysics*, 72(3):35–39.

Pearson, C., Murphy, J., and Hermes, R. (1986). Acoustic and resistivity measurements on rock samples containing tetrahydrofuran hydrates: Laboratory analogues to natural gas hydrate deposits. *Journal of Geophysical Research*, 91(B14):14132–14138.

Pedrazas, M. N., Bayani Cardenas, M., Demir, C., Watson, J. A., Connolly, C. T., and McClelland, J. W. (2020). Absence of ice-bonded permafrost beneath an Arctic lagoon revealed by electrical geophysics. *Science Advances*, 6(43):eabb5083.

Permafrost Subcommittee (1988). *Glossary of permafrost and related ground-ice terms*. Associate Committee on Geotechnical Research, National Research Council of Canada, Ottawa.

Ping, C. L., Michaelson, G. J., Guo, L., Jorgenson, M. T., Kanevskiy, M., Shur, Y., Dou, F., and Liang, J. (2011). Soil carbon and material fluxes across the eroding Alaska Beaufort Sea coastline. *Journal of Geophysical Research: Biogeosciences*, 116:G02004.

Ramirez, A. L., Nitao, J. J., Hanley, W. G., Aines, R., Glaser, R. E., Sengupta, S. K., Dyer, K. M., Hickling, T. L., and Daily, W. D. (2005). Stochastic inversion of electrical resistivity changes using a Markov Chain Monte Carlo approach. *Journal of Geophysical Research: Solid Earth*, 110(2):B02101.

Rangel, R. C., Parsekian, A. D., Farquharson, L. M., Jones, B. M., Ohara, N., Creighton, A. L., Gaglioti, B. V., Kanevskiy, M., Breen, A. L., Bergstedt, H., Romanovsky, V. E., and Hinkel, K. M. (2021). Geophysical Observations of Taliks Below Drained Lake Basins on the Arctic Coastal Plain of Alaska. *Journal of Geophysical Research: Solid Earth*, 126:e2020JB020889.

Rekant, P., Bauch, H. A., Schwenk, T., Portnov, A., Gusev, E., Spiess, V., Cherkashov, G., and Kassens, H. (2015). Evolution of subsea permafrost landscapes in Arctic Siberia since the Late Pleistocene: a synoptic insight from acoustic data of the Laptev Sea. *Arktos*, 1:11.

Revil, A. and Glover, P. W. J. (1998). Nature of surface electrical conductivity in natural sands, sandstones, and clays. *Geophysical Research Letters*, 25(5):691–694.

Rey, E. and Jongmans, D. (2007). A 2D numerical study of the effect of particle shape and orientation on resistivity in shallow formations. *Geophysics*, 72(1):F9–F17.

Reynolds, J. M. (2011). *An introduction to applied and environmental geophysics*. Jhon Wiley & Sons, Ltd, 2 edition.

Robinson, D., Binley, A., Crook, N., Day-Lewis, F., Ferré, T. P. A., Grauch, V. J. S., Knight, R., Knoll, M., Lakshmi, V., Miller, R., Nyquist, J., Pellerin, L., Singha, K., and Slater, L. D. (2008). Advancing process-based watershed hydrological research using near-surface geophysics: a vision for, and review of, electrical and magnetic geophysical methods. *Hydrological processes*, 22:3604–3635.

Ronczka, M., Hellman, K., Günther, T., Wisén, R., and Dahlin, T. (2017). Electric resistivity and seismic refraction tomography: A challenging joint underwater survey at Äspö Hard Rock Laboratory. *Solid Earth*, 8(3):671–682.

Ronczka, M., Voß, T., and Günther, T. (2015). Cost-efficient imaging and monitoring of saltwater in a shallow aquifer by using long electrode ERT. *Journal of Applied Geophysics*, 122:202–209.

Rosas-Carbajal, M., Linde, N., Kalscheuer, T., and Vrugt, J. A. (2014). Two-dimensional probabilistic inversion of plane-wave electromagnetic data: Methodology, model constraints and joint inversion with electrical resistivity data. *Geophysical Journal International*, 196(3):1508–1524.

Rothman, D. H. (1985). Nonlinear inversion, statistical mechanics, and residual statics estimation. *Geophysics*, 50(12):2784–2796.

Roy, A., Dubey, C. P., and Prasad, M. (2021). Gravity inversion of basement relief using Particle Swarm Optimization by automated parameter selection of Fourier coefficients. *Computers and Geosciences*, 156:104875.

Roy, L., Sen, M. K., McIntosh, K., Stoffa, P. L., and Nakamura, Y. (2005). Joint inversion of first arrival seismic travel-time and gravity data. *Journal of Geophysics and Engineering*, 2(3):277–289.

Rücker, C., Günther, T., and Spitzer, K. (2006). Three-dimensional modelling and inversion of dc resistivity data incorporating topography - I. Modelling. *Geophysical Journal International*, 166(2):495–505.

Rücker, C., Günther, T., and Wagner, F. M. (2017). pyGIMLi: An open-source library for modelling and inversion in geophysics. *Computers and Geosciences*, 109:106–123.

Rumpf, M. and Tronicke, J. (2014). Predicting 2D geotechnical parameter fields in near-surface sedimentary environments. *Journal of Applied Geophysics*, 101(2014):95–107.

Rumpf, M. and Tronicke, J. (2015). Assessing uncertainty in refraction seismic traveltime inversion using a global inversion strategy. *Geophysical Prospecting*, 63(5):1188–1197.

Ruppel, C. D. and Kessler, J. D. (2017). The interaction of climate change and methane hydrates. *Reviews of Geophysics*, 55(1):126–168.

Saltelli, A., Ratto, M., Andres, T., Campolongo, F., Cariboni, J., Gatelli, D., Saisana, M., and Tarantola, S. (2008). *Global sensitivity analysis: The primer*. John Wiley and Sons.

Sambridge, M. (1999). Geophysical inversion with a neighbourhood algorithm–II. Appraising the ensemble. *Geophysical Journal International*, 138(3):727–746.

Santangelo, N., Daunis-i Estadella, J., di Crescenzo, G., di Donato, V., Faillace, P. I., Martín-Fernández, J. A., Romano, P., Santo, A., and Scorpio, V. (2012). Topographic predictors of susceptibility to alluvial fan flooding, Southern Apennines. *Earth Surface Processes and Landforms*, 37(8):803–817.

Savi, S., Norton, K. P., Picotti, V., Akçar, N., Delunel, R., Brardinoni, F., Kubik, P., and Schlunegger, F. (2014). Quantifying sediment supply at the end of the last glaciation: Dynamic reconstruction of an alpine debris-flow fan. *Bulletin of the Geological Society of America*, 126(5-6):773–790.

Sayedi, S. S., Abbott, B. W., Thornton, B. F., Frederick, J. M., Vonk, J. E., Overduin, P. P., Schädel, C., Schuur, E. A. G., Bourbonnais, A., Demidov, N., Gavrilov, A., He, S., Hugelius, G., Jakobsson, M., Jones, M. C., Joung, D. J., Kraev, G., Macdonald, R. W., David McGuire, A., Mu, C., O'Regan, M., Schreiner, K. M., Stranne, C., Pizhankova, E., Vasiliev, A., Westermann, S., Zarnetske, J. P., Zhang, T., Ghandehari, M., Baeumler, S., Brown, B. C., Frei, R. J., O'Regan, M., Schreiner, K. M., Stranne, C., Pizhankova, E., Vasiliev, A., Westermann, S., Zarnetske, J. P., Zhang, T., Ghandehari, M., Baeumler, S., Brown, B. C., and Frei, R. J. (2020). Subsea permafrost carbon stocks and climate change sensitivity estimated by expert assessment. *Environmental Research Letters*, 15:124075.

Scheidt, C., Li, L., and Caers, J. (2018). *Quantifying uncertainty in subsurface systems*. John Wiley and Sons.

Schirrmeister, L., Grigoriev, M. N., Strauss, J., Grosse, G., Overduin, P. P., Kholodov, A., Guenther, F., and Hubberten, H.-W. (2018). Sediment characteristics of a thermokarst lagoon in the northeastern Siberian Arctic (Ivashkina Lagoon, Bykovsky Peninsula). *Arktos*, 4:13.

Schirrmeister, L., Siegert, C., Kunitzky, V. V., Grootes, P. M., and Erlenkeuser, H. (2002). Late quaternary ice-rich permafrost sequences as a paleoenvironmental archive for the Laptve Sea Region in Northern Siberia. *International Journal of Earth Sciences*, 91(1):154–167.

Schnaidt, S. and Heinson, G. (2015). Bootstrap resampling as a tool for uncertainty analysis in 2-D magnetotelluric inversion modelling. *Geophysical Journal International*, 203(1):92–106.

Schoch-Baumann, A., Blöthe, J. H., Munack, H., Hornung, J., Codilean, A. T., Fülöp, R. H., Wilcken, K., and Schrott, L. (2022). Postglacial outsize fan formation in the Upper Rhone valley, Switzerland – gradual or catastrophic? *Earth Surface Processes and Landforms*, 47:1032–1053.

Schönleber, V. L., Lucía, A., Seitz, S., and Eberle, J. (2022). Sedimentologische Untersuchungen extremer Abflussereignisse am Beispiel des Grimmbachs in Südwestdeutschland. *Jber. Mitt. Oberrhein. geol. Ver.*, 104:291–312.

Schrott, L. and Sass, O. (2008). Application of field geophysics in geomorphology: Advances and limitations exemplified by case studies. *Geomorphology*, 93(1-2):55–73.

Schürch, P., Densmore, A. L., Ivy-Ochs, S., Rosser, N. J., Kober, F., Schlunegger, F., McArdell, B., and Alfimov, V. (2016). Quantitative reconstruction of late Holocene surface evolution on an alpine debris-flow fan. *Geomorphology*, 275:46–57.

Schuur, E. A. G., McGuire, A. D., Schädel, C., Grosse, G., Harden, J. W., Hayes, D. J., Hugelius, G., Koven, C. D., Kuhry, P., Lawrence, D. M., Natali, S. M., Olefeldt, D., Romanovsky, V. E., Schaefer, K., Turetsky, M. R., Treat, C. C., and Vonk, J. E. (2015). Climate change and the permafrost carbon feedback. *Nature*, 520(7546):171–179.

Scott, W. J., Sellmann, P. V., and Hunter, J. A. (1990). Geophysics in the study of permafrost. In Ward, S. H., editor, *Geotechnical and environmental geophysics*, volume I, pages 355–384. Society of Exploration Geophysicists.

Sellmann, P. V. (1989). Seafloor temperature and conductivity data from coastal waters of the US Beaufort Sea. Technical Report 1, US Army Corps of Engineers, Cold Regions Research and Engineering Laboratory.

Sellmann, P. V., Delaney, A. J., and Arcone, S. A. (1989). Coastal subsea permafrost and bedrock observations using dc resistivity. Technical report, US Army Corps of Engineers, Cold Regions Research and Engineering Laboratory.

Sen, M. K. and Stoffa, P. L. (1991). Nonlinear one-dimensional seismic waveform inversion using simulated annealing. *Geophysics*, 56(10):1624–1638.

Sen, M. K. and Stoffa, P. L. (1996). Bayesian inference, Gibbs' sampler and uncertainty estimation in geophysical inversion. *Geophysical Prospecting*, 44(2):313–350.

Sen, M. K. and Stoffa, P. L. (2013). *Global optimization methods in geophysical inversion*. Cambridge University Press.

Shakhova, N., Semiletov, I., Gustafsson, O., Sergienko, V., Lobkovsky, L., Dudarev, O., Tumskoy, V., Grigoriev, M., Mazurov, A. K., Salyuk, A., Ananiev, R., Koshurnikov, A., Kosmach, D., Charkin, A., Dmitrevsky, N., Karnaukh, V., Gunar, A., Meluzov, A., and Chernykh, D. (2017). Current rates and mechanisms of subsea permafrost degradation in the East Siberian Arctic Shelf. *Nature Communications*, 8(1):15872.

Shaw, R. and Srivastava, S. (2007). Particle swarm optimization: A new tool to invert geophysical data. *Geophysics*, 72(2):F75–F83.

Sherman, D., Kannberg, P., and Constable, S. (2017). Surface towed electromagnetic system for mapping of subsea Arctic permafrost. *Earth and Planetary Science Letters*, 460:97–104.

Shevnin, V., Mousatov, A., Ryjov, A., and Delgado-rodriquez, O. (2007). Estimation of clay content in soil based on resistivity modelling and laboratory measurements. *Geophysical Prospecting*, 55(2):265–275.

Shewchuk, J. R. (1996). Triangle: engineering a 2D quality mesh generator and delaunay triangulator. In Lin, M. C. and Manocha, D., editors, *Applied Computational Geometry Towards Geometric Engineering*, pages 203–222. Springer.

Si, H. (2015). TetGen, a delaunay-based quality tetrahedral mesh generator. *ACM Transactions on Mathematical Software*, 41(2):11.

Smith, T., Hoversten, M., Gasperikova, E., and Morrison, F. (1999). Sharp boundary inversion of 2D magnetotelluric data. *Geophysical Prospecting*, 47(4):469–486.

Sobol, I. M. (2001). Global sensitivity indices for nonlinear mathematical models and their Monte Carlo estimates. *Mathematics and computers in simulation*, 55:271–280.

Spitzer, K. (1998). The three-dimensional DC sensitivity for surface and subsurface sources. *Geophysical Journal International*, 134(3):736–746.

Stevens, C. W., Moorman, B. J., and Solomon, S. M. (2008). Detection of frozen and unfrozen interfaces with ground penetrating radar in the nearshore zone of the Mackenzie Delta , Canada. In *Proceedings of the 9th International Conference on Permafrost, Fairbanks, AK, USA*, pages 1711–1716.

Stoffa, P. L. and Sen, M. K. (1991). Nonlinear multiparameter optimization using genetic algorithms: inversion of plane-wave seismograms. *Geophysics*, 56(11):1794–1810.

Stummer, P., Maurer, H., and Green, A. G. (2004). Experimental design: Electrical resistivity data sets that provide optimum subsurface information. *Geophysics*, 69(1):120–139.

Tarantola, A. (2005). *Inverse problem theory and methods for model parameter estimation*. SIAM.

Thibaut, R., Kremer, T., Royen, A., Kim Ngun, B., Nguyen, F., and Hermans, T. (2021). A new workflow to incorporate prior information in minimum gradient support (MGS) inversion of electrical resistivity and induced polarization data. *Journal of Applied Geophysics*, 187.

Tompkins, M. J., Fernández-Martínez, J. L., Alumbaugh, D. L., and Mukerji, T. (2011). Scalable uncertainty estimation for nonlinear inverse problems using parameter reduction, constraint mapping, and geometric sampling: Marine controlled-source electromagnetic examples. *Geophysics*, 76(4):F263–F281.

Tronicke, J. and Holliger, K. (2005). Quantitative integration of hydrogeophysical data: Conditional geostatistical simulation for characterizing heterogeneous alluvial aquifers. *Geophysics*, 70(3):H1–H10.

Tronicke, J., Paasche, H., and Böniger, U. (2012). Crosshole traveltime tomography using particle swarm optimization: A near-surface field example. *Geophysics*, 77(1):R19–R32.

Vasco, D. W., Johnson, L. R., and Majer, E. L. (1993). Ensemble inference in geophysical inverse problems. *Geophysical Journal International*, 115(3):711–728.

Vasco, D. W., Peterson, J. E., and Majer, E. L. (1996). Nonuniqueness in traveltime tomography: Ensemble inference and cluster analysis. *Geophysics*, 61(4):1209–1226.

Vinciguerra, A., Aleardi, M., Hojat, A., Loke, M. H., and Stucchi, E. (2022). Discrete cosine transform for parameter space reduction in Bayesian electrical resistivity tomography. *Geophysical Prospecting*, 70(1):193–209.

von Hebel, C., Rudolph, S., Mester, A., Huisman, J., and Kumbhar, P. (2014). Three-dimensional imaging of subsurface structural patterns using quantitative large-scale multi-configuration electromagnetic induction data. *Water Resources Research*, 50(3):2732–2748.

Wagner, F. M., Mollaret, C., Günther, T., Kemna, A., and Hauck, C. (2019). Quantitative imaging of water, ice and air in permafrost systems through petrophysical joint inversion of seismic refraction and electrical resistivity data. *Geophysical Journal International*, 219(3):1866–1875.

Wagner, F. M. and Uhlemann, S. (2021). An overview of multimethod imaging approaches in environmental geophysics. In *Advances in Geophysics*, volume 62, pages 1–72. Academic Press Inc.

Wainwright, H. M., Finsterle, S., Jung, Y., Zhou, Q., and Birkholzer, J. T. (2014). Making sense of global sensitivity analyses. *Computers and Geosciences*, 65:84–94.

Ward, W. O. C., Wilkinson, P. B., Chambers, J. E., Oxby, L. S., and Bai, L. (2014). Distribution-based fuzzy clustering of electrical resistivity tomography images for interface detection. *Geophysical Journal International*, 197(1):310–321.

Wu, Y., Nakagawa, S., Kneafsey, T. J., Dafflon, B., and Hubbard, S. (2017). Electrical and seismic response of saline permafrost soil during freeze - Thaw transition. *Journal of Applied Geophysics*, 146:16–26.

Zhou, B. and Dahlin, T. (2003). Properties and effects of measurement errors on 2D resistivity imaging surveying. *Near Surface Geophysics*, 1(3):105–117.

Zhu, D. and Gibson, R. (2018). Seismic inversion and uncertainty quantification using trans-dimensional Markov chain Monte Carlo method. *Geophysics*, 83(4):R321–R334.